A Super-Nyquist Architecture for Rateless Underwater Acoustic Communication

by

Qing He

B.A.Sc, Electrical Engineering
University of Waterloo, 2009

Submitted to the Department of Electrical Engineering and Computer Science
in partial fulfillment of the requirements for the degree of

Master of Science

at the

MASSACHUSETTS INSTITUTE OF TECHNOLOGY

June 2012

Author .....
Department of Electrical Engineering and Computer Science
May 11, 2012

Certified by .....
Professor Gregory W. Wornell
Professor of Electrical Engineering and Computer Science
Thesis Supervisor

Certified by .....
Dr. Uri Erez
Senior Lecturer of Electrical Engineering At Tel Aviv University
Thesis Supervisor

Accepted by .....
Leslie Kolodziejski
Chairman, Department Committee on Graduate Students

A Super-Nyquist Architecture for Rateless Underwater Acoustic Communication

by

Qing He

Submitted to the Department of Electrical Engineering and Computer Science
on May 11, 2012, in partial fulfillment of the
requirements for the degree of
Master of Science

Abstract

Oceans cover about 70 percent of Earth's surface. Despite the abundant resources they contain, much of them remain unexplored. Underwater communication plays a key role in the area of deep ocean exploration. It is also essential in the field of the oil and fishing industry, as well as for military use. Although research on communicating wirelessly in the underwater environment began decades ago, it remains a challenging problem due to the oceanic medium, in which dynamic movements of water and rich scattering are commonplace.

In this thesis, we develop an architecture for reliably communicating over the underwater acoustic channel. A notable feature of this architecture is its rateless property: the receiver simply collects pieces of transmission until successful decoding is possible. With this, we aim to achieve capacity-approaching communication under a variety of a priori unknown channel conditions. This is done by using a super-Nyquist (SNQ) transmission scheme. Several other important technologies are also part of the design, among them dithered repetition coding, adaptive decision feedback equalization (DFE), and multiple-input multiple-output (MIMO) communication.

We present a complete block diagram for the transmitter and receiver architecture for the SNQ scheme. We prove the sufficiency of the architecture for optimality, and we show through analysis and simulation that as the SNQ signaling rate increases, the SNQ scheme is indeed capacity-achieving. At the end, the performance of the proposed SNQ scheme and its transceiver design are tested in physical experiments, whose results show that the SNQ scheme achieves a significant gain in reliable communication rate over conventional (non-SNQ) schemes.

Thesis Supervisor: Professor Gregory W. Wornell
Title: Professor of Electrical Engineering and Computer Science

Thesis Supervisor: Dr. Uri Erez
Title: Senior Lecturer of Electrical Engineering At Tel Aviv University

Acknowledgments

First and foremost, I would like to offer my sincerest gratitude to my thesis advisors Professor Gregory Wornell and Professor Uri Erez. When I first started my Master's program, I did not know much about communication systems. Professor Wornell guided me through the learning process by letting me tackle small problems that – for many of them – he already knew the answers to. He has taught me to not just focus on getting results, but that it is more important to think about the meaning and the implication of the results. He has often asked me, "How are you going to plot these results that will be meaningful to the system engineers?" I would also like to thank Professor Erez for his humor, kindness, and patience. I have learnt a lot through working with Uri, things from specific technical tools, debugging methods, to presentation skills. No matter where he is, he is always interested in discussing problems and replies right away. There are many other things I have learnt from them and I feel deeply grateful for being able to work with them. Without their support and guidance, this thesis would not have been possible.

I would also like to thank Professor James Preisig for being my supervisor during my summer internship at the Woods Hole Oceanographic Institute. I have learnt a lot of insights from him through the internship as well as through the conference calls and emails that followed. In addition, I want to thank Dr. Vijay Divi for helping me get started on the project, and David Ensberg at the Scripps Institution of Oceanography for uploading data for me upon my last-minute request.

It was a great pleasure being part of the Signals, Information, and Algorithms Lab with my friendly and cheerful labmates: Gauri, Maryam, Atulya, Da, Ying-zong, James, Venkat, Charles, Vijay, Anthony, Yuval, Ligong, and Arya. They have provided me with invaluable assistance and encouragement, not to mention the good laughs. Specifically, I would like to thank Da for generously giving me his thesis template, as well as tips on how to use LaTeX. I want to thank Gauri for helping me fix bugs when I first started using LaTeX and Atulya for answering my questions on channel equalizers. Ying-zong is very quiet. I remember talking to him only when I needed help. I wish to thank him for helping me with the server at 2AM in the morning and for his tremendous help through the process of editing the thesis. Many thanks to Tricia who is always so caring and helpful; and to Vanni for giving me extra space on the server and helping me install the newer version of MATLAB. In addition, I would like to thank my dear friend Lei, who suggested and

helped me to convert my thesis from PDF to Word file such that I can use the spelling and grammar checker.

Last but not least, I would like to thank my parents for their support, encouragement, and love. Without them, I would never have the opportunity to come here and have the wonderful experience at MIT.

Contents

List of Figures

Chapter 1

Introduction

1.1 Background of Underwater Communication

The goal of this thesis is to develop a wireless communication architecture for the underwater channel. Currently, communications under the ocean are mostly conducted using robotic vehicles that are attached to surface ships with expensive and heavy cables that significantly limit the range of the robot. Furthermore, electromagnetic communication as done terrestrially is difficult under the ocean due to heavy attenuation by conductive seawater, such that signal waves only penetrate a few meters. Therefore, most attention for underwater communication has focused on the acoustic channel, with acoustic transducers and hydrophones serving the roles of transmitters and receivers, respectively. Techniques developed for the underwater channel may potentially be applied to general wireless communication.

The underwater acoustic (UWA) channel is one of the most challenging channels for wireless communication. The dynamic ocean environment presents a large amount of inter-symbol interference (ISI) and a rapidly time-varying channel. The channel bandwidth is limited to the order of Kilo-Hertz due to frequency-dependent attenuation. The channel delay spread is around 50 ms due to the rich scattering environment. The Doppler spread is significant due to slow wave speed and ocean mass propagation. As a result, our goal is to design a scheme which overcomes these issues and achieves reliable and fast communication over the UWA channel. Specifically, in order to compensate for the time-variation of the UWA channel, we desire to design a rateless communication scheme that aims to operate at rates close to the channel capacity under all channel conditions. For a detailed description of the UWA communication problem and recent advances in UWA signal processing techniques, one can refer to [1], [2] and [3].

1.2 Rateless Codes and SNQ Signaling

With the invention of efficient error-correction codes such as Low-Density Parity-Check (LDPC) codes and Turbo codes, we can achieve rates very close to the capacity for additive white Gaussian noise (AWGN) channels. Nevertheless, reliable communication remains difficult over many other noisy channels such as the time-varying underwater channel. To achieve capacity-approaching communication with fixed rate coding, both the transmitter and the receiver have to know the channel statistics in advance and use an error correction scheme specifically designed for this channel. Knowing the channel statistics exactly is infeasible for the constantly changing UWA channel. As a result, channel capacity cannot be achieved with a fixed code rate, because a code designed for a channel with high signal to noise ratio (SNR) will result in decoding failure for a channel with low SNR. In contrast, a capacity-achieving code for a low SNR channel will be inefficient for a high SNR channel.

In order to resolve this problem and allow capacity-achieving communication in the varying channel condition, the concept of rateless coding emerged. Rateless code is a code with (potentially) infinite length and has the property that high-rate codewords are prefix of lower rate codewords. In other words, instead of using a pre-determined code rate, the transmitter encodes the information bits into an infinitely long stream of symbols and starts transmitting them to the receiver. The receiver will keep on collecting packets until successful decoding is achieved. At the end of each session, an Automatic Repeat reQuest (ARQ) component in the receiver sends an acknowledgment message to the transmitter and the transmitter will transmit the next set of packets.

Capacity-achieving rateless codes such as LT codes and Raptor codes have been developed for Binary Erasure Channels (BEC). A comprehensive review of these rateless codes can be found in [4]. A rateless coding scheme for the AWGN channel is introduced in [5]. This thesis develops a rateless coding scheme for the time-varying Gaussian ISI channel, as well as a simple decoding architecture for this scheme. The overall system performance is shown to be capacity-approaching.

The simplest rateless scheme would be to use a repetition code that transmits the same codeword repeatedly over the channel. Let us define the effective spectral efficiency as information rate transmitted through a single redundancy block and the total spectral efficiency over M re-

dundancy blocks as the information rate transmitted through M redundancy blocks. In this case, with a fixed channel SNR, the gain in total spectral efficiency increases logarithmically with M such that

$$\text{total spectral efficiency} = \log_2(1 + M \times \text{SNR}) \qquad [\text{bits}/M \text{ channel uses}]; \tag{1.1}$$

whereas the total channel capacity over M channel uses increases linearly with the number of redundancy blocks such that

$$C_{\text{tot}} = M\log_2(1 + \text{SNR}) \qquad [\text{bits}/M \text{ channel uses}]. \tag{1.2}$$

From another point of view, the effective spectral efficiency of each redundancy block is decreasing with M and it is given by

$$\text{effective spectral efficiency} = \frac{1}{M}\log_2(1 + M \times \text{SNR}) \qquad [\text{bits/channel use}]; \tag{1.3}$$

whereas the channel capacity stays constant at

$$C = \log_2(1 + \text{SNR}) \qquad [\text{bits/channel use}]. \tag{1.4}$$

Although the effective spectral efficiency for the pure repetition coding scheme, given by Eq. (1.3), is close to the channel capacity when SNR is much smaller than 1 (0dB), the overall communication system still cannot operate at capacity approaching rates because existing capacity achieving channel codes are inefficient in this regime. In addition, for a time-varying ISI channel, the conventional decoding scheme fails when the SNR is low. Consequently, the pure repetition coding scheme is inefficient for practical applications. In [5], [6] and [7], a rateless coding scheme for Gaussian channels is introduced. The proposed scheme incorporated techniques such as super-Nyquist (SNQ) signaling, dithered repetition coding and adaptive channel equalization. In this thesis, we develop several aspects and some properties of the SNQ rateless coding scheme, and evaluate its performance in simulations and experiments.

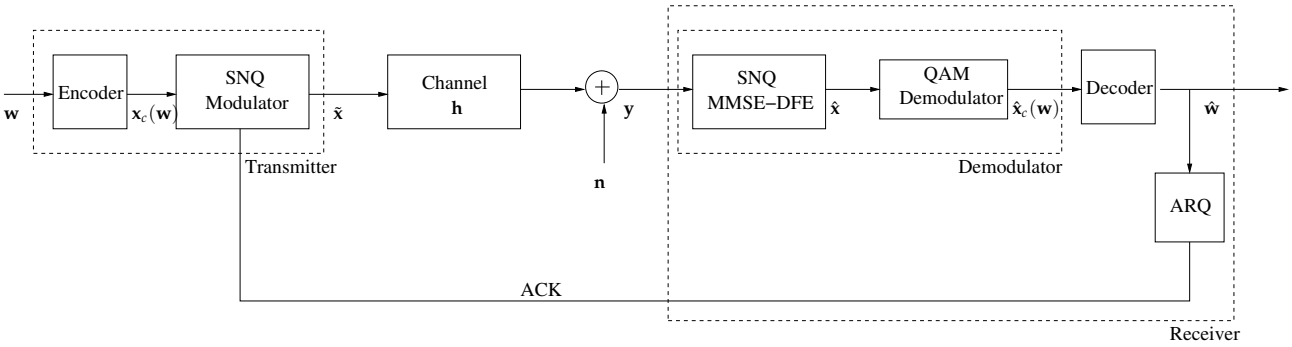

Figure 1-1: Discrete-time model with transmitter, channel and receiver

1.3 Discrete-Time Model of the Communication System

The UWA channel is a band-limited, time-varying, multi-path channel. The discrete time model of the UWA communication channel over a static interval is shown in Figure 1-1, where $\mathbf{h}$ represents the channel impulse response. In addition, the vector $\tilde{\mathbf{x}}$ denotes the complex baseband transmit data vector; the vector $\mathbf{n}$ denotes the complex AWGN vector; and $\mathbf{y}$ is the vector representing the baseband received signal.

As shown in Figure 1-1, the transmitter is composed of the channel encoder and the SNQ modulator. The encoder maps the incoming message $\mathbf{w}$ into a codeword $\mathbf{x}_c(\mathbf{w})$ and sends it to the modulator. The SNQ modulator consists of a QAM modulator, a redundancy block generator and a pulse shape modulator. The QAM modulator maps the binary information vector $\mathbf{x}_c(\mathbf{w})$ into a vector of symbols, denoted by $\mathbf{x}$, with a QAM constellation (e.g. QPSK, 16-QAM). Then the redundancy generator generates an arbitrary number of redundancy blocks (also called a redundancy packet) with the dithered coding scheme to be presented in Chapter 2. Lastly, the symbol block is modulated with a baseband pulse shape corresponding to a pre-determined SNQ signaling rate. If this SNQ signaling rate is set to 1, then it is equivalent to Nyquist signaling. We show in Chapter 3 that, under the assumption of optimal decoding, the combined scheme of dithered repetition coding and SNQ signaling is capacity achieving for the time-varying ISI channel.

At the receiver end, we adopt the structure of the minimum-mean-squared-error (MMSE) decision-feedback-equalizer (DFE) to overcome ISI introduced by both the channel and SNQ signal modulation. This serial concatenation of the MMSE-DFE and the channel decoder structure is optimal under the assumption of perfect feedback in the MMSE-DFE [8]. In practice, an iterative scheme

between the MMSE-DFE and the channel decoder is required to achieve optimality. The receiver diagram in Figure 1-1 illustrates a single channel DFE that decodes the received signal from a single hydrophone for a single redundancy block. In Chapter 2, we generalize this simple structure to a joint decoder that combines the received signals from multiple hydrophones, as well as multiple redundancy blocks. Moreover, we propose a simple decoder structure for the SNQ scheme when the redundancy blocks are dithered with DFT sequences and show that its coefficients converge to the optimal MMSE-DFE filter. At the end of Chapter 2, we demonstrate a modified MMSE-DFE design for the multiple-input-multiple-output (MIMO) SNQ scheme.

After demodulating symbols to binary bits with a QAM constellation, the channel decoder decodes the received bits and checks the validity of the decoded signal. If decoding is unsuccessful, the decoder waits for another redundancy packet and repeats the decoding process. If the current packet is successfully decoded, the decoder flags the ARQ unit, which then sends an acknowledgment message to the transmitter. Upon receiving the acknowledgement message, the transmitter starts transmitting the next packet.

The system in Figure 1-1 comprises the major the components of a standard transceiver structure for the Gaussian ISI channel. Next, we will briefly describe the key concepts of the SNQ modulation and demodulation schemes. First, the transmitter is assigned a signaling rate, which is faster than the conventional Nyquist signaling rate. By using SNQ signaling, we can transmit symbols at a higher rate than the Nyquist rate while using the same signal power and bandwidth as Nyquist signals. This gain in signaling rate is at the expense of ISI. The tradeoffs balance out exactly such that, with capacity achieving coding and perfect feedback MMSE-DFE equalization, the SNQ signaling scheme achieves the channel capacity in the time-invariant AWGN channel setup just as the Nyquist scheme. So, what is the benefit of SNQ signaling? The SNQ signaling scheme unveils its advantage when coupled with dithered repetition coding. With dithering, the modulator performs an unitary transformation on the original codeword and encodes this codeword into mutually independent redundancy blocks which are transmitted subsequently at the SNQ rate over the channel. At the receiver, a subset of these redundancy blocks are cumulated and jointly decoded to recover the original codeword and the number of packets required for successful decoding depends on the channel condition(e.g. ISI, SNR and coherence time of the channel).

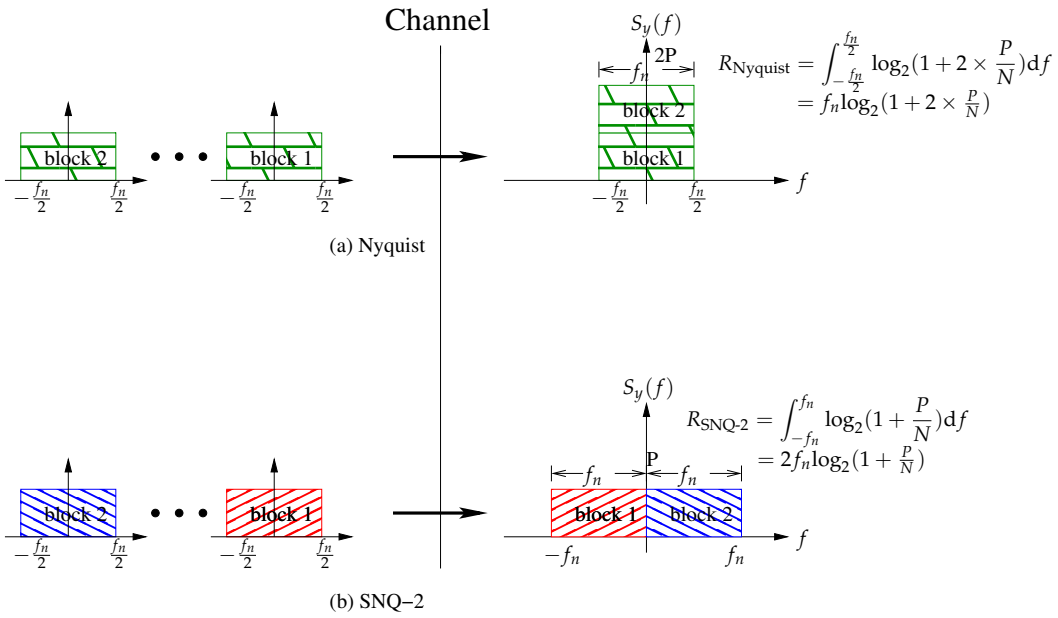

Figure 1-2: PSD figure of Nyquist and SNQ-2 signals with 2 redundancy blocks

The following figure provides a simple illustration of the benefit of the dithered SNQ repetition scheme (i.e. SNQ signaling with each redundancy block element-wise multiplied with a different dithering vector) when compared with Nyquist repetition coding. As shown in Figure 1-2, two packets are transmitted over the channel for each of the Nyquist and the SNQ-2 (i.e. signaling at two times the Nyquist rate) schemes. With pure repetition (i.e. all packets are identical), the two Nyquist packets are combined to obtain a gain in signal power such that the total spectral efficiency increases logarithmically with the number of redundancy blocks (i.e $R_{\text{Nyquist}} = \log_2(1+2\times\text{SNR})$). In contrast, the two packets generated from the SNQ-2 scheme are designed to represent information in different frequency bands, which, when jointly decoded, yields a linear gain in total spectral frequency (i.e. $R_{\text{SNQ-2}} = 2\log_2(1+\text{SNR})$). Furthermore, another attractive feature of the SNQ scheme is that an arbitrary subset of the packets can be combined for decoding in spite of their order. Hence, when coupled with dithering, the SNQ scheme offers a framework for constructing a capacity-approaching rateless code for the time-varying UWA channel.

1.4 Notation

Throughout this thesis, boldface uppercase letters denote matrices. Boldface lowercase letters denote vectors. All vectors are assumed to be column vectors. Lower case letters denote scalar quantities. The superscripts T, * ,and H denote transpose, complex conjugate, and Hermitian transpose, respectively. The symbol **I** denotes an identity matrix. In the following chapters, the size of an identity matrix **I** is always equal to the size of the square matrix that it is added to. The symbols $\circ$ and $*$ denote element-wise matrix multiplication and linear convolution, respectively. The $\hat{}$ denotes the estimate of the quantity under the caret.

In addition, when we refer to an N-tap linear filter $\mathbf{h} = [h_0, h_1, \ldots, h_{N-1}]$ by a matrix **H**, it means that the filtering operation $\mathbf{y} = \mathbf{h} * \mathbf{x}$ is expressed in the equivalent matrix from $\mathbf{y} = \mathbf{H}\mathbf{x}$, where **H** is a Toeplitz matrix of appropriate size with **h** (zero-padded as necessary) on each row. Specifically, it is given by,

$$\mathbf{H} = \begin{bmatrix} h_0 & h_1 & h_2 & \ldots & 0 & \ldots & 0 \\ 0 & h_0 & h_1 & \ldots & 0 & \ldots & 0 \\ \vdots & \vdots & \vdots & \vdots & \ddots & \vdots & \vdots \\ 0 & \ldots & 0 & h_0 & h_2 & \ldots & h_N \end{bmatrix}. \tag{1.5}$$

Chapter 2

System Architecture

In this chapter, we begin by exploring each component of the communication system (Figure 1-1) in detail. The transmitter module encapsulates the channel encoder and the signal modulator. It takes in a sequence of information bits and potentially generates an arbitrary number of redundancy packets. These redundancy packets are then transmitted subsequently through a discrete-time Gaussian ISI channel. Next, we present a number of decoder structures that are commonly used in ISI channel communications. For each codeword, the receiver continuously cumulates redundancy blocks and feed them into the decoder which consists of an channel equalizer that jointly decodes multiple redundancy blocks and a channel code decoder. If the symbol error rate at the decoder output is sufficiently low that the original codeword can be successfully decoded, the receiver sends an ARQ request to the transmitter to initiate the transmission of the next codeword. On the other hand, if the decoder is not able to decode the current codeword, it waits for the next packet, sends it to the joint decoder along with all the previous packets and attempts to decode again. This step repeats until decoding for the current codeword has succeeded.

The block diagram of the communication shown in Figure 1-1 is reproduced below with added details of the MMSE-DFE. In the second part of this chapter, we describe the SNQ scheme which

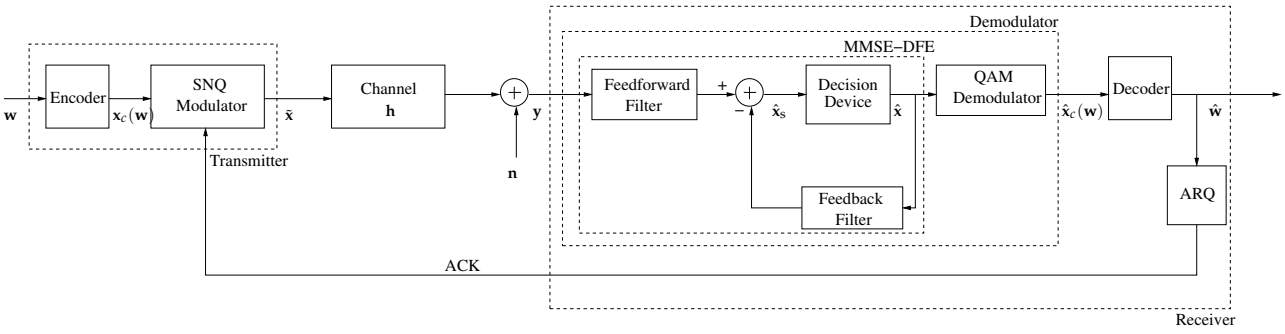

Figure 2-1: Discrete-time model of a single-input-single-output system with transmitter, channel and receiver

as introduced in [7] and present a decoder structure for the SNQ scheme. Lastly, we demonstrate the architecture used in the Kauai Acomms MURI 2011 (KAM11) experiments.

2.1 Channel Encoder and Decoder

The channel encoder takes l_{i} bits of the binary information message $\mathbf{w}$ as input and encodes it into l_{o} bits of codeword $\mathbf{x}_c(\mathbf{w}) \in \{0,1\}^{l_{\mathrm{o}}}$, at the base code rate of $R_{\mathrm{b}} = l_{\mathrm{i}}/l_{\mathrm{o}}$. This base code rate is carefully chosen with respect to the effective coding channel, which is the intermediate system that the code sees. We show later in Chapter 3 that this channel behaves as an additive white Gaussian noise (AWGN) channel under the SNQ scheme. If the parameters of the SNQ scheme, such as the base code rate and the SNQ signaling rate, are chosen in the way such that the targeting communication rate matches the channel capacity, by applying existing capacity-achieving codes, the SNQ scheme achieves a communication rate close to the channel capacity.

2.2 Modulator

The SNQ modulator is the interface between the binary codeword $\mathbf{x}_c(\mathbf{w})$ and the transmitter output. Traditionally, the modulator for Nyquist signals consists of a constellation modulator (e.g. QAM) and a band-limited pulse shape modulator. In order to achieve effective rateless coding, the SNQ scheme makes two modifications on the standard structure: (1) an additional redundancy block generator that generates an arbitrary number of independent blocks by a process of pseudorandom dithering; and (2) generalized baseband pulse shape modulator that features SNQ signaling.

Let B denote the Nyquist bandwidth of the baseband channel. Hence, the Nyquist period and Nyquist signaling rate for this channel are $T_{\mathrm{N}} = \frac{1}{2B}$ and $f_n = 2B$, respectively. Let us denote the actual signaling frequency by f_s and let f_s be an integer multiple of f_n such that $f_s = \beta f_n$. We call β the SNQ signaling rate and denote it as the SNQ-β signaling scheme. Let M denote the number of redundancy blocks. Figure 2-2 shows the procedure for generating the i^{th} redundancy block, $\tilde{\mathbf{x}}^{(i)}$. We use the superscript (i) to indicate correspondence with the i^{th} redundancy block for $i \in \{1, 2, \ldots, M\}$ and the index k to denote the k^{th} symbol of a codeword (e.g. $\mathbf{x}[k]$) or a redundancy block (e.g. $\tilde{\mathbf{x}}^{(\mathbf{i})}[k]$). Potentially, this modulation process can be applied to $\mathbf{x}$ repeatedly to generate an arbitrarily large number of redundancy blocks.

We next describe the transmitter components in detail. First, the QAM modulator maps the bi-

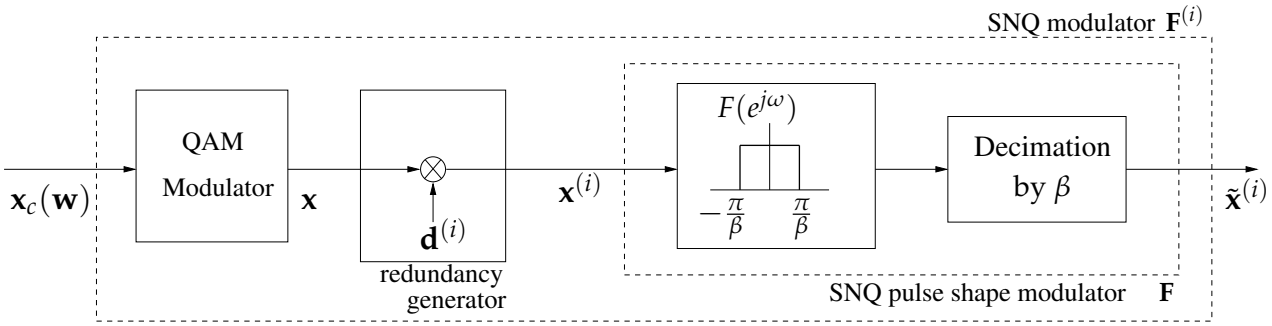

Figure 2-2: Signal modulator with dithering and SNQ pulse-shaping

nary codeword $\mathbf{x}_c(\mathbf{w})$ to a vector of symbols $\mathbf{x}$. The symbol codeword $\mathbf{x}$ is then element-wise multiplied with the i^{th} dithering sequence, $\mathbf{d}^{(i)}$, to produce its corresponding dithered redundancy block $\mathbf{x}^{(i)}$ (i.e. $\mathbf{x}^{(i)} \triangleq \mathbf{x} \circ \mathbf{d}^{(i)}$). There are potentially many different dithering schemes such as random dither, deterministic dither with Hadamard matrix and deterministic dither with DFT matrix. Our analysis mainly focuses on the performances of the DFT dithering scheme due to its simple decoder structure and many other favorable properties that are addressed in later chapters. After dithering, the data sequence is modulated by a band-limited baseband pulse shape (e.g. raised-cosine pulse shape). Lastly, the modulated signal is signaled at the pre-determined SNQ rate. In a practical system, the modulated discrete data signal is converted to a continuous signal using a discrete-to-continuous (D/C) convertor and modulated to its carrier frequency before transmission. We omit these components in our baseband discrete model.

2.2.1 SNQ Signaling Scheme

Two major components of the SNQ scheme are the SNQ signaling scheme and dithered repetition coding. We now explain the SNQ signaling scheme.

The communication channel we are interested in is a band-limited, ISI channel with AWGN noise. The discrete data sequence $\mathbf{x}$ is modulated with a baseband pulse shape whose bandwidth is equal to the channel bandwidth before being transmitted through the channel. To better understand the SNQ signaling method, let us look at the continuous-time signal. The continuous band-limited transmitting signal $x(t)$ is constructed from modulating each symbol of $\mathbf{x}[k]$ with the baseband pulse shape, $f(t)$, such that

$$x(t) = \sum_{k=0}^{\infty} \mathbf{x}[k] f(t - kT_{\text{N}}).$$

When we signal at β times the Nyquist rate, the continuous signal can be expressed as

$$x(t) = \sum_{k=0}^{\infty} \mathbf{x}[k] f(t - k\frac{T_{\mathrm{N}}}{\beta}),$$

that adjacent symbols are spaced with time $\frac{T_{\mathrm{N}}}{\beta}$.

Figure 2-3 illustrates an example, in which the Nyquist and the SNQ-2 signaling schemes has Nyquist period T_{N}, modulation pulse $f(t) = \mathrm{sinc}(t)$, and the symbol vector $\mathbf{x} = [111]$. The difference between the two schemes is that the Nyquist symbols are transmitted with T_{N}s apart, as shown by the top plot in Figure 2-3; whereas the SNQ-2 symbols are spaced by $\frac{T_{\mathrm{N}}}{2}$s, as shown by the bottom plot in Figure 2-3. In other words, the Nyquist scheme transmits $1/T_{\mathrm{N}}$ symbols per second, while the SNQ-β scheme transmits β/T_{N} symbols per second. It is shown in Figure 2-3 that when sampled at the Nyquist rate, each sample (indicated by an arrow) from the Nyquist signal is equal to the value of its corresponding symbol without ISI, whereas the samples from the SNQ-2 signal suffer from ISI from neighboring symbols. It is important to note that both the Nyquist and SNQ signals have the same bandwidth, which is equal to the bandwidth of the modulation pulse shape $f(t)$.

In the discrete time domain, the SNQ signaling scheme can be modeled by downsampling a SNQ rate sequence to the Nyquist rate. As shown in Figure 2-2, with Nyquist signaling the time-sequence $\mathbf{x}^{(i)}$ is spaced at intervals of spacing T_{N}, whereas with SNQ-signaling, the time-sequence $\mathbf{x}^{(i)}$ is spaced at intervals of smaller size $\frac{T_{\mathrm{N}}}{\beta}$. Due to the band-limited natural of the channel, this SNQ-signal is then down-sampled to the Nyquist rate, yielding $\tilde{\mathbf{x}}^{(i)}$.

2.2.2 Matrix Representation of the Modulation Procedure

Let L_{x} denote the length of $\mathbf{x}$ such that L_{x} is an integer multiple of β. This way, the down-sampled Nyquist rate signal $\tilde{\mathbf{x}}^{(i)}$ has an integer length $\frac{L_x}{\beta}$. The signal modulation procedure described by

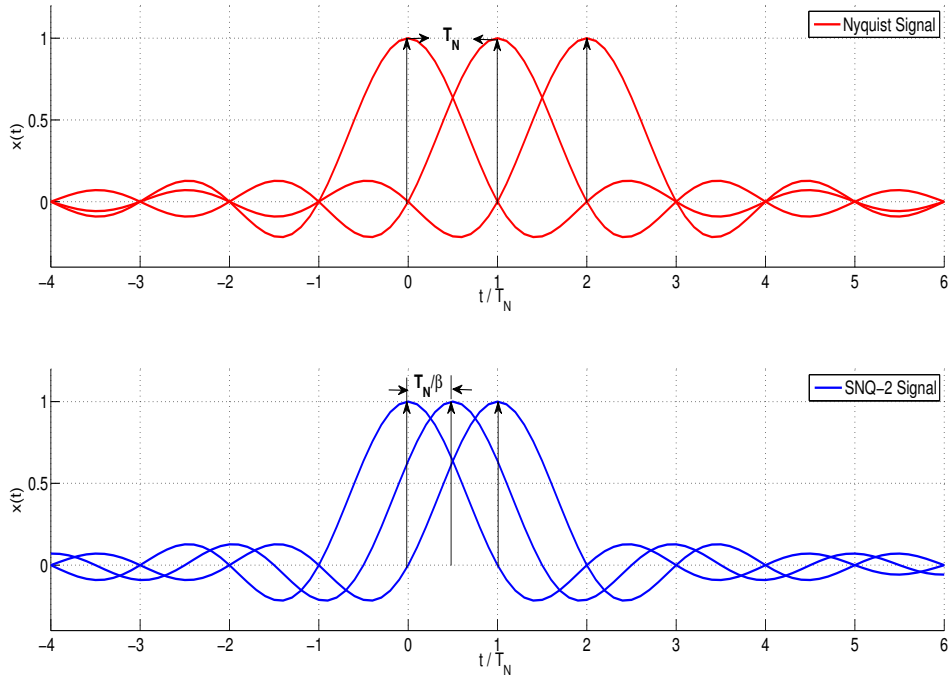

Figure 2-3: Pulse shape of Nyquist and SNQ-2 signaling

Figure 2-2 can be expressed in matrix form as,

$$\tilde{\mathbf{x}}^{(i)} = \mathbf{F}(\mathbf{x} \circ \mathbf{d}^{(i)}) \tag{2.1}$$

$$\triangleq \mathbf{F}\mathbf{x}^{(i)}$$

$$\triangleq (\mathbf{F} \circ \mathbf{D}^{(i)})\mathbf{x} \tag{2.2}$$

$$\triangleq \mathbf{F}^{(i)}\mathbf{x}, \tag{2.3}$$

where $(\mathbf{x} \circ \mathbf{d}^{(i)})$ and $\mathbf{F}$ in Eq. (2.1), respectively, correspond to the dither and the pulse shape modulator in Figure 2-2. The dither vector $\mathbf{d}^{(i)}$ is a column vector of equal length as the codeword $\mathbf{x}$ and the modulation matrix $\mathbf{F}$ is of size $\frac{L_x}{\beta} \times L_x$. Eq. (2.2) rearranges the dithering vector into a matrix, denoted by $\mathbf{D}^{(i)}$, such that the dithering step and the downsampling step can be combined into one matrix $\mathbf{F}^{(i)}$, as shown in Eq. (2.3).

We now describe how each dithering matrix $\mathbf{D}^{(i)}$ is constructed. We delay the description for the pulse modulation matrix $\mathbf{F}^{(i)}$ until Chapter 3. First, $\mathbf{D}^{(i)}$ is a matrix of the same size as $\mathbf{F}$ and is

composed of repetitions of the row vector $\mathbf{d}^{(i)^{\mathrm{T}}}$, where $\mathbf{d}^{(i)^{\mathrm{T}}}$ is constructed from a base dithering matrix. Let $\mathbf{D}$ denote this base dithering matrix of size $M \times M$, which is a much smaller matrix comparing to $\mathbf{D}^{(i)}$ or $\mathbf{F}$. The elements in $\mathbf{D}$ are phasors of the form $e^{j\theta}$, $\theta \in [0, 2\pi]$,whose magnitudes are equal to 1. With this condition, the dithered sequence $\mathbf{x}^{(i)}$ has the same power as $\mathbf{x}$. Let $\mathbf{d}_i^{\mathrm{r}}$ and $\mathbf{d}_i^{\mathrm{c}}$ denote the i^{th} row and the i^{th} column of $\mathbf{D}$, respectively, such that $\mathbf{d}_i^{\mathrm{r}}$ is a row vector of length M and $\mathbf{d}_i^{\mathrm{c}}$ is a column vector of length M. Specifically,

$$\begin{aligned}
\mathbf{D} &\triangleq \begin{bmatrix} d_{11} & d_{12} & \dots & d_{1M} \\ d_{21} & d_{22} & \dots & d_{2M} \\ \vdots & \vdots & \ddots & \vdots \\ d_{M1} & d_{M2} & \dots & d_{MM} \end{bmatrix}_{M\times M} \\
&= \begin{bmatrix} — & \mathbf{d}_1^{\mathrm{r}} & — \\ — & \mathbf{d}_2^{\mathrm{r}} & — \\ & \vdots & \\ — & \mathbf{d}_M^{\mathrm{r}} & — \end{bmatrix}_{M\times M} \qquad (2.4) \\
&= \begin{bmatrix} | & | & & | \\ \mathbf{d}_1^{\mathrm{c}} & \mathbf{d}_2^{\mathrm{c}} & \dots & \mathbf{d}_M^{\mathrm{c}} \\ | & | & & | \end{bmatrix}_{M\times M} \qquad (2.5)
\end{aligned}$$

The i^{th} dithering sequence, $\mathbf{d}^{(i)}$ in Eq. (2.1), is constructed by repeating and concatenating the i^{th} row of $\mathbf{D}$ until its length is L_{x}. In particular,

$$\mathbf{d}^{(i)} \triangleq \underbrace{\begin{bmatrix} — & \mathbf{d}_i^{\mathrm{r}} & — & \mathbf{d}_i^{\mathrm{r}} & — & \dots & — & \mathbf{d}_i^{\mathrm{r}} & — \end{bmatrix}^{\mathrm{T}}}_{\text{repeated } \frac{L_{\mathrm{x}}}{M} \text{ times}}. \qquad (2.6)$$

The dithering matrix $\mathbf{D}^{(i)}$, in Eq. (2.2), has the same size as matrix $\mathbf{F}$ and is obtained by stacking

the dither vector $\frac{L_x}{\beta}$ times.

$$\mathbf{D}^{(i)} \triangleq \begin{bmatrix} — & \mathbf{d}_i^{\mathrm{r}} & — & \mathbf{d}_i^{\mathrm{r}} & — & \dots & — & \mathbf{d}_i^{\mathrm{r}} & — \\ — & \mathbf{d}_i^{\mathrm{r}} & — & \mathbf{d}_i^{\mathrm{r}} & — & \dots & — & \mathbf{d}_i^{\mathrm{r}} & — \\ & \vdots & & \vdots & & \ddots & & \vdots & \\ — & \mathbf{d}_i^{\mathrm{r}} & — & \mathbf{d}_i^{\mathrm{r}} & — & \dots & — & \mathbf{d}_i^{\mathrm{r}} & — \end{bmatrix}_{\frac{L_x}{\beta} \times L_x} \tag{2.7}$$

Next, we combine signal modulation with channel modulation to obtain a coupled channel model.

2.3 Matrix Representation of the General Communication Model

We adopt the same system model as described in [9]. The channel is modeled as a discrete time system, whose input and output are related by,

$$\mathbf{y}[k] = \mathbf{H}[k]\tilde{\mathbf{x}}[k] + \mathbf{n}[k], \tag{2.8}$$

where the index k indicates the k^{th} symbol. Assume we transmit one symbol per time period, k also corresponds to the k^{th} decoding time period. For each k, $\tilde{\mathbf{x}}[k] \in \mathbb{C}^{L_x}$; and $\mathbf{y}[k]$, $\mathbf{n}[k] \in \mathbb{C}^{L_y}$ are a slice of channel symbols related by ISI through the channel impulse response matrix $\mathbf{H}[k] \in \mathbb{C}^{\{L_y \times L_x\}}$. Here, L_x and L_y denote the lengths of $\tilde{\mathbf{x}}$ and $\mathbf{y}$ respectively. More specifically, $\tilde{\mathbf{x}}[k]$ is a segment of the transmitted data vector containing the k^{th} symbol and its neighbors. In particular, for a channel of N_a anticausal taps and N_c causal taps; and with a feedforward filter of L_a anticausal taps and L_c causal taps,

$$\tilde{\mathbf{x}}[k] \triangleq [\tilde{x}[k - L_c - N_c + 1], \dots, \tilde{x}[k], \dots, \tilde{x}[k + L_a + N_a]]^{\mathrm{T}}. \tag{2.9}$$

The vector $\mathbf{n}[k]$ is a sequence of AWGN samples with variance σ_n^2 and is defined as

$$\mathbf{n}[k] \triangleq [n[k - L_c + 1], \dots, n[k], \dots, n[k + L_a]]^{\mathrm{T}}. \tag{2.10}$$

Lastly, $\mathbf{y}[k]$ is a segment of the received data, given by

$$\mathbf{y}[k] \triangleq [y[k - L_c + 1], \dots, y[k], \dots, y[k + L_a]]^{\mathrm{T}}. \tag{2.11}$$

The general discrete model assumes the channel to be time-varying. Hence, the channel is modeled by allowing $\mathbf{H}[k]$ to change with k.

2.4 Channel Matrix Model with SNQ Modulation

The received signal and the transmitted signal for the i^{th} redundancy block are related by,

$$\mathbf{y}^{(i)}[k] = \mathbf{H}^{(i)}[k]\tilde{\mathbf{x}}^{(i)}[k] + \mathbf{n}^{(i)}[k]. \tag{2.12}$$

Combining Eqs (2.12), (2.1) and (2.2), we couple the SNQ modulator with the channel impulse response in the following way,

$$\begin{aligned}
\mathbf{y}^{(i)}[k] &= \mathbf{H}^{(i)}[k](\mathbf{F}^{(i)}[k]\mathbf{x}[k]) + \mathbf{n}^{(i)}[k] && (2.13)\\
&= \mathbf{H}^{(i)}[k](\mathbf{F}(\mathbf{x}[k] \circ \mathbf{d}^{(i)}[k])) + \mathbf{n}^{(i)}[k] && (2.14)\\
&\triangleq \mathbf{G}^{(i)}[k](\mathbf{x}[k] \circ \mathbf{d}^{(i)}[k]) + \mathbf{n}^{(i)}[k] && (2.15)\\
&= \mathbf{G}^{(i)}[k] \circ \mathbf{D}^{(i)}[k](\mathbf{x}[k]) + \mathbf{n}^{(i)}[k] && (2.16)\\
&= {\mathbf{G}^{(i)}}^{\dagger}[k]\mathbf{x}[k] + \mathbf{n}^{(i)}[k], && (2.17)
\end{aligned}$$

where Eq. (2.13) follows by substituting Eq. (2.3) into Eq. (2.12); Eq. (3.2) separates the modulation and the dithering procedure from $\tilde{\mathbf{x}}^{(i)}[k]$; Eq. (2.15) combines the pulse shape modulation step with the channel impulse matrix; Eq. (2.16) follows from (2.2). Lastly, Eq. (2.17) combines the signal modulation procedure and the channel modulation step into a single transformation matrix $\mathbf{G}^{(i)}[k]$, given by,

$$\mathbf{G}^{(i)}[k] \triangleq \mathbf{H}^{(i)}[k]\mathbf{F}. \tag{2.18}$$

Moreover, as in Eq. (2.17), ${\mathbf{G}^{(i)}}^{\dagger}[k]$ further includes the effect of the dithering matrix for the i^{th} redundancy block and is defined as

$${\mathbf{G}^{(i)}}^{\dagger}[k] \triangleq \mathbf{G}^{(i)}[k] \circ \mathbf{D}^{(i)}[k]. \tag{2.19}$$

Note that the rows of $\mathbf{G}^{\dagger}[k]$ are composed of impulse response vectors, which are appropriately positioned with leading and trailing zeros, as defined in Eq. (1.5). Here, $\mathbf{x}[k]$, $\mathbf{y}[k]$ and $\mathbf{n}[k]$ are

defined in a similar way as in Eqs. (2.9) to (2.11), except that N_c and N_a now represent the causal and anticausal components of the coupled channel impulse response. Similarly, the dithering sequence $\mathbf{d}^{(i)}[k]$ is a segment of the dithering vector $\mathbf{d}^{(i)}$ and it is defined as

$$\mathbf{d}^{(i)}[k] \triangleq \left[d^{(i)}[k - L_c - N_c + 1], \ldots, d^{(i)}[k], \ldots, d^{(i)}[k + L_a + N_a]\right]^{\mathrm{T}}. \tag{2.20}$$

Now, let us generalize Eq. (2.17) to represent M redundancy blocks. The received blocks and $\mathbf{x}$ are related by,

$$\mathbf{y}[k] \triangleq \begin{bmatrix} \mathbf{y}^{(1)}[k] \\ \mathbf{y}^{(2)}[k] \\ \vdots \\ \mathbf{y}^{(M)}[k] \end{bmatrix} = \begin{bmatrix} {\mathbf{G}^{(1)}}^{\dagger}[k]\mathbf{x}[k] + \mathbf{n}^{(1)}[k] \\ {\mathbf{G}^{(2)}}^{\dagger}[k]\mathbf{x}[k] + \mathbf{n}^{(2)}[k] \\ \vdots \\ {\mathbf{G}^{(M)}}^{\dagger}[k]\mathbf{x}[k] + \mathbf{n}^{(M)}[k] \end{bmatrix} \tag{2.21}$$

$$\triangleq \mathbf{G}^{\dagger}[k]\mathbf{x}[k] + \mathbf{n}[k], \tag{2.22}$$

where the matrix $\mathbf{G}^{\dagger}$ denote the cascade of the individual transformation matrices.

We have now constructed a matrix model for the SNQ scheme, which will facilitate our derivations of an optimal SNQ decoder in the following section.

2.5 Demodulator

The block diagram for the demodulator is shown in Figure 2-1. Similar to the modulator, the demodulator bridges the interfaces between the received signal $\mathbf{y}$ and the decision codeword $\hat{\mathbf{x}}_c(\mathbf{w})$. The demodulation procedure for ISI channel uses such techniques as the minimum-mean-squared-error decision-feedback-equalizer (MMSE-DFE) to remove ISI, after which the soft decision $\hat{\mathbf{x}}_s$ is then mapped to its closest constellation symbol using a hard decision device (also called a slicer). The hard decision vector $\hat{\mathbf{x}}$ is finally converted to binary bits with a QAM demodulator. In the remaining of this section, we explain the DFE structure in detail and investigate a variety of

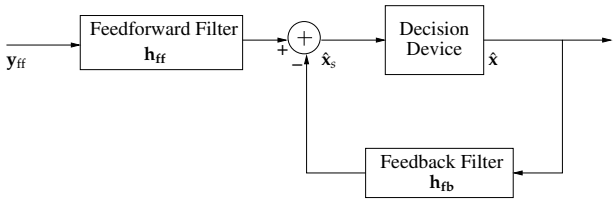

Figure 2-4: One-channel decision-feedback-equalizer

DFE implementations.

2.5.1 Single Channel MMSE Decision-Feedback-Equalizer

The MMSE-DFE structure, under the assumption of perfect feedback, is a capacity achieving receiver for the Gaussian ISI channel, [8] and [10]. The MMSE-DFE consists of a feedforward filter, a feedback filter and a hard-decision device. It converts the ISI channel into a memoryless Gaussian channel. Both the feedforward and the feedback filters operate at symbol rate (i.e. generates one output per symbol). Since the received signals are limited by the channel bandwidth, Nyquist rate samples provide a sufficient statistic for estimating the transmitted codeword. Nevertheless, without additional up-sampling or down-sampling, the time-domain MMSE-DFE requires one sample input per output. In other words, with SNQ signaling rate β, the filters operate at a fractional sampling rate of β (i.e. the input signal are sampled at β times of the Nyquist rate). The drawback of over-sampling is that it results in a large portion of free parameters (i.e. (1-β)/β of the parameters are free to take any value). In the frequency domain, this translates into a band of zero parameters. In the adaptive DFE scheme, the extra free parameters will slow down the convergence rate and may also introduce extra estimation error if the filter coefficients are not fully adapted. To avoid these negative effects, we adopt a frequency-domain equalization scheme, which will be introduced in Section 2.5.5.

A single channel DFE structure is shown in Figure 2-4. Let $\mathbf{h}_{\mathrm{ff}}$ and $\mathbf{h}_{\mathrm{fb}}$ denote the feedforward and feedback filter coefficients, with lengths L_{ff} and L_{fb}, respectively. Define $\mathbf{y}_{\mathrm{ff}}[k]$ to be a vector of the received data samples with length L_{ff} such that

$$\mathbf{y}_{\mathrm{ff}}[k] \triangleq [y[k + L_{\mathrm{ff}} - 1], \ldots, y[k]]^{\mathrm{T}},$$

and $\hat{\mathbf{x}}_{\text{fb}}[k]$ to be a vector of past estimates of the transmitted signal given by,

$$\hat{\mathbf{x}}_{\text{fb}}[k] \triangleq [\hat{x}[k-1], \ldots, \hat{x}[k-L_{\text{fb}}]]^{\text{T}}.$$

Then, the soft-decision of the k^{th} transmitted data symbol $x[k]$ given by the MMSE-DFE can be computed as follows,

$$\hat{x}_s[k] = \mathbf{h}_{\text{ff}}[k]^{\text{H}}\mathbf{y}_{\text{ff}}[k] + \mathbf{h}_{\text{fb}}[k]^{\text{H}}\hat{\mathbf{x}}_{\text{fb}}[k]. \tag{2.23}$$

The finite length input of a feedforward filter (i.e. $\mathbf{y}_{\text{ff}}$) is defined above as a segment of the received signal. For notation conveniences, we omit the subscript in $\mathbf{y}_{\text{ff}}$ in the following chapters. We now have a structure that produces symbol-wise estimates of $\mathbf{x}$. Next, we explain how the DFE coefficients are computed.

2.5.2 The Optimal MMSE-DFE

The optimal MMSE-DFE has coefficients that satisfy the following constraint

$$\hat{\mathbf{h}}[k] = \underset{\mathbf{h}}{\text{argmin}}\ \mathbb{E}[|x[k] - \mathbf{h}^{\text{H}}\tilde{\mathbf{y}}[k]|^2],$$

where $\mathbf{h}[k] = \begin{bmatrix} \mathbf{h}_{\text{ff}}[k] \\ \mathbf{h}_{\text{fb}}[k] \end{bmatrix}$; $x[k]$ is the k^{th} transmitted data symbol, and $\tilde{\mathbf{y}}[k] = \begin{bmatrix} \mathbf{y}_{\text{ff}}[k] \\ \hat{\mathbf{x}}_{\text{fb}}[k] \end{bmatrix}$.

Given the channel impulse matrix and the AWGN variance (σ_n^2), the feedforward filter coefficients ($\mathbf{h}_{\text{ff}}$) and the feedback filter coefficients ($\mathbf{h}_{\text{fb}}$) of the MMSE DFE can be computed. First, we decompose $\mathbf{H}[k]$ into three parts in the following manner:

$$\mathbf{H}[k] = [\mathbf{H}_{\text{fb}}[k] \quad \mathbf{h}_0[k] \quad \mathbf{H}_0[k]], \tag{2.24}$$

where $\mathbf{H}_{\text{fb}}[k]$ corresponds to the causal portion of the channel impulse matrix; $\mathbf{h}_0[k]$ is the channel impulse vector that corresponds to the current decoding symbol; and $\mathbf{H}_0[k]$ is the anticausal portion of the channel impulse matrix.

Then, as shown in [9], the MMSE-DFE coefficients are given by Eqs (2.25) and (2.26):

$$\mathbf{h}_{\text{ff}}[k] = \frac{\mathbf{Q}^{-1}[k]\mathbf{h}_0[k]}{1 + \mathbf{h}_0^{\text{H}}[k]\mathbf{Q}^{-1}[k]\mathbf{h}_0[k]}, \tag{2.25}$$

$$\mathbf{h}_{\text{fb}}[k] = -\mathbf{H}_{\text{fb}}^{\text{H}}[k]\mathbf{h}_{\text{ff}}[k], \tag{2.26}$$

where $\mathbf{Q}[k] \triangleq \sigma_n^2\mathbf{I} + \mathbf{H}_0[k]\mathbf{H}_0^{\text{H}}[k]$.

2.5.3 RLS Adaptive Equalizer

For a time-varing channel, the channel impulse response is usually unknown to the receiver and the optimal MMSE-DFE coefficients cannot be computed in advance. As a result, we adopt the Recursive-Least-Squares (RLS) adaptive equalizer, which minimizes the *exponentially weighted least square* with the cost function

$$\hat{\mathbf{h}}[k] = \underset{\mathbf{h}}{\text{argmin}} \sum_{i=1}^{k} \lambda^{k-i} |\mathbf{x}[k] - \mathbf{h}^{\text{H}}\tilde{\mathbf{y}}[k]|^2,$$

where λ, a positive constant, is the *exponential weighting factor* or *forgetting factor*. The memory of the algorithm is approximately $\frac{1}{1-\lambda}$. For example, when λ is set to 1, the algorithm has infinite memory which means all the past symbols are accounted and weighted equally. If the channel is time-invariant and as k, the number of received data symbols, increases, the *exponentially weighted least square* solution converges to the MMSE solution [11].

There are three parameters associated with the adaptive RLS-DFE that affect its performance. They are the feedforward filter length, feedback filter length and the forgetting factor λ. If the channel impulse response is known, the exact values of the MMSE-DFE coefficients can be computed [9]. In contrast, when the channel is time-varying and not known exactly, we can only set the parameters for the RLS-DFE based on general rules. For example, the feedback filter aims to remove the ISI caused by the channel thus its length should be approximately equal to the main power envelope of the channel impulse response. The total length of the feedforward and the feedback filters together should be approximately equal to the length of the channel impulse response. The forgetting factor governs the memory of the DFE, which is approximately $\frac{1}{1-\lambda}$. When the channel is fast varying, λ should be set small so that the DFE has a short memory. When the

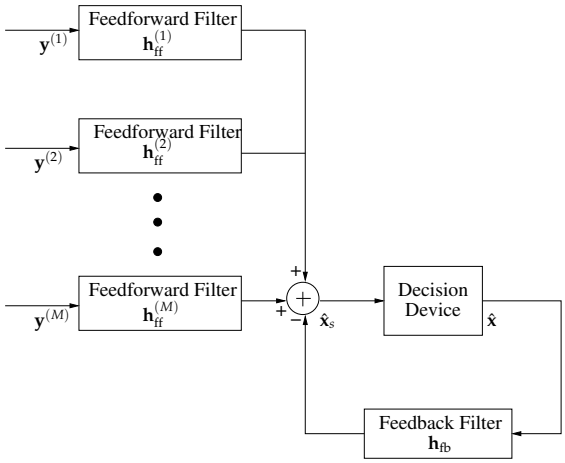

Figure 2-5: Multi-channel decision-feedback-equalizer with joint decoding

channel SNR is low, λ should be set close to 1 such that the DFE's long memory will average out the effect of noise. The resulting DFE coefficients from these parameter settings may have small discrepancy from the optimal MMSE DFE coefficients.

2.5.4 Equalization with Multiple Redundancy Blocks

In our proposed SNQ scheme, multiple redundancy blocks are generated from the same source codeword $\mathbf{x}$, and after being received sequentially by the receiver, $\{\mathbf{y}^{(1)}, \mathbf{y}^{(2)}.....\mathbf{y}^{(M)}\}$ are combined in parallel to recover $\mathbf{x}$. We adopt the standard adaptive multi-channel combining DFE structure, whose full description and analysis can be found in [12]. The multi-channel MMSE-DFE consists of M feedforward filters each with length L_{ff} and a feedback filter with length L_{fb}. The structure of the multi-channel DFE is shown in Figure 2-5.

Similar to the single-channel MMSE-DFE, the multi-channel MMSE-DFE has coefficients that minimize the mean square error of the estimate,

$$\hat{\mathbf{h}}[k] = \underset{\mathbf{h}}{\text{argmin}}\ \mathbb{E}[|\mathbf{x}[k] - \mathbf{h}^{\text{H}}\tilde{\mathbf{y}}[k]|^2],$$

$$\text{where } \mathbf{h}[k] \triangleq \begin{bmatrix} \mathbf{h}_{\text{ff}}[k] \\ \mathbf{h}_{\text{fb}}[k] \end{bmatrix} \triangleq \begin{bmatrix} \mathbf{h}_{\text{ff}}^{(1)}[k] \\ \vdots \\ \mathbf{h}_{\text{ff}}^{(M)}[k] \\ \mathbf{h}_{\text{fb}}[k] \end{bmatrix} \text{ and } \tilde{\mathbf{y}}[k] \triangleq \begin{bmatrix} \mathbf{y}_{\text{ff}}[k] \\ \hat{\mathbf{x}}_{\text{fb}}[k] \end{bmatrix} \triangleq \begin{bmatrix} \mathbf{y}_{\text{ff}}^{(1)}[k] \\ \vdots \\ \mathbf{y}_{\text{ff}}^{(M)}[k] \\ \hat{\mathbf{x}}_{\text{fb}}[k] \end{bmatrix}.$$

Then, the soft-decision of the k^{th} transmitted data symbol $x[k]$ can be computed with

$$\hat{x}_s[k] = \mathbf{h}^{\text{H}}[k]\tilde{\mathbf{y}}[k]. \tag{2.27}$$

This generalizes to a multiple hydrophone (receiver) structure, which is implemented in Section 2.7.1.

2.5.5 Frequency Domain DFE

The multi-channel-equalization structure, introduced in section 2.5.4, converges to the optimal MMSE estimator of the transmitted information sequence, under the assumptions that: (1) the channel is time-invariant during the transmission time-frame of each redundancy block; (2) the block length of the training symbols are sufficiently long such that the equalizer coefficients are fully adapted; and (3) the channel condition yields a sufficiently high slicer SNR such that the equalizer does not run into a failure mode. Unfortunately, these assumptions cannot always be satisfied under practical conditions. For example, the filter convergence time increases with the length of the filter taps. In a rapidly varying environment, the communication system may not have sufficient time to adapt the equalizer to its optimal coefficients. As a result, it is essential to avoid using extra filter taps. Due to the intrinsic nature of the symbol-by-symbol decoding scheme, the decoder requires at least one output sample from the equalizer for each symbol. As explained earlier in Section 2.5.1, this constraint implies that the number of taps increases linearly with the SNQ signaling rate, among which a large portion are free parameters which may introduce estimate errors and decrease coefficients convergence rate. To overcome this inefficiency of the SNQ scheme, we adopt the frequency domain equalizer structure, whose optimal number of filter taps is constant with respect to the SNQ signaling rate and is chosen to be minimal such that the filter only operates on the useful bandwidth of the signal. In particular, the frequency domain DFE computes the discrete Fourier Transform (DFT) of the received signal and then performs equalization in the frequency domain [13]. Since both the Nyquist and the SNQ signals occupy

the same frequency band, the number of filter coefficients is now independent of the signal rate.

Let $\mathbf{Y}_j^{(i)}[k]$, $i \in \{1, 2, \ldots, M\}$ and $j \in \{1, 2, \ldots, N\}$, represent the DFT of the received signal vector of the i^{th} redundancy block at hydrophone j. Here, M is the total number of redundancy blocks and N is the total number of receive hydrophones.The optimal frequency-domain equalizer coefficients minimize the mean square error of the estimate, specifically,

$$\hat{\mathbf{h}}[k] = \underset{\mathbf{h}}{\operatorname{argmin}}\, \mathbb{E}[|x[k] - \mathbf{h}^{\mathrm{H}}\tilde{\mathbf{Y}}[k]|^2],$$

where $\tilde{\mathbf{Y}}(k) = \begin{bmatrix} \mathbf{Y}_{\text{ff}}^{(1)}[k] \\ \vdots \\ \mathbf{Y}_{\text{ff}}^{(M)}[k] \\ \hat{\mathbf{X}}_{\text{fb}}[k] \end{bmatrix}$; $\hat{\mathbf{X}}_{\text{fb}}[k]$ and $\mathbf{Y}^{(i)}[k]$ are vectors representing the DFT of $\hat{\mathbf{x}}_{\text{fb}}[k]$ and $\mathbf{y}^{(i)}[k]$, respectively. The $M \times N$ signal vectors are combined linearly to produce the soft-decision of the transmitted symbol, which is given by,

$$\hat{x}[k] = \sum_{j=1}^{N} \sum_{i=1}^{M} [\mathbf{h}_{\{\text{ff},j\}}^{(i)}]^{\mathrm{T}} \mathbf{Y}_j^{(i)}[k] + \mathbf{h}_{\text{fb}}^{\mathrm{T}} \hat{\mathbf{X}}_{\text{fb}}[k]. \tag{2.28}$$

2.5.6 Delayed Frequency Domain DFE

Another important practical consideration is that the conventional DFE makes decisions on individual symbols independently at each time instance. If the value of the leading filter taps are large, a single error may affect the decision on the next symbol significantly and thus introducing error into subsequent symbols. This way, the error propagates and may cause the filter to go into a failure mode. In order to penalize error propagation and prevent the equalizer from being trapped into the failure mode, we utilize the delayed-decision structure [14] in our frequency domain DFE, such that the hard-decision $\hat{x}[k]$ is made jointly with neighboring soft-decision symbols $\{\hat{x}_{\text{s}}[k], \ldots, \hat{x}_{\text{s}}[k + D]\}$. Specifically, $\hat{x}[k]$ is the the k^{th} element of $\hat{\mathbf{x}}$, which satisfies the following minimization function:

$$\hat{\mathbf{x}} = \underset{\mathbf{x}[i] \in \mathbb{S}^D}{\operatorname{argmin}} \sum_{i=k}^{i=k+D} (x[i] - \hat{x}_s[i])^2, \tag{2.29}$$

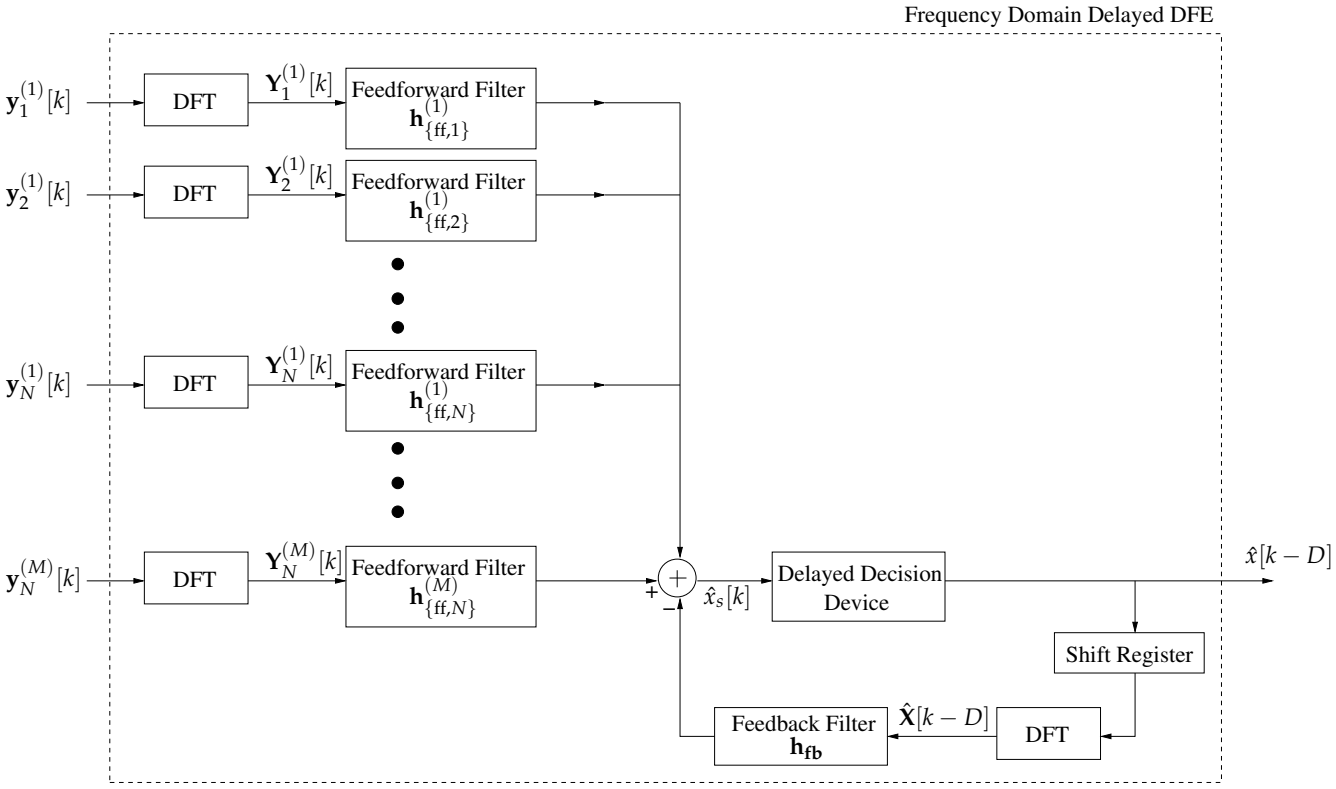

Figure 2-6: Delayed Frequency Domain DFE

where $\mathbb{S}$ denotes the symbol space of the QAM constellation and $\mathbf{x}[i]$ is a vector of length D. Under this setup, the value of $\mathbf{x}[i]$ will affect the next soft decision $\hat{\mathbf{x}}_s[i+1]$ when there is ISI between the two symbols; and an incorrect hard decision on the current symbol will be penalized on the next symbol decision.

The block diagram of the delayed-frequency domain DFE is shown in Figure 2-6. With delay step equal to D, the decision on the past symbol $\hat{x}[k-D]$ is made at time instance k. Appendix A shows an example of the delayed-decision making procedure when the decision process is postponed by $D = 1$ symbol step.

2.6 MMSE-DFE Structure for SNQ Signaling with DFT Dithering

In Section 2.3, we sketched the discrete-time model of the communication system, where data is transmitted through a time-varying channel with multi-path scattering and white noise. The received signal is then processed with a DFE to produce the MMSE estimate of the transmitted data

sequence. When the channel is time-invariant, the channel impulse response can be estimated and the optimal MMSE-equalizer coefficients can be computed from Eqs. (2.25) and (2.26). Under a time-varying communication environment, our decoder system incorporates the RLS adaptive equalization structure. The equalizer coefficients adapt according to the slicer error at each step and the forgetting factor, λ, controls the memory of the equalizer. For a fast-varying channel, λ is set to be small that each adaptation step is large; whereas a large λ is used for a slow-varying channel. Although the system is prone to time-varying channels, the underlying assumption is that the convergence time of the equalizer is much smaller than the coherence-time of the channel, thus the channel is effectively time-invariant during short time frames.

This assumption is violated when we take the effect of dithering into consideration, because the dithering sequence is varying at every symbol time. Consequently, the adaptive equalization structures introduced previously generally cannot be directly applied to the dithered-SNQ scheme. The following section presents a solution to this problem – a simple modified adaptive DFE structure (Figure 2-7), which inverts the time-varying effects caused by the dither and computes the MMSE estimates for the dithered SNQ repetition coding scheme under the special case of DFT dithering.

Although many other dithering schemes also yield capacity-achieving performances, we deliberately select the $R \times R$, $R \in \mathbb{N}$, DFT matrix as our base matrix $\mathbf{D}$, because special properties of the DFT matrix enable us to derive this simple and, more importantly, time-invariant receiver structure. If we choose R to be at least M, each redundancy block $\mathbf{x}^{(i)}$ will be dithered with a different dithering sequence $\mathbf{d}^{(i)}$. Then, the decoder jointly combines the M redundancy blocks. Although the general underwater channel is time-varying, we impose the assumption that the channel coherence time is much longer than the transmission time of each packet such that $\mathbf{G}^{(i)}$, and the noise variance of the Gaussian ISI channel, denoted by ${\sigma_n}^2$, is constant during each frame, but can vary over different packet frames. Specifically,

$$\mathbf{G}^{(i)}[k+1] = \mathbf{G}^{(i)}[k], \qquad \forall k. \tag{2.30}$$

Only if this condition is met, will the adaptive equalization algorithm be viable and efficient.

Let us decompose $\mathbf{G}^{\dagger}[k]$ into three parts as described in Eq. (2.24):

$$\mathbf{G}^{\dagger}[k] \triangleq \left[\mathbf{G}_{\text{fb}}{}^{\dagger}[k] \quad \mathbf{g}_0{}^{\dagger}[k] \quad \mathbf{G}_0{}^{\dagger}[k] \right]. \tag{2.31}$$

The MMSE-DFE receiver is capacity-achieving for the Gaussian ISI channel. With dithering, the optimal MMSE-DFE consists of M time-varying feedforward filters, each denoted by $\mathbf{h}_{\text{ff}}^{(i)}[k]$; and one time-invariant feedback filter, denoted by $\mathbf{h}_{\text{fb}}[k]$. Let $\mathbf{h}_{\text{ff}}[k]$ be a vector that is composed of the M feedforward filters. The length of $\mathbf{h}_{\text{ff}}[k]$ is equal to $M \times L_{\text{ff}}$. Applying Eqs. (2.25) and (2.26) to the discrete model represented by Eq. (2.22), the feedforward filter coefficients at the initial time ($k = 0$) are given by,

$$\begin{aligned} \mathbf{h}_{\text{ff}}[0] &\triangleq \begin{bmatrix} \mathbf{h}_{\text{ff}}^{(1)}[0] \\ \mathbf{h}_{\text{ff}}^{(2)}[0] \\ \vdots \\ \mathbf{h}_{\text{ff}}^{(M)}[0] \end{bmatrix} \\ &= \frac{\mathbf{Q}^{-1}[0]\mathbf{g}_0[0]}{1 + \mathbf{g}_0^{\text{H}}[0]\mathbf{Q}^{-1}[0]\mathbf{g}_0[0]}, \end{aligned} \tag{2.32}$$

where $\mathbf{Q}[0] \triangleq \sigma_n^2\mathbf{I} + \mathbf{G}_0^{\dagger}[0]\mathbf{G}_0^{\dagger\text{H}}[0]$, and ${\sigma_n}^2$; the feedback filter coefficients are

$$\mathbf{h}_{\text{fb}}[0] \triangleq \left[\mathbf{h}_{\text{fb}}^{(1)}[0] + \mathbf{h}_{\text{fb}}^{(2)}[0] + \ldots + \mathbf{h}_{\text{fb}}^{(M)}[0] \right], \tag{2.33}$$

where $\mathbf{h}_{\text{fb}}^{(i)}[0]$ is a vector of length L_{fb} and is given by,

$$\begin{bmatrix} \mathbf{h}_{\text{fb}}^{(1)}[0] \\ \mathbf{h}_{\text{fb}}^{(2)}[0] \\ \vdots \\ \mathbf{h}_{\text{fb}}^{(M)}[0] \end{bmatrix} \triangleq -\mathbf{G}_{\text{fb}}^{\dagger\text{H}}[0]\mathbf{h}_{\text{ff}}[0]. \tag{2.34}$$

Theorem 2.1. With DFT dithering, the time-varying feedforward filter coefficients at time k are equal to the feedforward filter coefficients at time 0 multiplied by $\mathbf{d}^{(i)}[k]^*$. More specifically, they are given by

$$\mathbf{h}_{\text{ff}}[k] \triangleq \begin{bmatrix} \mathbf{h}_{\text{ff}}^{(1)}[k] \\ \mathbf{h}_{\text{ff}}^{(2)}[k] \\ \vdots \\ \mathbf{h}_{\text{ff}}^{(M)}[k] \end{bmatrix} = \begin{bmatrix} \mathbf{h}_{\text{ff}}^{(1)}[0]\mathbf{d}^{(1)}[k]^* \\ \mathbf{h}_{\text{ff}}^{(2)}[0]\mathbf{d}^{(2)}[k]^* \\ \vdots \\ \mathbf{h}_{\text{ff}}^{(M)}[0]\mathbf{d}^{(M)}[k]^* \end{bmatrix}. \tag{2.35}$$

The time-invariant feedback filter coefficients are given by,

$$\mathbf{h}_{\text{fb}}[k] = \mathbf{h}_{\text{fb}}[0]. \tag{2.36}$$

The proof for Theorem 2.1 is given in Appendix C. Substituting the filter coefficients into Eq. (2.27), the MMSE-estimate at time k is given by,

$$\hat{x}_{\text{s}}[k] = \begin{bmatrix} \mathbf{h}_{\text{ff}}^{(1)}[0]^{\text{H}} d^{(1)}[k]^* \mathbf{y}_{\text{ff}}^{(1)}[k] \\ \mathbf{h}_{\text{ff}}^{(2)}[0]^{\text{H}} d^{(2)}[k]^* \mathbf{y}_{\text{ff}}^{(2)}[k] \\ \vdots \\ \mathbf{h}_{\text{ff}}^{(M)}[0]^{\text{H}} d^{(M)}[k]^* \mathbf{y}_{\text{ff}}^{(M)}[k] \end{bmatrix} + \mathbf{h}_{\text{fb}}[0]^{\text{H}} \hat{\mathbf{x}}_{\text{fb}}[k]. \tag{2.37}$$

The implementation of Eq. (2.37) is illustrated by Figure 2-7.

2.7 Overall System Architecture

In this section, we show the overall system architecture for a SIMO and a MIMO system, which incorporates a capacity-approaching channel code (i.e. the LDPC code) and includes the D/C and C/D converters, as well as the passband modulator. These systems are tested in experiments and the results are shown in Chapter 4.

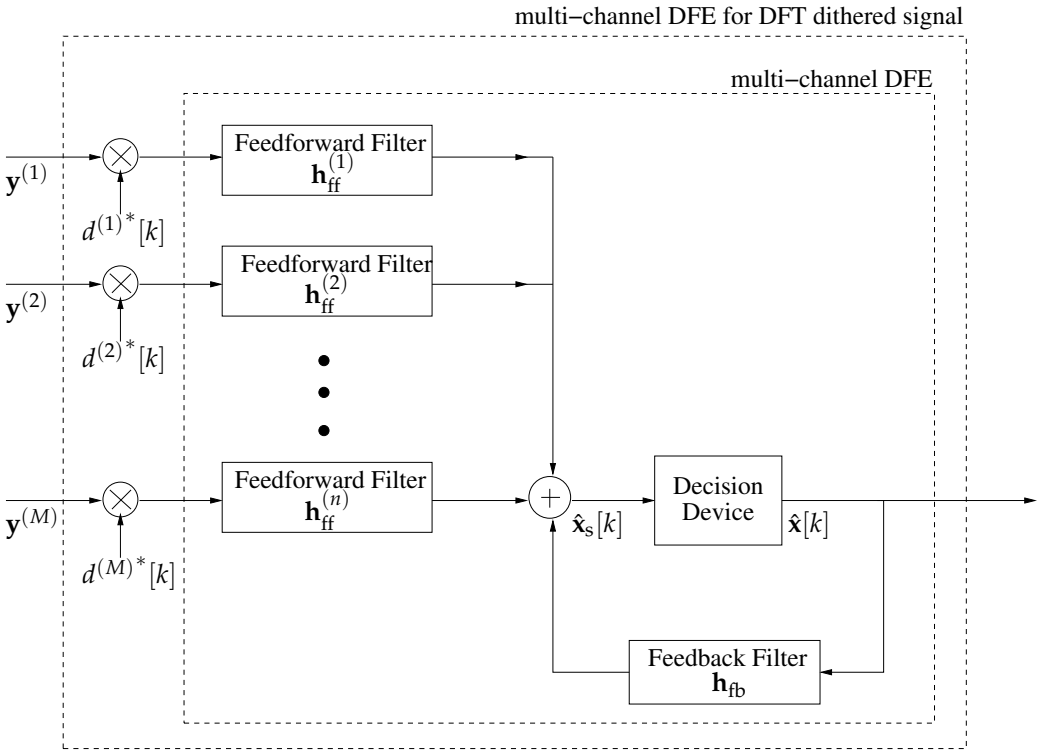

Figure 2-7: Modified multi-channel DFE with joint decoding for DFT dithered scheme

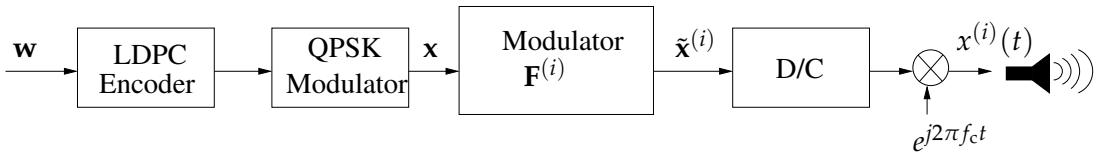

Figure 2-8: SIMO system, transmitter structure

2.7.1 SIMO System Architecture

Figure 2-8 shows the block diagram of the single transducer system. First, we generate a sequence of binary information bits, $\mathbf{w}$. The information bits are coded with a capacity-approaching code. Here, we choose to use the LDPC code at base code rate R_{b}. The output codeword has length 64,800 bits which are modulated with QPSK constellation to 32,400 complex symbols. The modulator, $\mathbf{F}^{(i)}$, dithers the coded symbols, prepends them with synchronization and training symbols and modulates them with a band-limited baseband pulse shape. At the end, the discrete signal is converted to a continuous signal and modulated to passband.

Figure 2-9 shows the decoder structure, which jointly combines multiple received signal packets from different hydrophones and at different times. As shown in the figure, $\mathbf{y}_j^{(i)}(t)$ denotes the

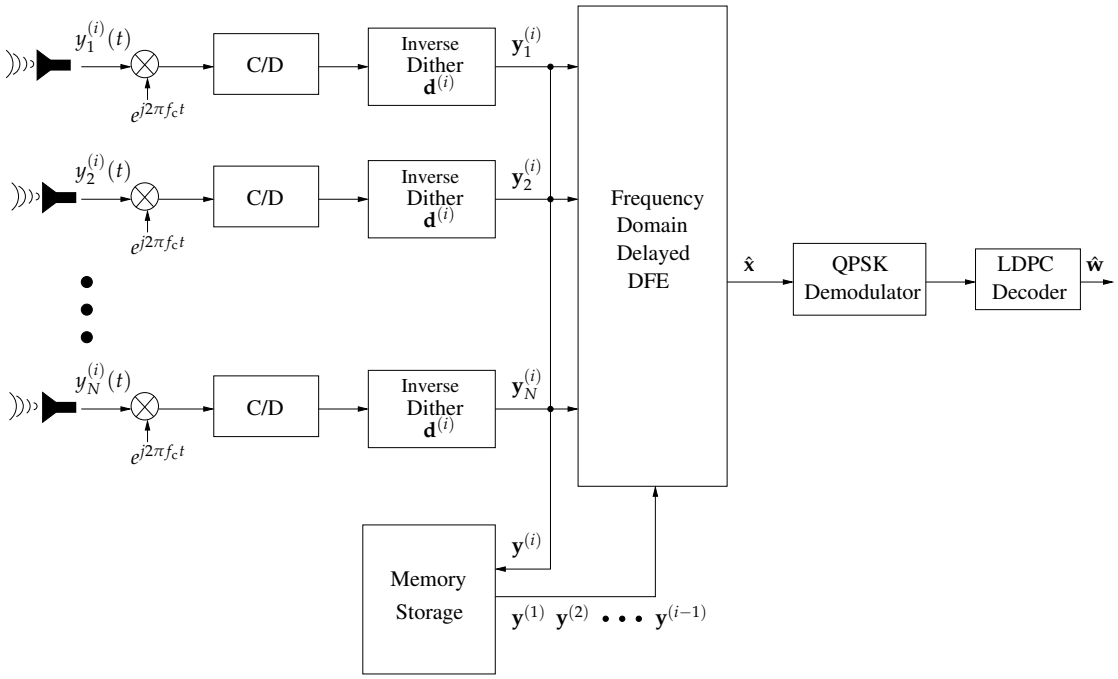

Figure 2-9: SIMO system, receiver structure

received signal of the i^{th} redundancy block at the j^{th} receive hydrophone. After modulating the received signals to the baseband, the decoding structure exploits the special property of the DFT dithered signals as introduced in Section 2.6 and the frequency-domain-delayed equalizer shown in Figure 2-9. Let $\mathbf{y}^{(i)} \triangleq [\mathbf{y}_1^{(i)}, \ldots, \mathbf{y}_N^{(i)}]^{\mathrm{T}}$ denote the concatenation of all the received signal vectors for the i^{th} redundancy block. The memory storage device stores all the past redundancy packets corresponding to the same codeword and pass them to the joint decoder at the next iteration.

2.7.2 MIMO System Architecture

Figure 2-10 depicts the transmit structure of the SNQ scheme under MIMO channels (i.e. the SNQ-MIMO scheme). Similar to the single transducer system, the information message $\mathbf{w}$ is encoded with LDPC code to a binary block of length 64,800 bits, mapped to QPSK constellation, dithered with DFT dithering string and modulated with a baseband pulse-shape. The next step exploits the multiple transducer structure, where the modulated signal $\tilde{\mathbf{x}}^{(i)}$ is multiplied with orthogonal (DFT) dithers before transmitting. In other words, the dithering procedure is performed twice. First, similar to the single transducer scheme, redundancy blocks transmitted over different time frames are modulated with different dithers $\mathbf{d}^{(i)}$ and the i^{th} redundancy block is denoted by $\tilde{\mathbf{x}}^{(i)}$. Then, at each of the T transducers, $\tilde{\mathbf{x}}^{(i)}$ is dithered again with another set of dithers

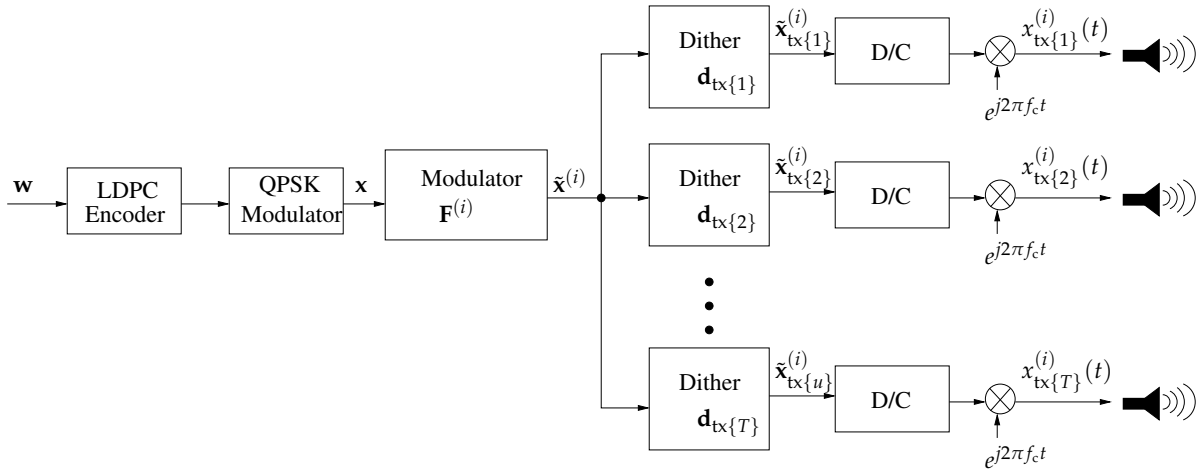

Figure 2-10: MIMO system, transmitter structure.

$\{\mathbf{d}_{\text{tx}\{1\}}, \mathbf{d}_{\text{tx}\{2\}}, \ldots, \mathbf{d}_{\text{tx}\{T\}}\}$ and the outputs are transmitted simultaneously over the MIMO channel. Similar to the redundancy dithers, the second layer dither ($\mathbf{d}_{\text{tx}\{u\}}$, $u \in \{1, 2, \ldots, T\}$) is also formed by concatenating rows of a T by T DFT matrix, and it is therefore a vector of period T. The discrete-time transmit signal at the u^{th} transducer can be expressed by,

$$\tilde{\mathbf{x}}^{(i)}_{\text{tx}\{u\}} = \tilde{\mathbf{x}}^{(i)} \circ \mathbf{d}^{(i)}_{\text{tx}\{u\}}. \tag{2.38}$$

Specifically, with DFT dithering at the transmitter,

$$\tilde{\mathbf{x}}^{(i)}_{\text{tx}\{u\}}[k] = \tilde{\mathbf{x}}^{(i)}[k] e^{j\frac{2\pi u}{T}k}. \tag{2.39}$$

Next, we look at the MIMO decoder structure as shown in Figure 2-11. In Section 2.6, we derived the optimal equalizer coefficients which can be expressed as a function of the time-varying dithering sequence. For the SISO and SIMO systems, the dithering sequences are deterministic and the effects of the dithering procedure can be inverted by inverting the dither before decoding. This does not apply to the MIMO scheme, where the received signal is a linear combination of the transmitted signals from all transducers $\{x^{(i)}_{\text{tx}\{1\}}, x^{(i)}_{\text{tx}\{2\}}, \ldots, x^{(i)}_{\text{tx}\{T\}}\}$. Since the channel is unknown to the receiver before decoding, the dithering coefficients, scaled by a variety of channel gains, cannot be determined and inverted as in the SISO and SIMO cases. In order to remove the time-varying effect of the dither, we utilize the property that the transmit dithering sequences are periodic with period T. As a result of this periodicity in each of the dithers, the combined dither acting on the received signal also has period T. Therefore, we multiplex the received signal into T branches,

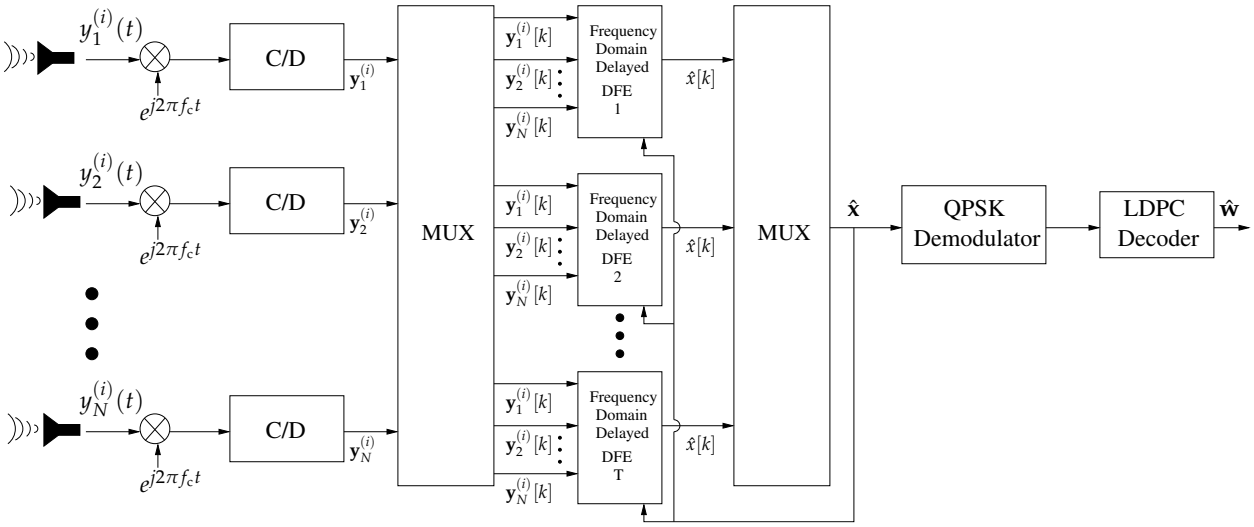

Figure 2-11: MIMO system, receiver structure.

decode each sub-sequence independently (without inverse dither modules) and concatenate the decoded symbols again at the end. The decoder structure of the MIMO system is illustrated in Figure 2-11. The soft-decision at time k is given by,

$$\hat{x}[k] = \sum_{j=1}^{N} \sum_{i=1}^{M} [\mathbf{h}^{(i)}_{\{\mathrm{ff}-\rho,j\}}]^{\mathrm{T}} \mathbf{Y}^{(i)}_{j}[k] + \mathbf{h}^{\mathrm{T}}_{\mathrm{fb}} \hat{\mathbf{X}}_{\mathrm{fb}}[k], \tag{2.40}$$

where ρ indicates the DFE set and $\rho = \mathrm{mod}(k, T)$. One drawback of such a multiplexing scheme is that the DFE coefficients for each set adapts once every T symbols. In other words, the convergence time increases linearly with the number of sub-decoders, and for a time-varying channel, this will impair the system performance.

2.8 Summary

In this chapter, we first presented the components of the SNQ transceiver. The original information bits are first encoded with a capacity-achieving channel code such as the LDPC code. We then apply the dithered repetition coding scheme to each codeword and generate its redundancy packets. In order to introduce orthogonality among the set of redundancy blocks, each codeword is multiplied with a dithering string that is unique to each redundancy block and orthogonal with other dithering strings. A good choice of such dithering strings is to adopt the DFT matrix due to its simple decoding structure and preferable properties. Finally, the redundancy blocks are modulated with a baseband pulse shape and transmitted through a Gaussian band-limited ISI channel.

We then showed the matrix representation of the channel model, which couples the signal modulator and the channel impulse matrix. In Section 2.5.1, we derived an expression for the time-varying DFE filter coefficients, given by Eq. (C.5), which shows the relation among the filter coefficients, channel impulse matrix and the dithering matrix. We then introduced a variety of receiver structures ranging from a simple single-channel RLS adaptive equalizer to the multi-channel frequency domain equalizer with delayed decision device. Under the assumption of a time-invariant channel and perfect feedback, the RLS-adaptive equalizer coefficients converge to the optimal MMSE DFE coefficients.

Due to the time-varying property of the dithering sequence, the standard adaptive DFE structure cannot be applied to the dithered signals directly. Nevertheless, we showed that, with DFT dithering, the time-invariant component and the time-varying components can be separated. Specifically, the time-varying component that is due to the dithering process can be inverted at the beginning of each iteration, leaving the time-invariant DFE coefficients, which adapts after each iteration. The expressions of the feedforward and feedback filter coefficients are given by Eqs. (C.19) and (C.20) and the modified DFE architecture is implemented as in Figure 2-7. We showed that with the simple addition of the inverse dither components at the front end of the multi-channel DFE, we arrive at an optimal decoder structure for the DFT dithered signals. Note that, if the base dithering matrix $\mathbf{D}$ is not the DFT matrix, the filter coefficients are intermingled with dithering coefficients. In this case, the time-varying and time-invariant components of the optimal filter coefficients are difficult to separate. At the end of this chapter, we presented the overall

communication architecture for a practical system, which is used in the KAM11 experiment. The experiment results are shown in Chapter 4.

In the next chapter, we show that under ideal conditions, the SNQ transceiver architecture is capacity achieving. Unfortunately, due to tracking error in the equalizer, error-propagation and potential numerical errors, we are expecting a gap between the actual achievable rate and the channel capacity in practical systems. The analytical and experiment performances of the SNQ system will be shown in Chapters 3 and 4, respectively.

Chapter 3

System Design and Analysis

In Chapter 2, we proposed the SNQ repetition coding scheme with a general dithering sequence and designed the MMSE-DFE decoder structure specifically for the DFT dithered SNQ scheme. In this chapter, we study the properties of the SNQ scheme and analyze its achievable rate. Under the assumption that the channel is time-invariant during the transmission frame of each redundancy block and can be time-varying over multiple blocks, the achievable rate for the SNQ scheme is given in [7]. Here, we derive the bound again with a matrix model and show that the bound is achievable with the proposed decoding structure when the parameters are chosen to be optimal for the channel condition. We first consider the general case in which the dithering matrix is an arbitrary unitary matrix. It is shown that when the number of redundancy blocks (M) is less than or equal to the SNQ signaling rate (β), the channel capacity can be achieved exactly with the SNQ scheme. When the number of redundancy blocks is greater than the signaling rate, we derive an expression for the SNQ achievable rate. Then, we look into the specific case that the dithering matrix is the DFT matrix and show that the DFT dither yields optimal performance among all choices of dithering sequences. At the end of the chapter, we verify the analytical results with simulation.

3.1 Revisit of the Discrete Model Representation

As described by Eq. (2.12), the general discrete channel model of the underwater communication system can be described as,

$$\mathbf{y}^{(i)} = \mathbf{H}^{(i)}\tilde{\mathbf{x}}^{(i)} + \mathbf{n}^{(i)}. \tag{3.1}$$

For notation conveniences, we omit the symbol index k in this chapter. However, we should always keep in mind that, when we write a matrix (e.g. $\mathbf{H}^{(i)}$) or a vector (e.g. $\mathbf{y}^{(i)}$), they are time varying matrices or vectors corresponding to the k^{th} symbol-time. Applying Eq. (2.13), the model can be separated into two steps: signal modulation and channel modulation as follows,

$$\mathbf{y}^{(i)} = \mathbf{H}^{(i)}(\mathbf{F}^{(i)}\mathbf{x}) + \mathbf{n}^{(i)}, \tag{3.2}$$

where $\mathbf{F}^{(i)}$ and $\mathbf{H}^{(i)}$ represent the modulation procedure and channel impulse response for the i^{th} redundancy block, respectively. We begin by assuming that the channel is a perfect band-limited channel with unit power gain. In this case, $\mathbf{H}^{(i)}$ is simply an identity matrix. It will become clear soon that, with SNQ signaling rate β, $\mathbf{H}^{(i)}$ is a matrix of size $\frac{L_x}{\beta} \times \frac{L_x}{\beta}$, and $\mathbf{F}^{(i)}$ is a matrix of size $\frac{L_x}{\beta} \times L_x$. In addition, $\mathbf{y}^{(i)}$ and $\mathbf{n}^{(i)}$ are both vectors of length $\frac{L_x}{\beta}$. This is because, with SNQ signaling at β times the Nyquist rate, the length of each redundancy block is $\frac{1}{\beta}$ of the length of the information codeword $\mathbf{x}$. Generalize Eq. (3.2) to combine M redundancy blocks, the overall model that couples signal modulation and channel modulation is given by,

$$\mathbf{y} \triangleq \begin{bmatrix} \mathbf{y}^{(1)} \\ \mathbf{y}^{(2)} \\ \vdots \\ \mathbf{y}^{(M)} \end{bmatrix} = \begin{bmatrix} \mathbf{H}^{(1)} & \mathbf{0} & \dots & \mathbf{0} \\ \mathbf{0} & \mathbf{H}^{(2)} & \dots & \mathbf{0} \\ \vdots & \vdots & \ddots & \vdots \\ \mathbf{0} & \mathbf{0} & \dots & \mathbf{H}^{(M)} \end{bmatrix} \begin{bmatrix} \mathbf{F}^{(1)} \\ \mathbf{F}^{(2)} \\ \vdots \\ \mathbf{F}^{(M)} \end{bmatrix} \mathbf{x} + \begin{bmatrix} \mathbf{n}^{(1)} \\ \mathbf{n}^{(2)} \\ \vdots \\ \mathbf{n}^{(M)} \end{bmatrix} \tag{3.3}$$

$$\triangleq \mathbf{H}\tilde{\mathbf{F}}\mathbf{x} + \mathbf{n} \tag{3.4}$$

$$\triangleq \mathbf{H}\tilde{\mathbf{x}} + \mathbf{n}$$

where, $\mathbf{H}$ is of size $\frac{ML_x}{\beta} \times \frac{ML_x}{\beta}$ and $\tilde{\mathbf{F}}$ is of size $\frac{ML_x}{\beta} \times L_x$.

As a first step, we isolate the effect of SNQ modulation by assuming a perfect band-limited channel with unit power gain. In this case, $\mathbf{H}$ is an identity matrix and the channel capacity can be achieved iff $\tilde{\mathbf{x}}$ is an i.i.d. Gaussian sequence. By analyzing the modulation procedure, which means studying how $\tilde{\mathbf{x}}$ is related to $\mathbf{x}$ and how the modulation matrix $\tilde{\mathbf{F}}$ is constructed, we show that the SNQ modulated signal $\tilde{\mathbf{x}}$ is indeed an i.i.d. Gaussian sequence.

Figure 2-2 depicts the SNQ modulator, which mainly consists of a redundancy generator that applies a different dither $\mathbf{d}^{(i)}$ to each redundancy block and a SNQ pulse shape modulator $\mathbf{F}$ that is common to all redundancy blocks. In the case of ideal band-limited modulation, the i^{th} row of $\mathbf{F}$ is a vector of the scaled sinc pulse with bandwidth $\frac{1}{\beta}$ and shifted by $i \times \beta$ SNQ periods, which is

equal to $i \times \beta \times \frac{1}{\beta} = i$ Nyquist periods. The elements of $\mathbf{F}$ are specified as follows,

$$\mathbf{F} \triangleq \frac{1}{\sqrt{\beta}} \begin{bmatrix} \operatorname{sinc}(\frac{0-0}{\beta}) & \operatorname{sinc}(\frac{1-0}{\beta}) & \dots & \operatorname{sinc}(\frac{(L_{\mathrm{x}}-1)-0}{\beta}) \\ \operatorname{sinc}(\frac{0-\beta}{\beta}) & \operatorname{sinc}(\frac{1-\beta}{\beta}) & \dots & \operatorname{sinc}(\frac{(L_{\mathrm{x}}-1)-\beta}{\beta}) \\ \operatorname{sinc}(\frac{0-2\beta}{\beta}) & \operatorname{sinc}(\frac{1-2\beta}{\beta}) & \dots & \operatorname{sinc}(\frac{(L_{\mathrm{x}}-1)-2\beta}{\beta}) \\ \vdots & \vdots & \ddots & \vdots \\ \operatorname{sinc}(\frac{0-(\frac{L_{\mathrm{x}}}{\beta}-1)\beta}{\beta}) & \operatorname{sinc}(\frac{1-(\frac{L_{\mathrm{x}}}{\beta}-1)\beta}{\beta}) & \dots & \operatorname{sinc}(\frac{(L_{\mathrm{x}}-1)-(\frac{L_{\mathrm{x}}}{\beta}-1)\beta}{\beta}) \end{bmatrix}_{\frac{L_{\mathrm{x}}}{\beta} \times L_{\mathrm{x}}}$$

$$= \frac{1}{\sqrt{\beta}} \begin{bmatrix} \text{—} & \operatorname{sinc}(\frac{k-0}{\beta}) & \text{—} \\ \text{—} & \operatorname{sinc}(\frac{k-\beta}{\beta}) & \text{—} \\ & \vdots & \\ \text{—} & \operatorname{sinc}(\frac{k-(M-1)\beta}{\beta}) & \text{—} \end{bmatrix}_{\frac{L_{\mathrm{x}}}{\beta} \times L_{\mathrm{x}}}$$

$$= \frac{1}{\sqrt{\beta}} \begin{bmatrix} | & | & & | \\ \operatorname{sinc}(k') & \operatorname{sinc}(k' - \frac{1}{\beta}) & \dots & \operatorname{sinc}(k' - \frac{L_{\mathrm{x}}-1}{\beta}) \\ | & | & & | \end{bmatrix}_{\frac{L_{\mathrm{x}}}{\beta} \times L_{\mathrm{x}}} \tag{3.5}$$

where $k \in \{0, 1, 2, \dots, (L_{\mathrm{x}} - 1)\}$ and $k' \in \{0, 1, 2, \dots, (\frac{L_{\mathrm{x}}}{\beta} - 1)\}$. Next, we incorporate the dithering vector $\mathbf{d}^{(i)}$, given by Eq. (2.20), into the overall signaling modulation matrix $\mathbf{F}^{(i)}$.

The combined modulation matrix $\mathbf{F}^{(i)}$, in Eq. (2.3), is composed of element-wise products of $\mathbf{F}$ and $\mathbf{D}^{(i)}$. The overall modulation matrix $\tilde{\mathbf{F}}$ (as in Eq. (3.4)) combines all the individual modulators $\mathbf{F}^{(i)}$ and it is defined as,

$$\tilde{\mathbf{F}} \triangleq \begin{bmatrix} \mathbf{F}^{(1)} \\ \mathbf{F}^{(2)} \\ \vdots \\ \mathbf{F}^{(M)} \end{bmatrix} = \begin{bmatrix} \mathbf{F} \circ \mathbf{D}^{(1)} \\ \mathbf{F} \circ \mathbf{D}^{(2)} \\ \vdots \\ \mathbf{F} \circ \mathbf{D}^{(M)} \end{bmatrix}_{(M\frac{L_{\mathrm{x}}}{\beta}) \times L_{\mathrm{x}}} \tag{3.6}$$

3.2 Properties of the Modulation Matrix

The modulation matrix $\tilde{\mathbf{F}}$ encompasses key elements of the dithered SNQ scheme and has several special properties that are essential to the design of an optimal system. These properties are shown below through Lemma 1 and Lemma 2.

Lemma 1. Let $\mathbf{f}_m^{\mathrm{c}}$ denote the m^{th} columns of matrix $\mathbf{F}$. Columns $\mathbf{f}_m^{\mathrm{c}}$ and $\mathbf{f}_n^{\mathrm{c}}$, $m \neq n$, are orthogonal iff $(m-n)$ is an integer multiple of β.

Proof. Without loss of generality, assume $m > n$ and let $m - n = N\beta$. We begin by showing that if N is a positive integer, column m and column n are orthogonal. The inner product of $\mathbf{f}_m^{\mathrm{c}}$ and $\mathbf{f}_n^{\mathrm{c}}$ is given by,

$$\begin{aligned}
\langle \mathbf{f}_m^{\mathrm{c}}, \mathbf{f}_n^{\mathrm{c}} \rangle &= \langle \frac{1}{\sqrt{\beta}} \mathrm{sinc}(k' - \frac{m}{\beta}), \frac{1}{\sqrt{\beta}} \mathrm{sinc}(k' - \frac{m+N\beta}{\beta}) \rangle \\
&= \langle \frac{1}{\sqrt{\beta}} \mathrm{rect}(\frac{\omega}{2\pi}) e^{-j\omega\frac{m}{\beta}}, \frac{1}{\sqrt{\beta}} \mathrm{rect}(\frac{\omega}{2\pi}) e^{-j\omega\frac{m}{\beta}} e^{-j\omega N} \rangle \\
&= \frac{1}{2\pi} \int_{-\pi}^{\pi} \left[\frac{1}{\sqrt{\beta}} e^{-j\omega\frac{m}{\beta}} \right] \left[\frac{1}{\sqrt{\beta}} e^{j\omega\frac{m}{\beta}} e^{j\omega N} \right] d\omega \\
&= \left(\frac{1}{2\pi\beta} \right) \left(\frac{2}{N} \right) \sin(N\pi) \qquad (3.7) \\
&= 0
\end{aligned}$$

where Eq. (3.7) follows from the assumption that N is an integer. In contrary, if N is not an integer, $\sin(N\pi) \neq 0$, implying $\mathbf{f}_m^{\mathrm{c}}$ and $\mathbf{f}_n^{\mathrm{c}}$ are not orthogonal. □

We now investigate the property of matrix $\tilde{\mathbf{F}}$. When $M = \beta$, $\tilde{\mathbf{F}}$ is a square matrix of size $L_{\mathrm{x}} \times L_{\mathrm{x}}$. In the following analysis, we assume that L_{x} is sufficiently large and neglect edge effects at the boundary of the matrix.

Lemma 2. When $M = \beta$, $\tilde{\mathbf{F}}$ is an unitary matrix iff $\mathbf{D}$ is a scaled unitary matrix.

Proof. Recall that $\mathbf{D}$ is a $M \times M$ matrix whose elements are phasors with magnitudes = 1. We begin by proving the direct statement: if $\mathbf{D}$ is a scaled unitary matrix such that any two different rows $\mathbf{d}_u^{\mathrm{r}}$ and $\mathbf{d}_v^{\mathrm{r}}$ are orthogonal, then $\tilde{\mathbf{F}}$ is an unitary matrix. As defined in Eq. (3.6), $\tilde{\mathbf{F}}$ is composed of M submatrices $\mathbf{F}^{(i)}$, $i \in \{1, 2, \ldots, M\}$. We divide the proof into three cases:
Case 1: two different rows in two different submatrices are orthogonal. Let $\mathbf{f}_m^{(u)}$ denote the m^{th}

row in submatrix $\mathbf{F}^{(u)}$ and $\mathbf{f}_n^{(v)}$ denote the n^{th} row in submatrix $\mathbf{F}^{(v)}$, $m \neq n$ and $u \neq v$. The inner product of $\mathbf{f}_m^{(u)}$ and $\mathbf{f}_n^{(v)}$ is given by

$$\begin{aligned}
\langle \mathbf{f}_m^{(u)}, \mathbf{f}_n^{(v)} \rangle &= \langle \frac{1}{\sqrt{\beta}} \text{sinc}\left(\frac{k-m\beta}{\beta}\right) \circ \mathbf{d}^{(u)}, \frac{1}{\sqrt{\beta}} \text{sinc}\left(\frac{k-n\beta}{\beta}\right) \circ \mathbf{d}^{(v)} \rangle \\
&= \frac{1}{2\pi} \langle \left(\frac{1}{\sqrt{\beta}}\right)\left(\frac{1}{2\pi}\right) \left\{ \left(\beta \text{rect}(\frac{\omega\beta}{2\pi}) e^{-j\omega m\beta}\right) \otimes \left(\frac{2\pi}{\beta} \sum_{\zeta=0}^{\beta-1} \mathbf{d}_u^{\text{r}}(\zeta+1) \sum_{k=-\infty}^{\infty} \delta(\frac{\omega}{2\pi} - \frac{k}{\beta}) e^{-j\omega\zeta}\right)\right\}, \\
&\qquad \left(\frac{1}{\sqrt{\beta}}\right)\left(\frac{1}{2\pi}\right) \left\{ \left(\beta \text{rect}(\frac{\omega\beta}{2\pi}) e^{-j\omega n\beta}\right) \otimes \left(\frac{2\pi}{\beta} \sum_{\zeta=0}^{\beta-1} \mathbf{d}_v^{\text{r}}(\zeta+1) \sum_{k=-\infty}^{\infty} \delta(\frac{\omega}{2\pi} - \frac{k}{\beta}) e^{-j\omega\zeta}\right)\right\} \rangle \qquad (3.8) \\
&= \frac{1}{2\pi} \langle \left(\frac{1}{\sqrt{\beta}}\right) \left\{ \int_{-\pi}^{\pi} \text{rect}\left(\frac{\theta\beta}{2\pi}\right) e^{-j\theta m\beta} \sum_{\zeta=0}^{\beta-1} \mathbf{d}_u^{\text{r}}(\zeta+1) \sum_{k=-\infty}^{\infty} \delta(\frac{\omega-\theta}{2\pi} - \frac{k}{\beta}) e^{-j(\omega-\theta)\zeta} \text{d}\omega \right\}, \\
&\qquad \left(\frac{1}{\sqrt{\beta}}\right) \left\{ \int_{-\pi}^{\pi} \text{rect}\left(\frac{\theta\beta}{2\pi}\right) e^{-j\theta n\beta} \sum_{\zeta=0}^{\beta-1} \mathbf{d}_v^{\text{r}}(\zeta+1) \sum_{k=-\infty}^{\infty} \delta(\frac{\omega-\theta}{2\pi} - \frac{k}{\beta}) e^{-j(\omega-\theta)\zeta} \text{d}\omega \right\} \rangle \\
&= \frac{1}{2\pi} \langle \left(\frac{1}{\sqrt{\beta}}\right) \left\{ \sum_{k=-\infty}^{\infty} e^{-j\omega\beta m} \text{rect}\left(\frac{\beta(\omega - \frac{2\pi}{\beta}k)}{2\pi}\right) \sum_{\zeta=0}^{\beta-1} \mathbf{d}_u^{\text{r}}(\zeta+1) e^{-j\frac{2\pi}{\beta}k\zeta} \right\}, \\
&\qquad \left(\frac{1}{\sqrt{\beta}}\right) \left\{ \sum_{k=-\infty}^{\infty} e^{-j\omega\beta n} \text{rect}\left(\frac{\beta(\omega - \frac{2\pi}{\beta}k)}{2\pi}\right) \sum_{\zeta=0}^{\beta-1} \mathbf{d}_v^{\text{r}}(\zeta+1) e^{-j\frac{2\pi}{\beta}k\zeta} \right\} \rangle \\
&= \frac{1}{2\pi} \int_{-\pi}^{\pi} \left(\frac{1}{\sqrt{\beta}}\right) \left\{ \sum_{k=-\lceil\frac{\beta}{2}\rceil}^{\lfloor\frac{\beta}{2}\rfloor} e^{-j\omega\beta m} \text{rect}\left(\frac{\beta(\omega - \frac{2\pi}{\beta}k)}{2\pi}\right) \sum_{\zeta=0}^{\beta-1} \mathbf{d}_u^{\text{r}}(\zeta+1) e^{-j\frac{2\pi}{\beta}k\zeta} \right\} \times \\
&\qquad \left(\frac{1}{\sqrt{\beta}}\right) \left\{ \sum_{k=-\lceil\frac{\beta}{2}\rceil}^{\lfloor\frac{\beta}{2}\rfloor} e^{-j\omega\beta n} \text{rect}\left(\frac{\beta(\omega - \frac{2\pi}{\beta}k)}{2\pi}\right) \sum_{\zeta=0}^{\beta-1} \mathbf{d}_v^{\text{r}}(\zeta+1) e^{-j\frac{2\pi}{\beta}k\zeta} \right\}^* \text{d}\omega \\
&= \left(\frac{1}{2\pi}\right)\left(\frac{1}{\beta}\right) \sum_{k=-\lceil\frac{\beta}{2}\rceil}^{\lfloor\frac{\beta}{2}\rfloor} \left(\sum_{\zeta=0}^{\beta-1} \mathbf{d}_u^{\text{r}}(\zeta+1) e^{-j\frac{2\pi}{\beta}k\zeta}\right) \left(\sum_{\zeta=0}^{\beta-1} \mathbf{d}_v^{\text{r}}(\zeta+1) e^{-j\frac{2\pi}{\beta}k\zeta}\right)^* \int_{\frac{2\pi}{\beta}k-\frac{\pi}{\beta}}^{\frac{2\pi}{\beta}k+\frac{\pi}{\beta}} e^{-j\omega\beta(m-n)} \text{d}\omega \\
&= \left(\frac{1}{2\pi}\right)\left(\frac{1}{\beta}\right) \beta \langle \mathbf{d}_u^{\text{r}}, \mathbf{d}_v^{\text{r}} \rangle \int_{-\frac{\pi}{\beta}}^{\frac{\pi}{\beta}} e^{-j\omega\beta(m-n)} \text{d}\omega \\
&= \left(\frac{1}{2\pi}\right) \langle \mathbf{d}_u^{\text{r}}, \mathbf{d}_v^{\text{r}} \rangle \int_{-\frac{\pi}{\beta}}^{\frac{\pi}{\beta}} e^{-j\omega\beta(m-n)} \text{d}\omega \qquad (3.9)
\end{aligned}$$

where $\mathbf{d}_i^{\text{r}}(\zeta)$ denotes the ζ^{th} entry of $\mathbf{d}_i^{\text{r}}$. Eq. (3.8) follows from the fact that $\mathbf{d}^{(u)}$ is a periodic sequence of period β and is consisted of repetitions of $\mathbf{d}_u^{\text{r}}$.

When $m \neq n$, Eq. (3.9) is evaluated below as,

$$\begin{aligned}\langle \mathbf{f}_m^{(u)}, \mathbf{f}_n^{(v)} \rangle &= \left(\frac{1}{2\pi}\right) \langle \mathbf{d}_u^{\mathrm{r}}, \mathbf{d}_v^{\mathrm{r}} \rangle \int_{-\frac{\pi}{\beta}}^{\frac{\pi}{\beta}} e^{-j\omega\beta(m-n)} \mathrm{d}\omega \\ &= C \left[\frac{e^{-j\omega\beta(m-n)}}{-j\beta(m-n)} \right]_{-\frac{\pi}{\beta}}^{\frac{\pi}{\beta}} \\ &= C \left(\frac{2}{\beta(m-n)} \right) \sin\left((m-n)\,\pi\right) \\ &= 0 \end{aligned} \tag{3.10}$$

where $C = \left(\frac{1}{2\pi}\right) \langle \mathbf{d}_u^{\mathrm{r}}, \mathbf{d}_v^{\mathrm{r}} \rangle$ is a constant, and $\sin((m-n)\pi) = 0$ when $(m-n)$ is an integer.

Case 2: we show that the same row in two different submatrices are orthogonal. That is the m^{th} row in submatrix $\mathbf{F}^{(u)}$ and the m^{th} row in submatrix $\mathbf{F}^{(v)}$, denoted by $\mathbf{f}_m^{(u)}$ and $\mathbf{f}_m^{(v)}$, respectively, $u \neq v$, are orthogonal. Similar to case 1, the inner product of $\mathbf{f}_m^{(u)}$ and $\mathbf{f}_m^{(v)}$ is given by

$$\langle \mathbf{f}_m^{(u)}, \mathbf{f}_m^{(v)} \rangle = \left(\frac{1}{2\pi}\right) \langle \mathbf{d}_u^{\mathrm{r}}, \mathbf{d}_v^{\mathrm{r}} \rangle \int_{-\frac{\pi}{\beta}}^{\frac{\pi}{\beta}} e^{-j\omega\beta(m-m)} \mathrm{d}\omega \tag{3.11}$$

$$= 0 \tag{3.12}$$

where Eq. (3.12) follows from the condition that $\mathbf{D}$ is an unitary matrix and $\langle \mathbf{d}_u^{\mathrm{r}}, \mathbf{d}_v^{\mathrm{r}} \rangle = 0, \forall u \neq v$.

Case 3: the inner product of a row vector with itself is equal to 1. Specifically,

$$\begin{aligned}\langle \mathbf{f}_m^{(u)}, \mathbf{f}_m^{(u)} \rangle &= \left(\frac{1}{2\pi}\right) \langle \mathbf{d}_u^{\mathrm{r}}, \mathbf{d}_u^{\mathrm{r}} \rangle \int_{-\frac{\pi}{\beta}}^{\frac{\pi}{\beta}} e^{-j\omega\beta(m-m)} \mathrm{d}\omega \\ &= \left(\frac{1}{2\pi}\right) \beta \left(\frac{2\pi}{\beta}\right) \\ &= 1 \end{aligned} \tag{3.13}$$

where Eq. (3.13) follows from the condition that $\mathbf{D}$ is a scaled unitary matrix with all of its elements having magnitude 1.

In converse, if $\mathbf{D}$ is not an unitary matrix, which means $\exists\ u^*$ and v^* such that $\mathbf{d}_{u^*}^{\mathrm{r}}$ and $\mathbf{d}_{v^*}^{\mathrm{r}}$ are not orthogonal, it then follows from Eq. (3.11) that the corresponding rows $\mathbf{f}_m^{(u^*)}$ and $\mathbf{f}_m^{(v^*)}$ are not

orthogonal. Hence, $\tilde{\mathbf{F}}$ is an unitary matrix iff $\mathbf{D}$ is a scaled unitary matrix.

□

Through Lemma 2, we have established that $\tilde{\mathbf{F}}$ is a unitary matrix when $M = \beta$. With the information codeword $\mathbf{x}$ being an i.i.d. Gaussian sequence, it follows from the property of unitary transformation that $\tilde{\mathbf{x}}$ is also an i.i.d. Gaussian sequence with the same power as $\mathbf{x}$. On the other hand, $\tilde{\mathbf{x}}$ can be represented as the concatenation of M redundancy blocks, $\{\tilde{\mathbf{x}}^{(1)}, \tilde{\mathbf{x}}^{(2)}, \ldots, \tilde{\mathbf{x}}^{(M)}\}$ such that $\tilde{\mathbf{x}}^{(i)}$ is independent of $\tilde{\mathbf{x}}^{(j)}$, $\forall i \neq j$. These independent redundancy blocks are then transmitted subsequently at different time slots. Therefore, the received redundancy blocks $\{\mathbf{y}^{(1)}, \mathbf{y}^{(2)}, \ldots, \mathbf{y}^{(M)}\}$ are also mutually independent.

3.3 Proof of Optimality for $M \leq \beta$

Our goal is to design a scheme such that the optimal communication rate can be achieved when the channel is unknown to the transmitter and is time-invariant during the transmission of each redundancy block, but can vary over different blocks. The optimal total mutual information between the transmitted signal and the received signal expands linearly with time. As a result, our interest is to maximize the mutual information between the combined received blocks and the original codeword $\mathbf{x}$, $\forall M$. Recall that the redundancy blocks $\{\tilde{\mathbf{x}}^{(1)}, \tilde{\mathbf{x}}^{(2)}, \ldots, \tilde{\mathbf{x}}^{(M)}\}$ are independent, Gaussian, and each being capacity-achieving, we next show that the mutual information between the received redundancy blocks and $\mathbf{x}$ increases linearly with M, $\forall M \leq \beta$, which means the combined redundancy blocks are also capacity-achieving when jointly decoded.

Theorem 3.1. With a time-invariant channel, let $S = \{\mathbf{y}^{(1)}, \mathbf{y}^{(2)}, \ldots, \mathbf{y}^{(M)}\}$ denote the set of M received redundancy blocks, $M \leq \beta$. Let S' denote a subset of S that it contains M' vectors in S. The mutual information between S' and the information codeword $\mathbf{x}$ is proportional to the number of vectors in S', iff $\tilde{\mathbf{F}}$ is an unitary matrix. In other words, $I(S'; \mathbf{x}) = M' \times I(\mathbf{y}^{(1)}; \mathbf{x})$, iff $\tilde{\mathbf{F}}$ is a unitary matrix.

Proof. Without loss of generality, we assume that the M' vectors in S' are the first M' vectors $\{\mathbf{y}^{(1)}, \mathbf{y}^{(2)}, \ldots, \mathbf{y}^{(M')}\}$. The statement can be shown through induction.

Base Step:

$$\begin{aligned} I(\mathbf{y}^{(1)}, \mathbf{y}^{(2)}; \mathbf{x}) &= I(\mathbf{y}^{(1)}; \mathbf{x}) + I(\mathbf{y}^{(2)}; \mathbf{x}|\mathbf{y}^{(1)}) \\ &= I(\mathbf{y}^{(1)}; \mathbf{x}) + I(\mathbf{y}^{(2)}; \mathbf{x}) - I(\mathbf{y}^{(1)}; \mathbf{y}^{(2)}) \quad (3.14) \\ &= I(\mathbf{y}^{(1)}; \mathbf{x}) + I(\mathbf{y}^{(2)}; \mathbf{x}) \quad (3.15) \\ &= 2I(\mathbf{y}^{(1)}; \mathbf{x}) \end{aligned}$$

where Eq. (3.14) follows from Eq. (3.16)

$$\begin{aligned} I(\mathbf{y}^{(2)}; \mathbf{x}|\mathbf{y}^{(1)}) &= H(\mathbf{y}^{(2)}|\mathbf{y}^{(1)}) - H(\mathbf{y}^{(2)}|\mathbf{y}^{(1)}, \mathbf{x}) \\ &= H(\mathbf{y}^{(2)}|\mathbf{y}^{(1)}) - H(\mathbf{y}^{(2)}|\mathbf{x}) \\ &= H(\mathbf{y}^{(2)}) + H(\mathbf{y}^{(1)}|\mathbf{y}^{(2)}) - H(\mathbf{y}^{(1)}) - H(\mathbf{y}^{(2)}|\mathbf{x}) \\ &= I(\mathbf{y}^{(2)}; \mathbf{x}) - I(\mathbf{y}^{(1)}; \mathbf{y}^{(2)}) \quad (3.16) \end{aligned}$$

and Eq. (3.15) relies on the conclusion that the received redundancy blocks $\{\mathbf{y}^{(1)}, \mathbf{y}^{(2)}, \ldots, \mathbf{y}^{(M)}\}$ are mutually independent.

Inductive Assumption:

$$I(\mathbf{y}^{(1)}, \mathbf{y}^{(2)}, \ldots, \mathbf{y}^{(n-1)}; \mathbf{x}) = (n-1)I(\mathbf{y}^{(1)}; \mathbf{x}) \quad (3.17)$$

Inductive Step:

$$I(\mathbf{y}^{(1)}, \mathbf{y}^{(2)}, \ldots, \mathbf{y}^{(n)}; \mathbf{x}) = I(\mathbf{y}^{(1)}, \mathbf{y}^{(2)}, \ldots, \mathbf{y}^{(n-1)}; \mathbf{x}) + I(\mathbf{y}^{(n)}; \mathbf{x}|\mathbf{y}^{(1)}, \mathbf{y}^{(2)}, \ldots, \mathbf{y}^{(n-1)}) \quad (3.18)$$

where,

$$I(\mathbf{y}^{(1)}, \mathbf{y}^{(2)}, \ldots, \mathbf{y}^{(n-1)}; \mathbf{x}) = (n-1)I(\mathbf{y}^{(1)}; \mathbf{x}) \quad (3.19)$$

follows from the inductive assumption shown by Eq. (3.17), and

$$\begin{aligned} I(\mathbf{y}^{(n)};\mathbf{x}|\mathbf{y}^{(1)},\mathbf{y}^{(2)},\ldots,\mathbf{y}^{(n-1)}) &= H(\mathbf{y}^{(n)}|\mathbf{y}^{(1)},\mathbf{y}^{(2)},\ldots,\mathbf{y}^{(n-1)}) - H(\mathbf{y}^{(n)}|\mathbf{y}^{(1)},\mathbf{y}^{(2)},\ldots,\mathbf{y}^{(n-1)},\mathbf{x}) \\ &= H(\mathbf{y}^{(n)}|\mathbf{y}^{(1)},\mathbf{y}^{(2)},\ldots,\mathbf{y}^{(n-1)}) - H(\mathbf{y}^{(n)}|\mathbf{x}) \qquad (3.20) \\ &= H(\mathbf{y}^{(n)}|\mathbf{y}^{(1)},\mathbf{y}^{(2)},\ldots,\mathbf{y}^{(n)}) - H(\mathbf{y}^{(n)}|\mathbf{y}^{(1)},\mathbf{y}^{(2)},\ldots,\mathbf{y}^{(n-1)}) - H(\mathbf{y}^{(n)}|\mathbf{x}) \\ &= [H(\mathbf{y}^{(n)}) - H(\mathbf{y}^{(n)}|\mathbf{x})] \\ &\qquad - [H(\mathbf{y}^{(1)},\mathbf{y}^{(2)},\ldots,\mathbf{y}^{(n-1)}) - H(\mathbf{y}^{(n)}|\mathbf{y}^{(1)},\mathbf{y}^{(2)},\ldots,\mathbf{y}^{(n-1)})] \\ &= I(\mathbf{y}^{(n)};x) - I(\mathbf{y}^{(1)},\mathbf{y}^{(2)},\ldots,\mathbf{y}^{(n-1)};\mathbf{y}^{(n)}) \\ &= I(\mathbf{y}^{(1)};\mathbf{x}) \qquad (3.21) \end{aligned}$$

Eq. (3.21) holds because the received redundancy blocks $\{\mathbf{y}^{(1)},\mathbf{y}^{(2)},\ldots,\mathbf{y}^{(M)}\}$ are mutually independent. Now, substitute Eqs. (3.19) and (3.21) into Eq. (3.18), we have shown that the inductive assumption Eq. (3.17) holds also for n such that

$$I(\mathbf{y}^{(1)},\mathbf{y}^{(2)},\ldots,\mathbf{y}^{(n)};\mathbf{x}) = nI(\mathbf{y}^{(1)};\mathbf{x}). \qquad (3.22)$$

□

Although Theorem 3.1 imposes the assumption that the channel is time-invariant, by following the same reasoning, the total mutual information expression (Eq. (3.22)) can easily be generalized for the case that the channel is time-varying throughout the transmission of the M redundancy blocks. The cumulative mutual information, denoted by I_M, is equal to the sum of mutual information between $\mathbf{x}$ and each individual redundancy block. Specifically,

$$I_M \triangleq I(\mathbf{y}^{(1)},\mathbf{y}^{(2)},\ldots,\mathbf{y}^{(M)};\mathbf{x}) = \sum_{i=1}^{M} I(\mathbf{y}^{(i)};\mathbf{x}) \qquad (3.23)$$

The implication of this result is as follows: suppose the information message is coded with a capacity-achieving code at base code-rate R_b. When the channel condition is poor, the decoder keeps on collecting redundancy blocks until the cumulative mutual information, I_M, exceeds R_b such that the original message can be recovered. On the other hand, when the channel condition is good, such that $I(\mathbf{y}^{(i)};\mathbf{x})$ is relatively large, the decoder requires fewer number of redundancy blocks, M, for decoding. To fully illustrate the benefit of the SNQ scheme, let us consider the special case when the SNQ signaling rate β approaches infinity, which results in an infinite number

of minute redundancy blocks each carrying a little bit information about the same codeword $\mathbf{x}$. Hence, the decoder will then always be able to cumulate just enough redundancy blocks such that $I_M = R_\mathrm{b}$. In addition, the mutual information I_M is capacity achieving, $\forall M$ (i.e. $I_M = C_M$) as $M \leq \beta$. In this case, the dithered SNQ repetition coding scheme always achieves channel capacity for any time-varying ISI channel.

3.4 Overall Performance of the Dithered SNQ Repetition Scheme

The conclusion drawn in Theorem 3.1 can also be seen from another perspective. For simplicity, let us assume the channel is a perfect band-limited channel, which implies that $\mathbf{H}$ is an identity matrix in Eq. (3.2). Under this condition, the discrete model simplifies to $\mathbf{y} = \tilde{\mathbf{F}}\mathbf{x} + \mathbf{n}$. With SNQ signaling rate β and number of redundancy blocks M, $\tilde{\mathbf{F}}$ is a matrix of size $M\frac{L_\mathrm{x}}{\beta} \times L_\mathrm{x}$ and the discrete model defines a virtual MIMO AWGN channel with L_x inputs and $M\frac{L_\mathrm{x}}{\beta}$ outputs. When $M \leq \beta$, the number of outputs is less than or equal to the number of inputs and the capacity of the channel can be achieved iff the rows of $\tilde{\mathbf{F}}$ are orthogonal. When $M > \beta$, the number of outputs is greater than the number of inputs and there is necessarily a loss between the cumulative mutual information, I_M, and the AWGN channel capacity because not all $M\frac{L_\mathrm{x}}{\beta}$ degrees of freedom can be filled.

Lemma 3. The optimal achievable rate for this MIMO scheme is given by,

$$R_\mathrm{opt} = \begin{cases} M\log(1+\frac{E}{N}) & \text{for } M \leq \beta \\ \beta\log(1+\frac{M}{\beta}\frac{E}{N}) & \text{for } M > \beta, \end{cases} \tag{3.24}$$

Proof. The first part of Eq. (3.24) corresponds to Theorem 3.1 under the special case that the channel is a time-invariant AWGN channel. Let us then focus on the case when $M > \beta$. In particular, let $\{\lambda_1, \lambda_2, \ldots, \lambda_{L_\mathrm{x}}\}$ denote the eigenvalues of $\tilde{\mathbf{F}}$, whose size is $\frac{M}{\beta}L_\mathrm{x} \times L_\mathrm{x}$, $M > \beta$ and has rank L_x to achieve optimality [15]. Because both $\mathbf{x}$ and $\tilde{\mathbf{x}}$ are i.i.d. Gaussian vectors with constant power, the rows and columns of $\tilde{\mathbf{F}}$ are constraint to have norm 1 and $\frac{M}{\beta}$, respectively. The capacity of this

MIMO channel is given by,

$$\begin{aligned} C &= \left(\frac{\beta}{L_x}\right) \log_2 \det\left(\mathbf{I} + \tilde{\mathbf{F}}^H \tilde{\mathbf{F}} \frac{E}{N}\right) \\ &= \left(\frac{\beta}{L_x}\right) \sum_{i=1}^{L_x} \log_2\left(1 + \lambda_i^2 \frac{E}{N}\right) \qquad \text{[bits/channel use]} \end{aligned} \tag{3.25}$$

in which C is maximized when all the eigenvalues are equal [15]. Performing single-value-decomposition on $\tilde{\mathbf{F}}$ such that $\tilde{\mathbf{F}} \triangleq \mathbf{U}\Lambda\mathbf{V}$. Then, we have

$$\begin{aligned} \tilde{\mathbf{F}}^H \tilde{\mathbf{F}} &= \left(\mathbf{V}^H \Lambda^H \mathbf{U}^H\right)(\mathbf{U}\Lambda\mathbf{V}) \\ &= \mathbf{V}^H \Lambda \mathbf{V} \\ &= \mathbf{V}^H \begin{bmatrix} \lambda_1^2 & 0 & \dots & 0 \\ 0 & \lambda_2^2 & \dots & 0 \\ 0 & 0 & \ddots & 0 \\ 0 & 0 & \dots & \lambda_{L_x}^2 \end{bmatrix} \mathbf{V} \qquad (3.26) \\ &= (\frac{M}{\beta})\mathbf{I} \qquad (3.27) \end{aligned}$$

From Eq. (3.26) and Eq. (3.27), we can see that the columns of $\tilde{\mathbf{F}}$ must be orthogonal in order to have the eigenvalues λ_i, $i \in \{1, 2, \dots, \lambda_{L_x}\}$ to be equivalent. With the power constraint, all the eigenvalues are equal to $\sqrt{\frac{M}{\beta}}$. The transmitting signal has total power constraint E and N is the AWGN power. Now substitute Eq. (3.27) into Eq. (3.25), we have

$$\begin{aligned} C &= \left(\frac{\beta}{L_x}\right) \sum_{i=1}^{L_x} \log_2\left(1 + \lambda_i^2 \frac{E}{N}\right) \\ &= \left(\frac{\beta}{L_x}\right) L_x \log_2\left(1 + \frac{M}{\beta}\frac{E}{N}\right) \\ &= \beta \log_2\left(1 + \frac{M}{\beta}\frac{E}{N}\right) \end{aligned} \tag{3.28}$$

When the L_x columns of $\tilde{\mathbf{F}}$ are orthogonal, the total power of the transmitted signal is equally divided among the L_x subspaces and the optimal rate, given by Eq. (3.28) can be achieved. □

We next show that, when M is an integer multiple of β and $M > \beta$, the columns of $\tilde{\mathbf{F}}$ are orthogonal.

Lemma 4. Let $\mathbf{D}$ be an unitary matrix and $M > \beta$. The columns of $\tilde{\mathbf{F}}$ are orthogonal iff M is an integer multiple of β (i.e. (M mod β)=0).

Proof. Let $\tilde{\mathbf{f}}_m$, $\tilde{\mathbf{f}}_m^{(i)}$, $\mathbf{f}_m$ and $\mathbf{d}_m$ denote the m^{th} column of $\tilde{\mathbf{F}}$, $\mathbf{F}^{(i)}$, $\mathbf{F}$ and $\mathbf{D}$, respectively. Let $\mathbf{d}^{(i)}(m)$ denote the m^{th} element of $\mathbf{d}^{(i)}$.

$$\begin{aligned}
\langle \tilde{\mathbf{f}}_m, \tilde{\mathbf{f}}_n \rangle &= \tilde{\mathbf{f}}_m^H \tilde{\mathbf{f}}_n \\
&= \sum_{i=1}^{M} (\tilde{\mathbf{f}}_m^{(i)})^H \tilde{\mathbf{f}}_n^{(i)} \\
&= \sum_{i=1}^{M} \mathbf{d}^{(i)^H}(m) \mathbf{f}_m^H \mathbf{d}^{(i)}(n) \mathbf{f}_n \\
&= \mathbf{f}_m^H \mathbf{f}_n \sum_{i=1}^{M} \mathbf{d}^{(i)^H}(m) \mathbf{d}^{(i)}(n) \\
&= \langle \mathbf{d}_{m'}^c, \mathbf{d}_{n'}^c \rangle \langle \mathbf{f}_m, \mathbf{f}_n \rangle
\end{aligned} \tag{3.29}$$

where $m' \triangleq (m \bmod M)$ and $n' \triangleq (n \bmod M)$.

We first prove the direct statement: when M is an integer multiple of β, the columns of $\tilde{\mathbf{F}}$ are orthogonal. We divide the proof into two cases.
Case 1: when $(n - m)$ is an integer multiple of β, it follows from Lemma 1 that the inner product between $\tilde{\mathbf{f}}_m$ and $\tilde{\mathbf{f}}_n$ is given by,

$$\begin{aligned}
\langle \tilde{\mathbf{f}}_m, \tilde{\mathbf{f}}_n \rangle &= \langle \mathbf{d}_{m'}^c, \mathbf{d}_{n'}^c \rangle \langle \mathbf{f}_m, \mathbf{f}_n \rangle \\
&= \langle \mathbf{d}_{m'}^c, \mathbf{d}_{n'}^c \rangle 0 \\
&= 0
\end{aligned} \tag{3.30}$$

Case 2: when $(n - m)$ is not an integer multiple of β, $((n - m) \bmod \beta) \neq 0$. Since M is an integer multiple of β, $((n - m) \bmod M) \neq 0$. Hence, $m' \neq n'$. Given that $\mathbf{D}$ is an unitary matrix, Eq. (3.29)

is equal to:

$$\begin{aligned}\langle \tilde{\mathbf{f}}_m, \tilde{\mathbf{f}}_n \rangle &= \langle \mathbf{d}^{\mathrm{c}}_{m'}, \mathbf{d}^{\mathrm{c}}_{n'} \rangle \langle \mathbf{f}_m, \mathbf{f}_n \rangle \\ &= 0 \langle \mathbf{f}_m, \mathbf{f}_n \rangle \\ &= 0 \end{aligned} \tag{3.31}$$

The converse states: if M is not an integer multiple of β, then not all columns of $\tilde{\mathbf{F}}$ are orthogonal. It can be shown as follows: let $n = m + M$. We have $n' = m'$ and $((n-m) \bmod \beta) = (M \bmod \beta) \neq 0$. Therefore,

$$\begin{aligned}\langle \tilde{\mathbf{f}}_m, \tilde{\mathbf{f}}_n \rangle &= \langle \mathbf{d}^{\mathrm{c}}_{n'}, \mathbf{d}^{\mathrm{c}}_{m'} \rangle \langle \mathbf{f}_m, \mathbf{f}_n \rangle \\ &= M \langle \mathbf{f}_m, \mathbf{f}_n \rangle \\ &\neq 0 \end{aligned} \tag{3.32}$$

where Eq. (3.32) follows from Lemma 1.

□

Combining Lemma 4 and the conclusion from Lemma 3 that optimal rate can be achieved when columns of $\tilde{\mathbf{F}}$ are orthogonal, we can conclude that R_{opt} in Eq. (3.24) can be met with the proposed scheme for the $M > \beta$ case when (M mod β)=0. Note that Eq. (3.24) is also equal to the bound for the layered repetition coding scheme introduced in [5]. So what is the achievable rate for $M > \beta$ and (M mod β)$\neq$ 0?

Proposition 1. The achievable rate of the dithered SNQ repetition coding scheme for all M values is given by,

$$R = \begin{cases} M \log(1 + \frac{E}{N}) & \text{for } \; M \leq \beta \\ k^{-} \log(1 + \lfloor \frac{M}{\beta} \rfloor \frac{E}{N}) + k^{+} \log(1 + \lceil \frac{M}{\beta} \rceil \frac{E}{N}) & \text{for } \; M > \beta \end{cases} \tag{3.33}$$

where

$$\begin{cases} k^+ = M - \lfloor \frac{M}{\beta} \rfloor \beta \\ k^- = \beta - k^+ \end{cases}$$

We verify Eq. (3.33) through a simple example, where the dithering matrix, $\mathbf{D}$, is a scaled and rearranged $M \times M$ DFT matrix; the SNQ signaling rate β is equal to 2; and the number of redundancy blocks, M, is equal to 4. This example can be easily extended to the general case for other β and M values.

Our goal is to calculate the achievable rate when an increasing number of redundancy blocks are combined. First, note that the dithering matrix $\mathbf{D}$ is chosen to be,

$$\mathbf{D} = \begin{bmatrix} 1 & 1 & 1 & 1 \\ 1 & -1 & 1 & -1 \\ 1 & -j & -1 & j \\ 1 & j & -1 & -j \end{bmatrix}. \tag{3.34}$$

Assume we have a time-invariant AWGN channel with noise power N, we calculate the achievable rate with the capacity integration formula for AWGN channel, given by

$$R = \int_{-\infty}^{\infty} \log_2(1 + \frac{S_{\tilde{\mathbf{x}}}(f)}{N}) \mathrm{d}f., \tag{3.35}$$

where $S_{\tilde{\mathbf{x}}}(f)$ is the power-spectral-density (PSD) of the modulated signal $\tilde{\mathbf{x}}$.

Without loss of generality, we use the second redundancy block in our example. Figure 3-1 depicts the PSD of the signal at each step of the modulation procedure for the second redundancy block. Part (1) of the figure corresponds to the PSD of the information codeword $\mathbf{x}$. The frequency spectrum is divided into 4 sections, each occupying an equal bandwidth, as labeled in the figure. The second redundancy block is dithered with the 2^{nd} row of $\mathbf{D}$. Hence, as shown in part (2) of the figure, the dithered signal, $\mathbf{x}^{(2)}$, is a frequency-shifted version of $\mathbf{x}$, whose spectrum is shifted by π. Let f_{n} denote the Nyquist sampling rate, f_{s} denote the SNQ sampling rate where $f_{\text{s}} = \beta f_{\text{n}}$ and E denote the power constraint of the transmission signal. Part (3) shows the dithered signal

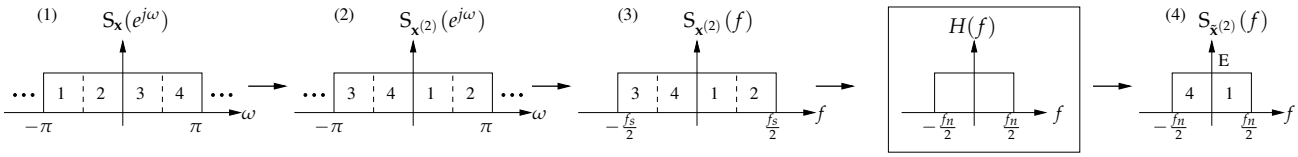

Figure 3-1: PSD of the signal modulation procedure at each stage for the 2nd redundancy block.

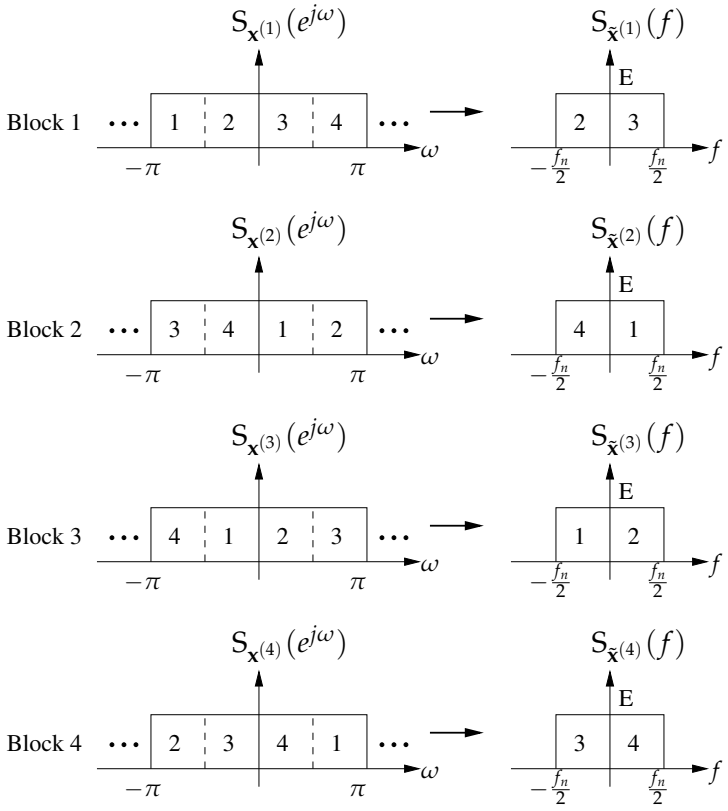

Figure 3-2: PSD of dithered and modulated blocks when $\beta = 2$ and $M = 4$.

sequence sampled at f_s and part (4) shows the modulated signal, whose bandwidth is limited to the Nyquist bandwidth of the channel.

The modulation processes for all four redundancy blocks are similar and Figure 3-2 contains the PSD of the dithered data sequence and the modulated signal for all the blocks.

At the receiver end, the four redundancy blocks are cumulated subsequently in time. Figure 3-3 shows the joint PSD for the cases when 1, 2, 3 and 4 blocks are combined, respectively. Next to the PSD diagram in Figure 3-3, the corresponding achievable rates are computed via. Eq. (3.35), indicating the bounds in Eq. (3.33) is met.

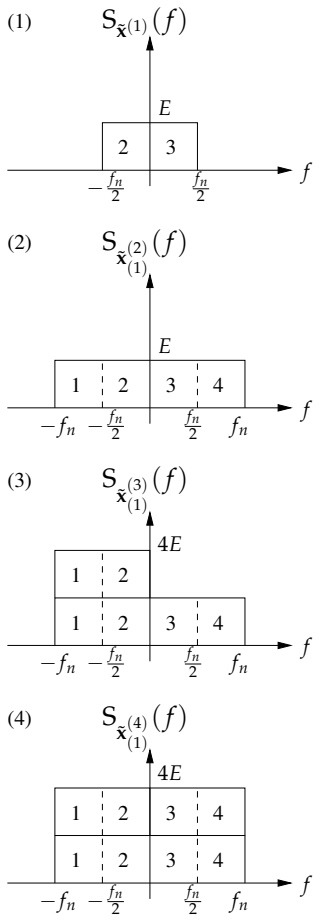

$$R_{\tilde{\mathbf{x}}^{(1)}} = \int_{-\frac{f_n}{2}}^{\frac{f_n}{2}} \log_2(1+\frac{E}{N})\mathrm{d}f = f_n \log_2(1+\tfrac{E}{N})$$

$$R_{\tilde{\mathbf{x}}^{(2)}_{(1)}} = \int_{-f_n}^{f_n} \log_2(1+\frac{E}{N})\mathrm{d}f = 2f_n \log_2(1+\tfrac{E}{N})$$

$$R_{\tilde{\mathbf{x}}^{(3)}_{(1)}} = \int_{-f_n}^{0} \log_2(1+\frac{4E}{2N})\mathrm{d}f + \int_{0}^{f_n} \log_2(1+\frac{E}{N})\mathrm{d}f = f_n \log_2(1+2\tfrac{E}{N}) + f_n \log_2(1+\tfrac{E}{N})$$

$$R_{\tilde{\mathbf{x}}^{(4)}_{(1)}} = \int_{-f_n}^{f_n} \log_2(1+\frac{4E}{2N})\mathrm{d}f = 2f_n \log_2(1+2\tfrac{E}{N})$$

Figure 3-3: Accumulative achievable rate through combining multiple number of redundancy blocks.

In fact, not only is Eq. (3.33) achievable, but it is also the optimal achievable rate for the dithered SNQ signaling scheme. The reasoning is as follows: in order to achieve optimal rate, the PSD of the combined blocks should be as flat as possible. With SNQ signaling at β times the Nyquist rate and jointly decoding multiple redundancy blocks, the combined signal will occupy the frequency range $[-\beta\frac{f_n}{2}, \beta\frac{f_n}{2}]$ at its utmost. When the number of redundancy blocks exceed β, i.e. $M > \beta$, the bound in Eq. (3.24) can be achieved only when the power of the combined signal is evenly distributed over the entire frequency band, $[-\beta\frac{f_n}{2}, \beta\frac{f_n}{2}]$. However, due to the bandwidth limit of the channel, each redundancy block will only be able to occupy a frequency band with bandwidth equal to f_n. As a result, with each additional redundancy block, a block with bandwidth $[-\frac{f_n}{2}, \frac{f_n}{2}]$ will be stacked onto the PSD diagram, more or less like the process demonstrated by Part (2) and

Part (3) of Figure 3-3. With the assistance of the integration formula Eq. (3.35), we can see that the achievable rate for any M and β is given by Eq. (3.33).

Figure 3-4 plots the effective spectral efficiency curves (computed from Eq. (3.33)) for different SNQ-signaling rates, when the target information rate we are trying to obtain by combining multiple number of redundancy blocks is equal to 8 [bits/s/Hz]. The effective spectral efficiency is given by,

$$\text{effective spectral efficiency} = \frac{\text{target rate}}{\text{minimum \# of redundancy blocks required for decoding}}. \quad (3.36)$$

Hence, as SNR increases, the number of redundancy blocks required to achieve target rate decreases, which means the effective spectral frequency also increases. Eq. (3.33) indicates that the DFT scheme performance curve touches the channel capacity when M is less than or equal to the signaling β and is strictly below capacity for M less than β. Figure 3-4 demonstrates that as β increases, this gap between capacity and the DFT achievable rate diminishes. Hence, with high signaling rate, the DFT SNQ scheme is almost capacity achieving with any M.

3.5 The Virtual AWGN Intermediate Channel Seen by the Code

In Section 3.3, we have shown that the DFT dithered SNQ signaling scheme is capacity-achieving in the information theoretic perspective when a capacity-achieving code is used. Most capacity-achieving codes are designed for AWGN channels whose channel SNR is time-invariant. Unfortunately, even when the channel SNR is time-invariant, the channel ISI coupled with the dithering effect may yield time-varying symbol SNR at the slicer. In this section, we show that, assuming perfect feedback, the MMSE-DFE yields constant symbol SNR at the slicer. In other words, referring to Figure 1-1, we show that when looking at the codewords to the signal modulator as input and taking the slicer-inputs, $\hat{x}_s$, as output, the intermediate communication system taken together behaves as an AWGN channel with constant SNR.

The channel model coupled with the dithering operation is rewritten as follows:

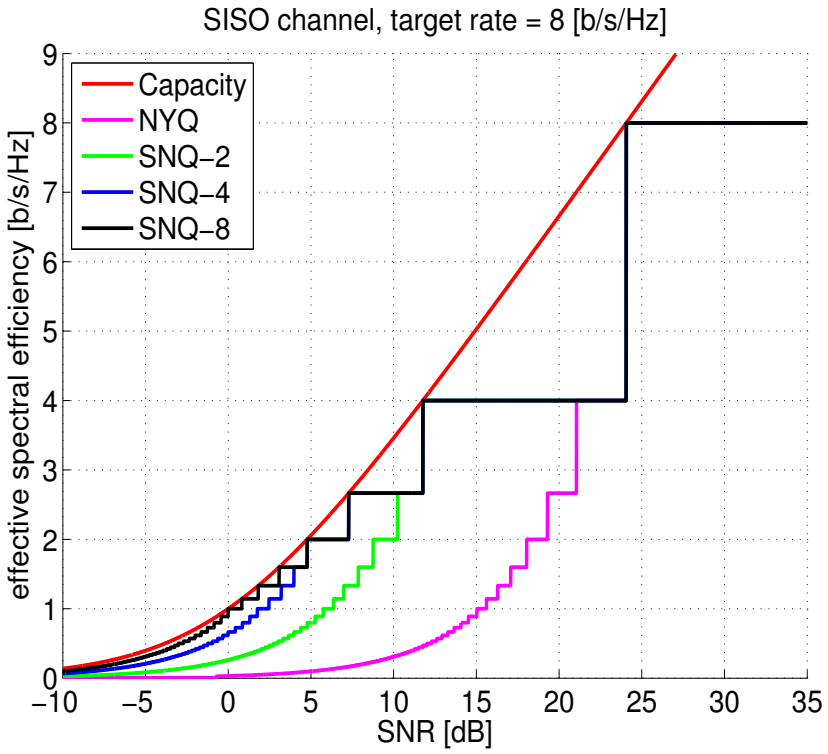

Figure 3-4: Theoretical achievable rates of the Nyquist and SNQ schemes

$$\mathbf{y}[k] = \begin{bmatrix} \mathbf{y}^{(1)}[k] \\ \mathbf{y}^{(2)}[k] \\ \vdots \\ \mathbf{y}^{(M)}[k] \end{bmatrix} = \begin{bmatrix} \mathbf{G}^{(1)}[k] \circ \mathbf{D}^{(1)}[k] \\ \mathbf{G}^{(2)}[k] \circ \mathbf{D}^{(2)}[k] \\ \vdots \\ \mathbf{G}^{(M)}[k] \circ \mathbf{D}^{(M)}[k] \end{bmatrix} \mathbf{x}[k] + \begin{bmatrix} \mathbf{n}^{(1)}[k] \\ \mathbf{n}^{(2)}[k] \\ \vdots \\ \mathbf{n}^{(M)}[k] \end{bmatrix} \tag{3.37}$$

$$= \begin{bmatrix} \mathbf{G}^{(1)^\dagger}[k] \\ \mathbf{G}^{(2)^\dagger}[k] \\ \vdots \\ \mathbf{G}^{(M)^\dagger}[k] \end{bmatrix} \mathbf{x}[k] + \begin{bmatrix} \mathbf{n}^{(1)}[k] \\ \mathbf{n}^{(2)}[k] \\ \vdots \\ \mathbf{n}^{(M)}[k] \end{bmatrix} \tag{3.38}$$

where $\mathbf{G}^{(i)^\dagger}[k]$ can be decomposed into three parts as shown in Eq (2.24). More specifically,

$$\mathbf{G}^{(i)^\dagger}[k] \triangleq \begin{bmatrix} \mathbf{G}^{(i)^\dagger}_{\text{fb}}[k] & \mathbf{g}^{(i)^\dagger}_{0}[k] & \mathbf{G}^{(i)^\dagger}_{0}[k] \end{bmatrix}. \tag{3.39}$$

The received signal $\mathbf{y}[k]$ is then processed with a MMSE-DFE with feedforward filter length L_{ff} and feedback filter length L_{fb}. Let

$$\mathbf{x}_{\text{fb}}[k] \triangleq [x[k-L_{\text{fb}}], \ldots, x[k-1]]^{\text{T}} \tag{3.40}$$

denote the feedback vector of previous symbols, and let

$$\mathbf{y}_{\text{ff}}^{(i)}[k] \triangleq \left[y^{(i)}[k], \ldots, y^{(i)}[k+L_{\text{ff}}-1]\right]^{\text{T}} \qquad i \in \{1,2,\ldots,M\} \tag{3.41}$$

denote the feedforward portion from the i^{th} received block $y^{(i)}$.

The linear-minimum-mean-square-error (LMMSE) estimate of the zero-mean random variable $x[k]$ is given by,

$$\hat{x}[k] \triangleq \mathbb{E}[x[k] \mid \mathbf{x}_{\text{fb}}[k], \mathbf{y}_{\text{ff}}^{(1)}[k], \ldots, \mathbf{y}_{\text{ff}}^{(M)}[k]] \tag{3.42}$$

$$\triangleq \begin{bmatrix} \mathbf{h}_{\text{fb}}[k] \\ \mathbf{h}_{\text{ff}}^{(1)}[k] \\ \vdots \\ \mathbf{h}_{\text{ff}}^{(M)}[k] \end{bmatrix}^{\text{H}} \begin{bmatrix} \mathbf{x}_{\text{fb}}[k] \\ \mathbf{y}_{\text{ff}}^{(1)}[k] \\ \vdots \\ \mathbf{y}_{\text{ff}}^{(M)}[k] \end{bmatrix} \tag{3.43}$$

$$\triangleq \mathbf{h}[k]^{\text{H}}\mathbf{v}[k] \tag{3.44}$$

where the vector $\mathbf{v}[k]$ is a concatenation of the past feedback vector $\mathbf{x}_{\text{fb}}[k]$ and the feedforward vectors $\mathbf{y}_{\text{ff}}^{(i)}[k]$.

Let l denote the total length of the estimation vector $\mathbf{v}[k]$, thus $l = L_{\text{fb}} + ML_{\text{ff}}$. Define the co-

variance between the symbol estimate and $\mathbf{v}$ as a row vector:

$$\begin{aligned}
\mathbf{k}_{x\mathbf{v}}[k] &\triangleq \mathbb{E}\left[x[k]v^*[1],\ \ldots,\ x[k]v^*[l]\right] \\
&= \mathbb{E}\left[x[k]\mathbf{x}_{\text{fb}}^{\text{H}}[k],\ x[k]\mathbf{y}_{\text{ff}}^{(1)^{\text{H}}}[k],\ \ldots,\ x[k]\mathbf{y}_{\text{ff}}^{(M)^{\text{H}}}[k]\right] \\
&= [0, 0, \ldots, 0, \mathbf{g}_0^{(1)^{\dagger^{\text{H}}}}[k], \mathbf{g}_0^{(2)^{\dagger^{\text{H}}}}[k], \ldots, \mathbf{g}_0^{(M)^{\dagger^{\text{H}}}}[k]] \\
&= \left[\,\mathbf{0}\,\middle|\,\mathbf{g}_0{}^{\dagger^{\text{H}}}[k]\,\right] \qquad (3.45)
\end{aligned}$$

Let $\mathbf{I}_x \triangleq \sigma_x^2\mathbf{I}$ and let $\mathbf{I}_n \triangleq \sigma_n^2\mathbf{I}$. Then, the covariance matrix of $\mathbf{v}[k]$ is given by,

$$\begin{aligned}
\mathbf{K}_{\mathbf{vv}}[k] &= \mathbb{E}\left[\mathbf{v}[k]\mathbf{v}^{\text{H}}[k]\right] \\
&= \mathbb{E}\left[\begin{bmatrix}\mathbf{x}_{\text{fb}} \\ \mathbf{y}_{\text{ff}}^{(1)} \\ \mathbf{y}_{\text{ff}}^{(2)} \\ \vdots \\ \mathbf{y}_{\text{ff}}^{(M)}\end{bmatrix}\left[\mathbf{x}_{\text{fb}}{}^{\text{H}}, \mathbf{y}_{\text{ff}}^{(1)^{\text{H}}}, \mathbf{y}_{\text{ff}}^{(2)^{\text{H}}}, \ldots, \mathbf{y}_{\text{ff}}^{(M)^{\text{H}}}\right]\right] \\
&= \left[\begin{array}{c|ccc}
\mathbf{I}_x & \left[\mathbf{G}_0^{(1)^{\dagger^{\text{H}}}}[k]\right] & \cdots & \left[\mathbf{G}_0^{(M)^{\dagger^{\text{H}}}}[k]\right] \\
\hline
\left[\mathbf{G}_0^{(1)^{\dagger}}[k]\right] & \mathbf{I}_n + \left[\mathbf{G}_0^{(1)^{\dagger}}[k]\right]\left[\mathbf{G}_0^{(1)^{\dagger^{\text{H}}}}[k]\right] & \cdots & \left[\mathbf{G}_0^{(1)^{\dagger}}[k]\right]\left[\mathbf{G}_0^{(M)^{\dagger^{\text{H}}}}[k]\right] \\
\vdots & \vdots & \ddots & \vdots \\
\left[\mathbf{G}_0^{(M)^{\dagger}}[k]\right] & \left[\mathbf{G}_0^{(M)^{\dagger}}[k]\right]\left[\mathbf{G}_0^{(1)^{\dagger^{\text{H}}}}[k]\right] & \cdots & \mathbf{I}_n + \left[\mathbf{G}_0^{(M)^{\dagger}}[k]\right]\left[\mathbf{G}_0^{(M)^{\dagger^{\text{H}}}}[k]\right]
\end{array}\right] \\
&= \left[\begin{array}{c|c}
\mathbf{I}_x & \mathbf{G}_0{}^{\dagger^{\text{H}}}[k] \\
\hline
\mathbf{G}_0{}^{\dagger}[k] & \mathbf{I}_n + \left[\mathbf{G}_0{}^{\dagger}[k]\right]\left[\mathbf{G}_0{}^{\dagger^{\text{H}}}[k]\right]
\end{array}\right]. \qquad (3.46)
\end{aligned}$$

Let us define the inverse of $\mathbf{K}_{\mathbf{vv}}[k]$ as follows:

$$\left[\mathbf{K}_{\mathbf{vv}}[k]\right]^{-1} \triangleq \left[\begin{array}{c|c}\mathbf{A}[k] & \mathbf{B}[k] \\ \hline \mathbf{C}[k] & \mathbf{D}[k]\end{array}\right]. \qquad (3.47)$$

The MSE of the linear MMSE estimate is given by,

$$\varepsilon^2_{\min}[k] = \sigma^2_x[k] - \mathbf{k}_{x\mathbf{v}}[k]\mathrm{K}^{-1}_{\mathbf{yy}}[k]\mathbf{k}^{\mathrm{H}}_{x\mathbf{v}}[k]. \tag{3.48}$$

Theorem 3.2. Let $\mathbf{x}[k]$ denote a sequence of redundancy blocks that are generated using the DFT dithered SNQ signaling scheme. The signal is transmitted through a time-invariant Gaussian ISI channel. The linear-MMSE estimates of $\mathbf{x}[k]$, denoted by $\hat{\mathbf{x}}_{\mathrm{s}}[k]$, have constant mean square error (MSE) over time. In other words, $\varepsilon^2_{\min}[k] = \varepsilon^2_{\min}[k+1]$.

Proof. Without loss of generality, let $\sigma^2_x[k] = 1, \forall k$.

$$\begin{aligned}\varepsilon^2_{\min}[k] &= 1 - \left[\begin{array}{c:c} \mathbf{0} & {\mathbf{g}_0}^{\dagger^{\mathrm{H}}}[k] \end{array}\right] \left[\begin{array}{c:c} \mathbf{A}[k] & \mathbf{B}[k] \\ \hdashline \mathbf{C}[k] & \mathbf{D}[k] \end{array}\right] \left[\begin{array}{c} \mathbf{0} \\ \hdashline {\mathbf{g}_0}^{\dagger}[k] \end{array}\right] \\ &= 1 - {\mathbf{g}_0}^{\dagger^{\mathrm{H}}}[k]\mathbf{D}[k]{\mathbf{g}_0}^{\dagger}[k] \end{aligned} \tag{3.49}$$

where $\mathbf{D}[k]$ can be obtained through the matrix inversion lemma and,

$$\mathbf{D}[k] = \mathbf{E}[k] + \mathbf{E}[k]{\mathbf{G}_0}^{\dagger}[k]\mathbf{F}[k]{\mathbf{G}_0}^{\dagger^{\mathrm{H}}}[k]\mathbf{E}[k] \tag{3.50}$$

where,

$$\begin{aligned}\mathbf{E}[k] &\triangleq \left({\mathbf{G}_0}^{\dagger}[k]{\mathbf{G}_0}^{\dagger^{\mathrm{H}}}[k] + \mathrm{I}_N\right)^{-1} \\ &= \begin{bmatrix} \mathbf{E}_{1,1}[k] & \mathbf{E}_{1,2}[k] & \dots & \mathbf{E}_{1,M}[k] \\ \vdots & \vdots & \ddots & \vdots \\ \mathbf{E}_{M,1}[k] & \mathbf{E}_{M,2}[k] & \dots & \mathbf{E}_{M,M}[k] \end{bmatrix}, \end{aligned} \tag{3.51}$$

and

$$\mathbf{F}[k] \triangleq \left(\mathrm{I}_x - {\mathbf{G}_0}^{\dagger^{\mathrm{H}}}[k]\mathbf{E}[k]{\mathbf{G}_0}^{\dagger}[k]\right)^{-1}. \tag{3.52}$$

Recall that from Eqs. (C.2) and Lemma 5, we know that

$$\mathbf{E}[k+1] = \begin{bmatrix} \mathbf{E}_{1,1}[k] & \mathbf{E}_{1,2}[k]\omega^{l_1-l_2} & \cdots & \mathbf{E}_{1,M}[k]\omega^{l_1-l_M} \\ \mathbf{E}_{2,1}[k]\omega^{l_2-l_1} & \mathbf{E}_{2,2}[k] & \cdots & \mathbf{E}_{2,M}[k]\omega^{l_2-l_M} \\ \vdots & \vdots & \ddots & \vdots \\ \mathbf{E}_{M,1}[k]\omega^{l_M-l_1} & \mathbf{E}_{M,2}[k]\omega^{l_M-l_2} & \cdots & \mathbf{E}_{M,M}[k] \end{bmatrix} \tag{3.53}$$

and thus,

$$\mathbf{G}_0{}^{\dagger}[k] = \begin{bmatrix} \mathbf{G}_0^{(1)\dagger}[k]\omega^{l_1} \\ \mathbf{G}_0^{(2)\dagger}[k]\omega^{l_2} \\ \vdots \\ \mathbf{G}_0^{(M)\dagger}[k]\omega^{l_M} \end{bmatrix}$$

Combining Eqs. (3.53) and (3.54) and Lemma 5, and with a little bit of algebra, we can see that

$$\mathbf{F}[k+1] = \mathbf{F}[k]. \tag{3.54}$$

Finally, substitute Eqs. (3.5), (3.53) and (3.54) into Eq (3.50), and apply it to Lemma 5 again, we can see that

$$\mathbf{D}[k+1] = \begin{bmatrix} \mathbf{D}_{1,1}[k] & \mathbf{D}_{1,2}[k]\omega^{l_1-l_2} & \cdots & \mathbf{D}_{1,M}[k]\omega^{l_1-l_M} \\ \mathbf{D}_{2,1}[k]\omega^{l_2-l_1} & \mathbf{D}_{2,2}[k] & \cdots & \mathbf{D}_{2,M}[k]\omega^{l_2-l_M} \\ \vdots & \vdots & \ddots & \vdots \\ \mathbf{D}_{M,1}[k]\omega^{l_M-l_1} & \mathbf{D}_{M,2}[k]\omega^{l_M-l_2} & \cdots & \mathbf{D}_{M,M}[k] \end{bmatrix} \tag{3.55}$$

Similarly, with Eq. (C.3)

$$\mathbf{g}_0{}^{\dagger}[k] = \begin{bmatrix} \mathbf{g}_0^{(1)\dagger}[k]\omega^{l_1} \\ \mathbf{g}_0^{(2)\dagger}[k]\omega^{l_2} \\ \vdots \\ \mathbf{g}_0^{(M)\dagger}[k]\omega^{l_2} \end{bmatrix}$$

Finally, substitute Eqs. (3.55) and (3.56) into Eq. (3.49), we can conclude that

$$\varepsilon^2_{\min}[k+1] = \varepsilon^2_{\min}[k]. \tag{3.56}$$

□

3.6 Simulation Results for the SIMO System

The following simulation plots provide a verification of Eq. (3.33). Figures 3-5 and 3-6 present the simulation results for a single-input-single-output (SISO) discrete time-invariant AWGN channel; whereas Figures 3-7 and 3-8 correspond to simulations through an ISI channel extracted from the Surface Processes and Acoustic Communications Experiment 08 experiment (conducted off the coast of Martha's Vineyard by the Woods Hole Oceanographic Institute) with additional white noise.

Our goal is to identify the minimum channel SNR under which the overall scheme achieves the target rate, which is 4 [bits/s/Nyquist channel use]. Each realization of the simulation is characterized by three parameters: the signaling scheme (i.e. Nyquist, SNQ-2 or SNQ-3), the aggregate number of blocks combined to recover the original codeword and the AWGN channel SNR.

The plots are simulated in the following manner. Let M denote the number of dithered redundancy blocks that are combined for joint decoding. For each $M \in \{1, 2, \ldots, 6\}$, we locate the minimum SNR such that the original codeword can be decoded successfully from the M blocks by executing the following procedure. We begin by generating M dithered repetitions of the information vector and modulate it with either the Nyquist, SNQ-2 or SNQ-3 scheme. Then, the M redundancy blocks are transmitted through an AWGN channel with a designated SNR level. The receiver combines the M received redundancy blocks using an equalizer structure depicted

in Figure 2-7. Before processing the actual data signal, we train the equalizer with a sequence of training symbols so that the equalizer coefficients are converged to the optimal DFE coefficients. We take the soft-decision from the slicer input and compute the total spectral efficiency from the following expression,

$$\mathrm{R_{tot}} = \beta \log_2(1 + \mathrm{SNR_{slicer}}) \qquad \text{[bits/M channel uses]}, \tag{3.57}$$

where the slicer input SNR, $\mathrm{SNR_{slicer}}$, equals the signal power divided by the mean squared value of the slicer-error vector (slicer error power). If $\mathrm{R_{tot}}$ is greater than or equal to the target spectral efficiency, we note down the corresponding SNR, SNR^*, and number of redundancy blocks, M^*, for this transmission. This means that, if the information data symbols were coded at the target rate, the original codeword can be decoded without error with M^* redundancy blocks under channel SNR SNR^*. In other words, by transmitting M^* redundancy blocks of a codeword that has base code rate $R_\mathrm{b} = R_\mathrm{target}$, we can achieve an effective spectral efficiency of $\frac{\beta}{M^*} \times R_\mathrm{target}$ [bits/s/Hz] at signal to noise ratio SNR^*.

Figure 3-5 shows the effective spectral efficiency v.s. SNR plot for different transmission schemes. The red line shows the AWGN channel capacity and the dashed-black line shows the optimal bound for a 2-layer repetition coding scheme, given by Eq. (3.24). The magenta, green and blue curves outline the achievable rates of the Nyquist, SNQ-2 and SNQ-3 schemes, respectively. As SNR increases, the effective spectral efficiency increases for all signaling schemes. In addition, the faster the signaling rate, the closer its achievable rate to the AWGN channel capacity. It is important to emphasize that as the horizontal axis approaches the increasingly low SNR regime, the step of the staircase becomes smaller. This means that the gain in spectral efficiency for each redundancy block (i.e. effective spectral efficiency) decreases with decreasing SNR.

For the same data, Figure 3-6 plots the aggregate number of blocks required to decode the original codeword at each SNR. As depicted in the figure, the required aggregate number of decoding blocks decreases with increasing channel SNR. Moreover, the SNQ-β scheme touches the AWGN channel capacity curve $\forall M \leq \beta$ and achieves the layered repetition coding bound when M is an integer multiple of β, thus verifying Eq. (3.33).

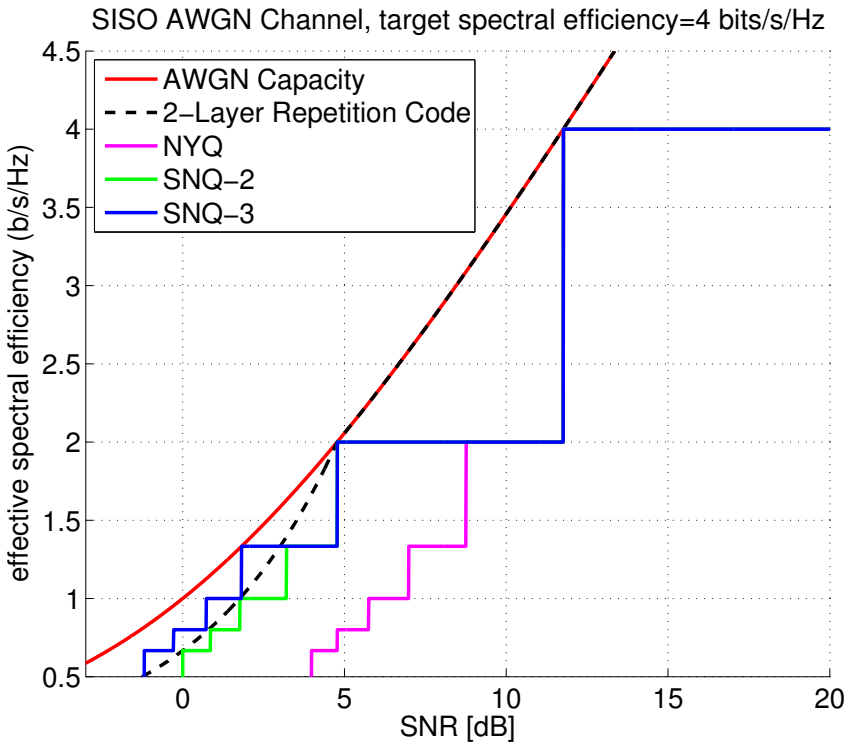

Figure 3-5: Effective achievable rate as a function of SNR for AWGN channel. The 2-layer repetition code bound is given by Eq. (3.24).

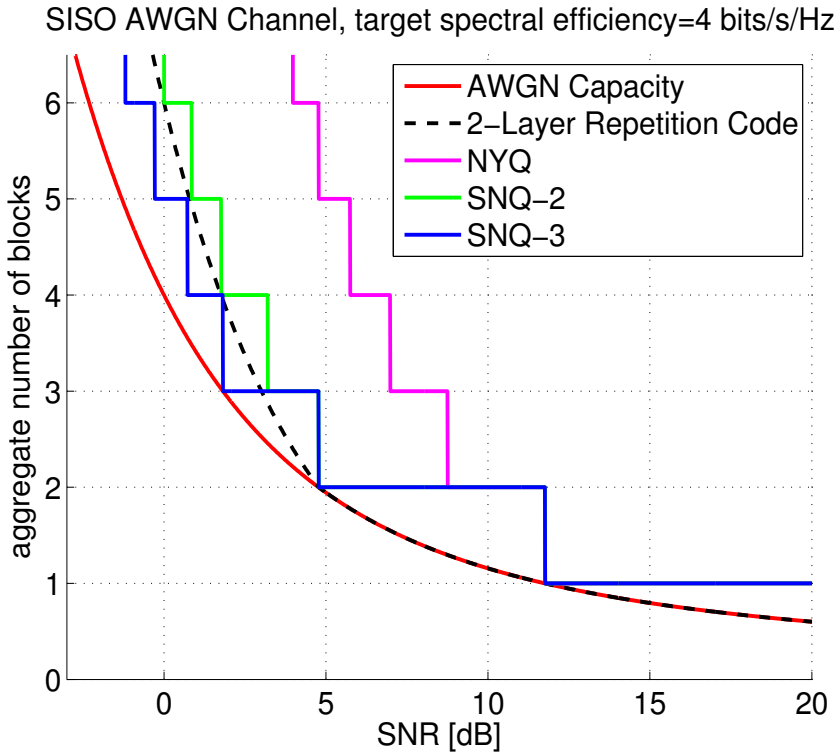

Figure 3-6: Aggregate number of blocks required to decode as a function of SNR for AWGN channel

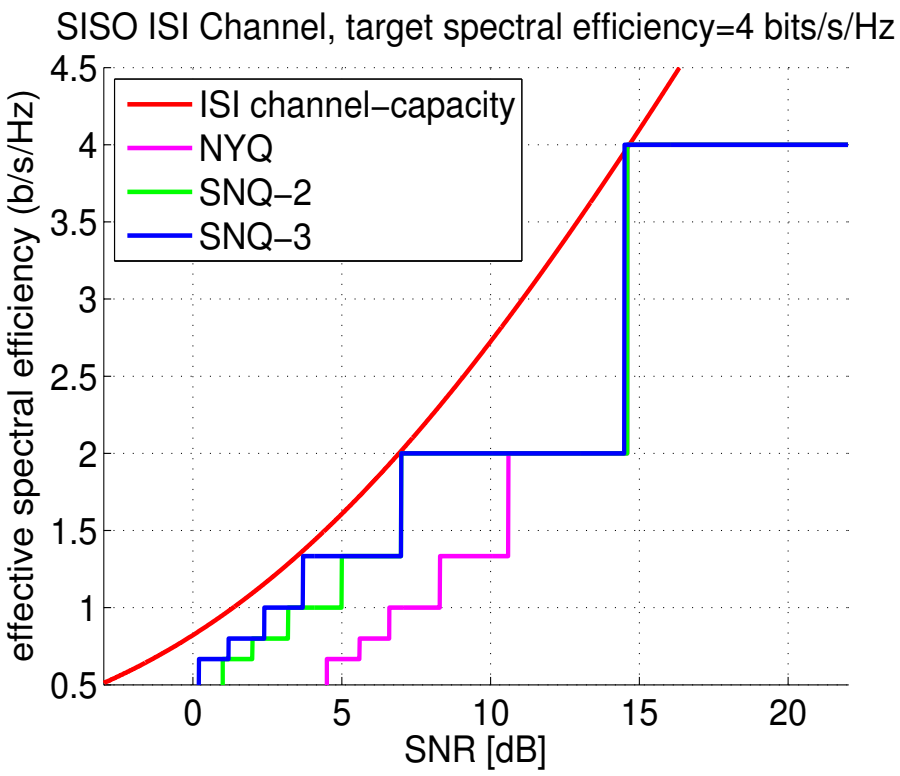

Figure 3-7: Effective achievable rate as a function of SNR for field ISI channel

In a similar manner, Figures 3-7 and 3-8 show the simulation results for the field ISI channel. The ISI channel capacity curve is obtained through Eq. (3.35). Similar to the AWGN case, SNQ-β also achieves channel capacity whenever the number of combined blocks is less than or equal to the signaling rate and Eq. (3.33) holds for ISI channels as well.

3.7 Simulation Results for the MIMO System

The SNQ-MIMO architecture as proposed in Section 2.7.2 is designed to perform rateless communication with the MIMO system. In this section, we present the simulation results for the SNQ-MIMO scheme for a time-invariant ISI channel. We show the that the SNQ-scheme yields capacity approaching performance even with a single redundancy block transmission and we compare its performance with the Vertical Bell Labs Space-Time Architecture (VBLAST) scheme [15].

The VBLAST architecture is widely used in MIMO communications and, with channel statistics, it is capacity achieving for fast fading channels. For capacity approaching performances, each transducer transmits an independent signal which is coded with respect to the capacity of

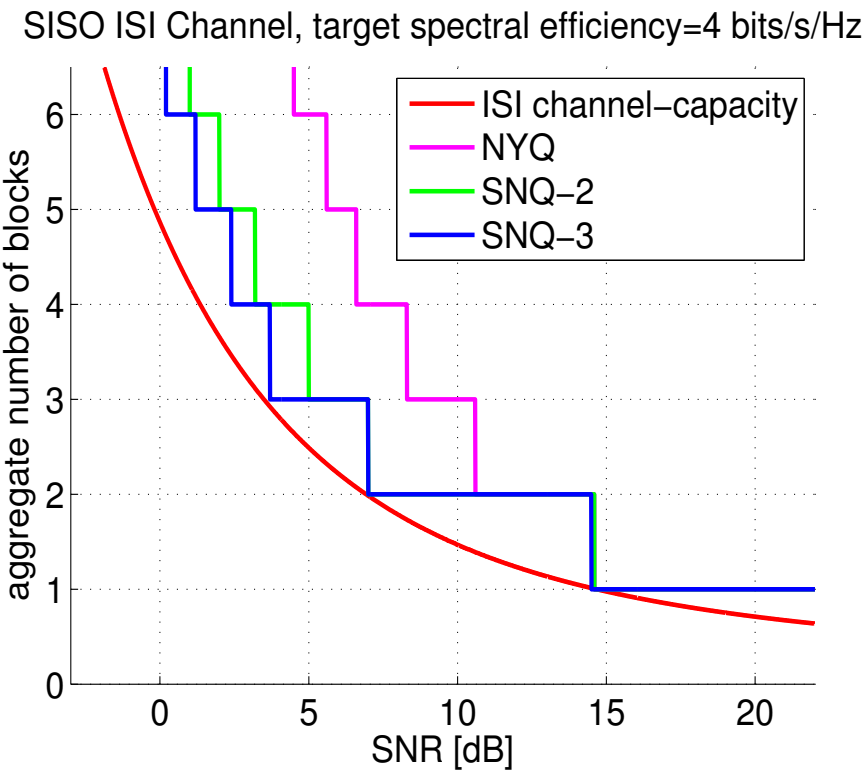

Figure 3-8: Aggregate number of blocks required to decode as a function of SNR for field ISI channel

the MIMO channel that it is transmitting through. Upon receiving all the signals on the other end of the MIMO channel, a decoder which incorporates the MMSE-SIC (successive interference cancellation) technique is used to decode the original messages. The VBLAST scheme becomes sub-optimal when we impose the constraint of equal code rates at all transmitters. This constraint is necessary due to the time-varying characteristics of the UWA channel, under which the transmitter does not have prior knowledge of the channel impulse response and cannot code each channel accordingly. As a result, the overall communication rate is limited by the minimum rate receiver. We call this equal rate VBLAST scheme as the conservative-VBLAST scheme. For simulation convenience, we do not apply the successive decoding scheme to compute the exact rate of the conservative-VBLAST scheme. For the purpose of performance comparison, it is sufficient for us to obtain an upper-bound of the conservative-VBLAST scheme by only decoding the first layer at all receivers; selecting the receiver with the highest rate, denoted by $R_{\max}$; and compute its achievable rate upper-bound with $R_{\max} \times T$, where T is the number of MIMO channels. This is an upper-bound due to the assumption of equal code rates at all transmitters; and conceivably, the actual achievable rate for the other layers may be even smaller than $R_{\max}$.

The simulation figures are generated with time-invariant ISI channels extracted from the KAM11 experiment. Each ISI channel has an impulse response of length 100, with additional noise obtained from the underwater environment. We compare the SNQ and the conservative-VBLAST achievable rates with channel capacity for the SISO and SNQ-MIMO4 (4 transducers and 4 hydrophones with SNQ signaling ratio $\beta = 4$) cases in Figure 3-9, where the horizontal axis corresponds to the transmitter SNR (i.e. total transmit power/noise power) and the vertical axis indicates spectral efficiency calculated from slicer SNR. Under the SISO setup, both schemes are capacity-achieving as expected. Under the MIMO-4 setup, however, the SNQ scheme shows a significant performance gain over the conservative-VBLAST scheme as SNR increases. Moreover, the effective spectral efficiency of the SNQ scheme almost coincides with the channel capacity curve.

Although the simulation shows capacity approaching rates for the SNQ-MIMO scheme, it is not capacity achieving for any MIMO channel. For some pathological channels (e.g. the MIMO channel that completely inverts the transmitter dither, in which case the achievable rate through the channel for the SNQ-MIMO scheme is 0), the SNQ-MIMO scheme could yield poor performance [16].

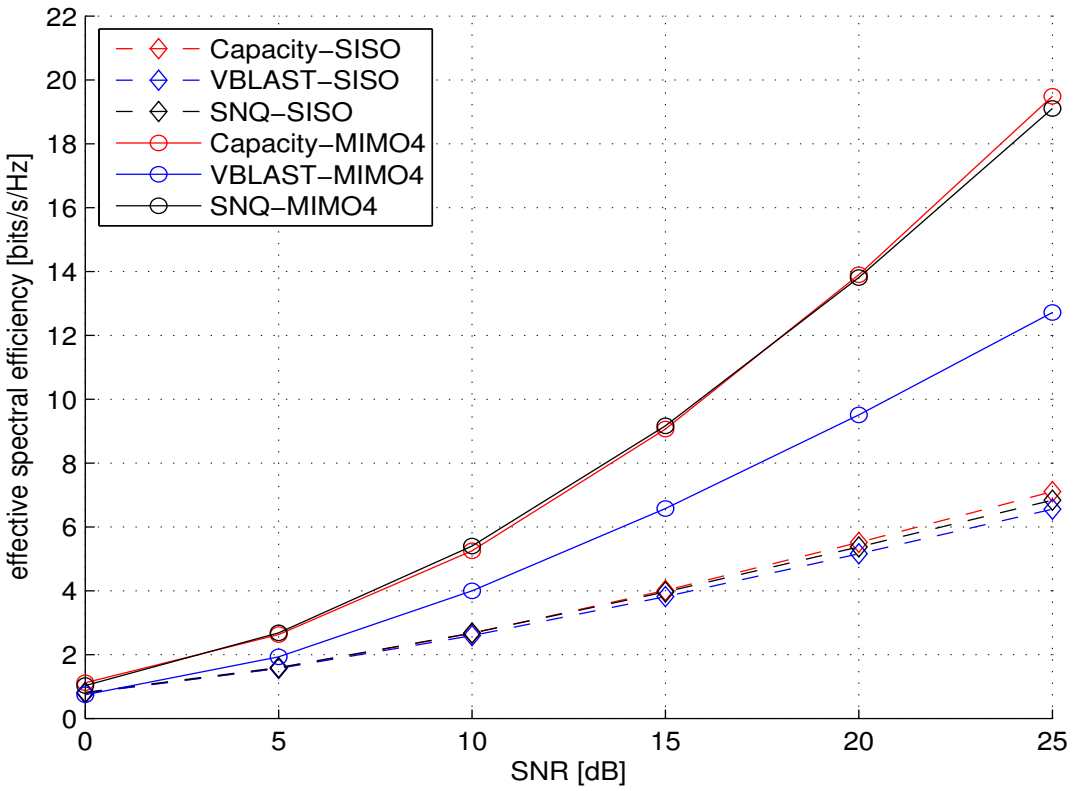

Figure 3-9: MIMO system simulation with channel extracted from KAM11 field data. Comparison among the theoretical channel capacity, the conservative-VBLAST scheme and the SNQ scheme. Effective spectral efficiency computed with equalizer slicer SNR.

3.8 Summary

In this chapter, we have shown that the SNQ dithered repetition coding scheme achieves channel capacity when the number of cumulative blocks, M, is less than or equal to the SNQ signaling rate, β. When M is greater than β, there is a gap between channel capacity and the achievable rate of the SNQ scheme whose expression is given by equation (3.33). Nevertheless, a large number of redundancy blocks is required only when the system is operating within the low SNR regime, where even the pure repetition coding scheme becomes increasingly efficient. Consequently, as shown in Figure 3-7, the gap between channel capacity and the SNQ scheme opens very slowly with increasing number of redundancy blocks.

In addition, we have shown that the DFT dithering scheme yields constant slicer SNR when decoded with an optimal MMSE-DFE. This property implies that if the information codeword is coded with a capacity achieving code for the AWGN channel at a rate matching the capacity of the intermediate system seen by the code, the overall proposed transceiver structure is capacity achieving. It is important to note that most dithering sequences other than the DFT dither will not satisfy this property. This can be verified by substituting another dither matrix $\mathbf{D}$ into Eq. (3.5) and observing that $\varepsilon^2_{\text{min}}[k]$ varies with k.

Chapter 4

Experiment Results

In this chapter, we present the results for the Kauai Acomms MURI 2011 (KAM11) experiment.

4.1 Experiment Background

The KAM11 experiments were conducted in shallow water of depth of 20-400 m off the western side of Kauai, Hawaii, during summer, 2011. A detailed description of the experiment can be found in [17]. The experiment data was transmitted under a variety of environment conditions and ranges using two of the KAM11 systems: the Woods Hole Oceanographic Institution Autonomous system (WHOI) and the Scripps Institute of Oceanography system (Scripps). Although both systems were equipped with multiple transducers and receive hydrophones, we used the WHOI system for single-input-multiple-output (SIMO) communication and the Scripps system for multiple-input-multiple-output (MIMO) communication. The transmitting signal power for both systems were bounded by maximum signal amplitude at each transducer. In other words, the maximal total available signal power increases linearly with the number of transducers in use.

The usable bandwidth of the WHOI system was 8.5 kHz to 17.5 kHz. There were two WHOI receive arrays, each had 24 hydrophones deployed in a vertical line array and with inter-element spacing of 5 cm and 20 cm, respectively. The sampling rate for both the transmit and receive systems were 39062.5 samples/second.

The Scripps system had eight transducers with an inter-element spacing of 7.5 meters, and two receive arrays, each had 16 hydrophones with a vertical inter-element spacing of 3.75 meters. The system operated in two modes: the narrowband mode in which the usable bandwidth was 20 kHz to 32 kHz and the wide-band mode in which the allowable bandwidth was increased to 10 kHz to 32 kHz. The sampling rate for both the transmit and receive systems were 100 kilo-samples/second. We investigate the performance of the SNQ-MIMO structure with the Scripps system by utilizing up to 4 transducers.

The experimental signals for both the WHOI and Scripps systems were transmitted repeatedly every 2 hours. At the end of each epoch, there was a silent period during which no signal was transmitted and only ambient noise data was collected. With power measurements of the received signals and the ambient noise signals, we can roughly estimate the underwater channel SNR. We make the assumption that the average noise power is time-invariant over each experiment epoch. In addition, in order to exploit the performance of the SNQ scheme at a wider range of SNRs, we have scaled ambient noise and add it to the received signal to emulate an environment with lower SNR.

In the experiment, the signal was modulated with two different pulse shape options: rectangular pulse and raised-cosine pulse with 20 percent excess bandwidth. The received signals are sampled at a rate of 6 samples per Nyquist symbol. All the signals, regardless of their signaling rate, were modulated with the QPSK constellation. Details of the KAM11 signal specifications are given in Appendix F.

In practice, communication systems require training under time-varying environments and the percentage of training symbols depends on the channel condition. Let us denote the percentage of training symbols by κ. Therefore, with base code rate R_{b}, modulation constellation representing τ bits/symbol and M redundancy blocks, the achievable effective spectral efficiency is given by,

$$\text{effective spectral efficiency} = (1-\kappa) \times \frac{\tau \times R_{\mathrm{b}}}{M} \ \text{[bits/s/Hz]}. \tag{4.1}$$

4.2 SIMO System

This section shows the experimental results of the SNQ scheme for the SIMO system as presented in section 2.7.1. The scheme is tested with two different LDPC base code rates: 1/2 and 9/10. Appendix E investigates the relationship between the LDPC code efficiency and its rate. Generally, the LDPC code efficiency decreases with the base code rate. Hence, the rate 9/10 code is more efficient than the rate 1/2 code. Nevertheless, the rate 1/2 code is also selected to test the SNQ scheme performance with fewer number of redundancy blocks under severe channel conditions (e.g. low SNR or large ISI), under which the rate 9/10 code requires a large number of redundancy blocks

for decoding. Recall that the transmitted signals are modulated with the QPSK constellation. This means, during each Nyquist period, two QPSK symbols (4 coded bits) would be transmitted for the SNQ-2 scheme, whereas one symbol (2 coded bits) is transmitted for the Nyquist scheme. In order to compare the SNQ-2 and the Nyquist schemes at the same transmission rate (i.e. number of bits transmitted per second), we would like to have the Nyquist symbols being modulated with the 16-QAM constellation. This way, 4 coded bits are transmitted per Nyquist period for the Nyquist scheme as well. As shown in Appendix D, we post-processed the experiment data to obtain an upper bound for the Nyquist signaling scheme with 16-QAM modulation.

The coded and modulated signal is transmitted through a single transducer and received at all of the 24 receiver hydrophones. Although by jointly combining signals from more hydrophones would yield a power gain, it also increases the decoding complexity and the convergence time of the equalizer coefficients. As a result, performance gain saturates when a large number of received signals are combined, and we hence only used signals received from six evenly spaced out hydrophones (i.e. hydrophones 1, 5, 9, 13, 17, 21) for decoding.

For each configuration (with a specific SNQ signaling rate and LDPC code rate), we start by attempting to decode the received signal with a single block. We choose to indicate a signal for a single realization as decodable if the bit error rate for this codeword is less than 10^{-6}. Due to the severe condition of the underwater environment, rate $9/10$ signals cannot be decoded with a single block for neither the Nyquist nor the SNQ scheme; at a minimum, two redundancy blocks are required. In contrast, rate $1/2$ signals are decodable from a single redundancy block. Then, we expand the experiment spectrum to cover a wider range of channel SNR by adding additional ambient noise to the received signals before decoding. In the experiment plots, the horizontal axis indicates the SNR, which is equal to the ratio of the total received signal power at all hydrophones and the total noise power at all hydropones. For each target SNR point, we find the minimum number of redundancy blocks ($M_{\min}(t)$) required for successfully decoding a single epoch and we average $M_{\min}(t)$ for 10 different epochs to obtain an ensemble average. Lastly, the effective spectral efficiency at this target channel SNR is calculated with Eq. (4.1) with $\kappa = 30\%$. For the KAM11 data, we have selected κ to be the minimum amount of training such that the SNQ2 (rate $9/10$) signal is decodable with two blocks. This corresponds to $\kappa \approx 30\%$.

Recall that the simulation plot presented at the end of Chapter 3 (Figure 3-7) shows a gain in effective spectral efficiency for the SNQ scheme over the Nyquist scheme. As demonstrated in Figure 4-1, the experiment results exhibit a similar trend. The green line and the red line, respectively, represent the Nyquist-16QAM and SNQ2-QPSK schemes with LDPC code rate 1/2. Here, the Nyquist 16-QAM line corresponds the upper-bound of the 16-QAM scheme described in Appendix D. We observe that the SNQ-2 scheme shows a gain of approximately 10dB over the Nyquist scheme. To further investigate the system performance with a higher base code rate, we plot the achievable region for the Nyquist-QPSK and SNQ2-QPSK schemes with the rate 9/10 LDPC code. The Nyquist-16QAM performance is not shown because the signal is not decodable even when four redundancy blocks are combined. Figure 4-1 indicates that under the given channel condition, the SNQ-2 with rate 1/2 code scheme yields the largest achievable region. If the channel condition is better and we are operating in a higher SNR regime, we would expect the SNQ2 rate 9/10 scheme to outperform the SNQ2 rate 1/2 scheme because the rate 9/10 LDPC code is more efficient than the rate 1/2 LDPC code (Appendix E).

4.3 MIMO System

This section presents the experiment results of the SNQ-MIMO system where 4 transducers and 6 receiver hydrophones are used. The received signals are decoded with a receiver system shown in Figure 2-11.

Table 4.1 shows the achievable rates calculated from slicer SNR for a single epoch. As a sanity check, we first look at the Scripps wide-band SIMO system. The SIMO scheme corresponds to the system with a single transducer and 6 receiver hydrophones. As shown by the first two columns of Table 4.1, the Nyquist and SNQ schemes achieve similar performances with a single block transmission, which is consistent with our analysis in Chapter 3. We next investigate the MIMO performance. Recall in Section 3.4, Eq. (3.25) shows the MIMO channel capacity expression, which strongly depends on the correlation among the MIMO channels. In the optimal case, where the channel matrix is well conditioned (e.g. an identity MIMO channel matrix), the channel capacity increases linearly with the number of MIMO channels. Interestingly, we observe a similar trend in the experiment results. The third and fourth columns list the effective spectral efficiency and bit rate for the MIMO system, and demonstrate an approximate linear relationship between the effec-

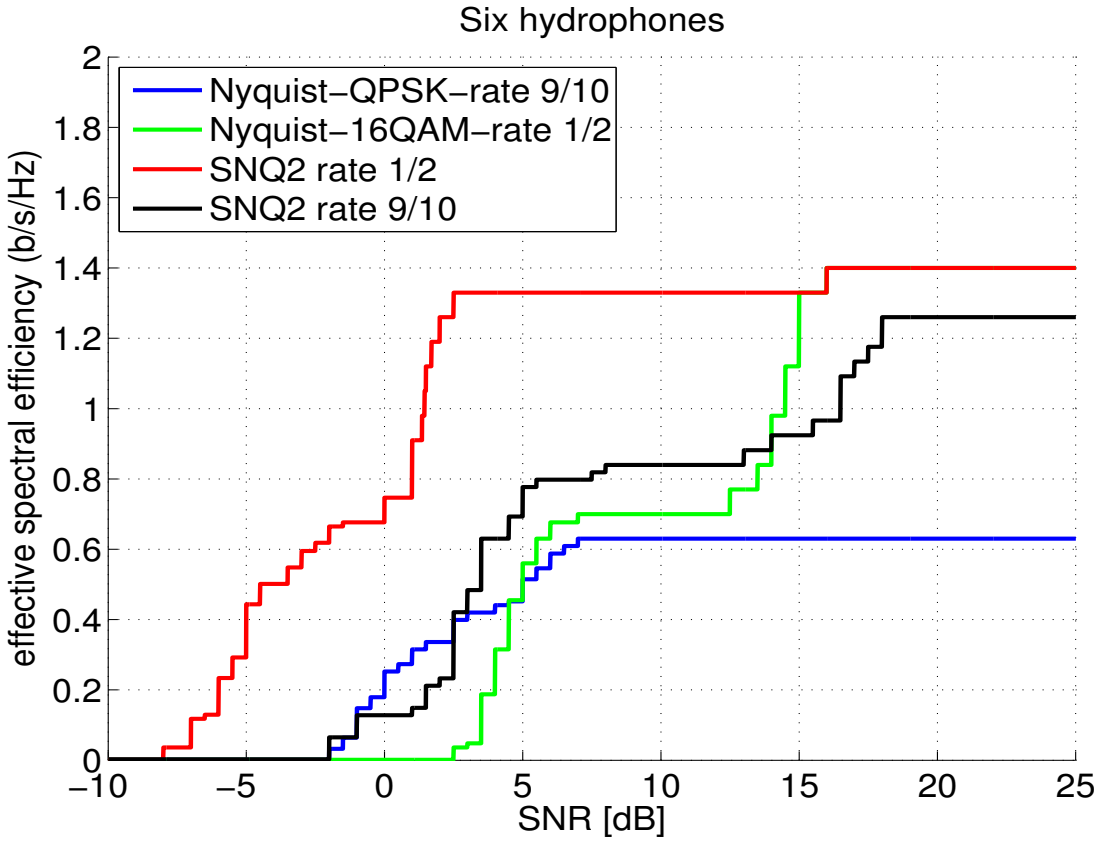

Figure 4-1: Experiment results from the WHOI SIMO system with 1 transducer and 6 hydrophones for the Nyquist and SNQ-2 schemes. Averaged performance over 10 epochs.

Table 4.1: Effective spectral efficiency calculated from slicer SNR and transmission rate for the SIMO and MIMO-4 schemes for the Scripps wide-band system.

	SIMO [b/s/Hz]	SIMO [Kb/s]	MIMO-4 [b/s/Hz]	MIMO-4 [Kb/s]
Nyquist	3.13	52.18	1.91	31.84
SNQ-2	3.09	51.51	3.51	58.51
SNQ-3	3.22	53.68	6.56	109.69
SNQ-4	3.43	57.18	8.22	137.03

tive spectral efficiency and SNQ signaling rate. Note that the performance of the MIMO-4 system is worse than SIMO system for the Nyquist scheme due to the slowly converging multi-decoder structure (Figure 2-11).

Next, we look at the system performance when a rate 1/2 LDPC code is applied. Figure 4-2 plots the effective spectral efficiency of the Nyquist and SNQ schemes for the 4-transducers-6-hydrophones system. The curve for each signaling scheme looks like a staircase with 5 transition points, which are resulted from averaging the effective spectral efficiencies over 5 epochs. The region beyond the last transition point corresponds to the regime that the received signals are decodable for all of the 5 epochs and this transition occurs almost at the same SNR for all four schemes. We observe that, once the system starts operating in the decodable region, the effective spectral efficiency increases linearly with the SNQ-signaling rate.

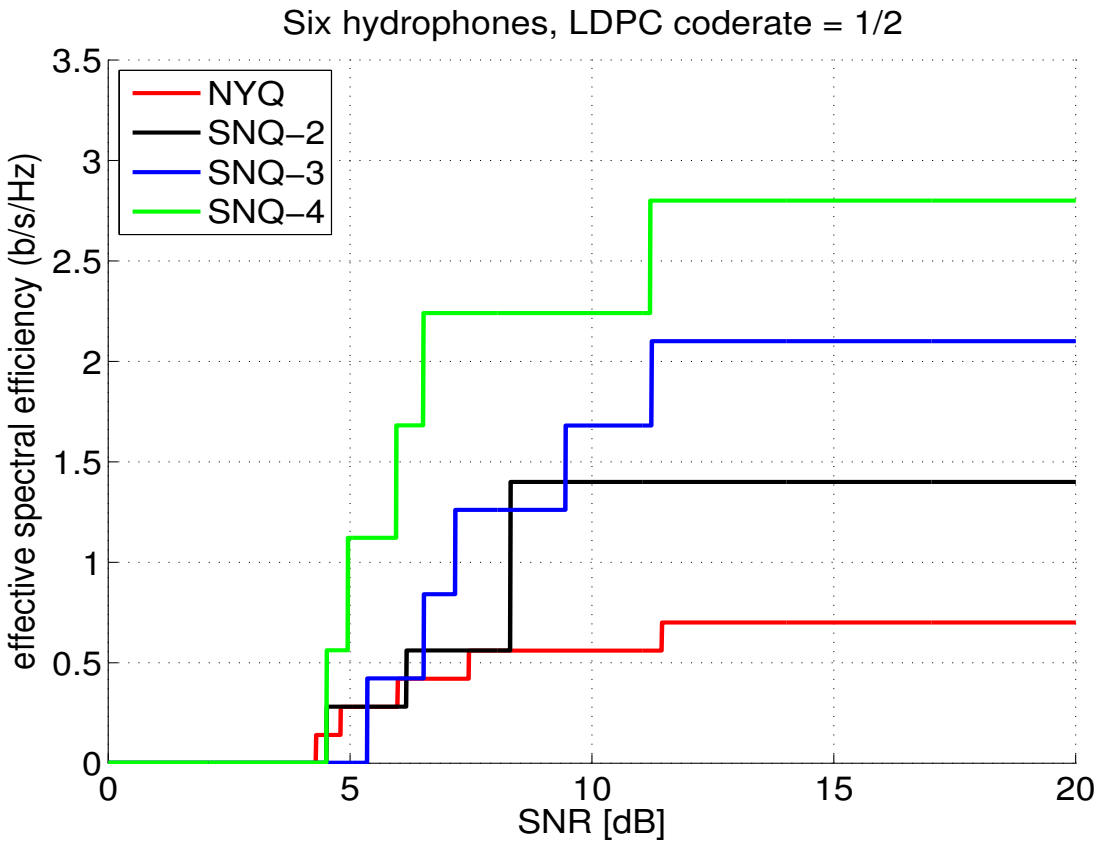

Figure 4-2: Experiment results from the Scripps MIMO system with 4 transducers and 6 hydrophones at LDPC code rate 1/2 for the Nyquist, SNQ-2, SNQ-3 and SNQ-4 schemes. Averaged performance over 5 epochs.

4.4 Summary

In this chapter, we presented results from the KAM11 experiment. For the WHOI SIMO system, we examined the effective spectral efficiency when combining multiple redundancy blocks for the Nyquist and the SNQ schemes, and at both low and high base code rates. The experiment results are consistent with the analytical and simulation results shown in Chapter 3, which indicate a higher effective spectral efficiency for the SNQ scheme than the Nyquist scheme when more than one redundancy block is combined. For the Scripps system, we compared the Nyquist and SNQ schemes under the MIMO-4 architecture with a single block transmission, in which case the SNQ scheme yields strictly better performance than Nyquist scheme. More specifically, the SNQ scheme demonstrates a linear gain in effective spectral frequency with respect to the SNQ signaling rate.

Chapter 5

Conclusion

This thesis has investigated the properties, achievable rates, and decoding strategies for the SNQ signaling scheme within an architecture supporting rateless communication over the UWA channel. We explored the performance of the SNQ scheme through simulations and experiments. The SNQ scheme out-performs the conventional Nyquist signaling scheme in the UWA environment and is proven to be capacity-achieving.

In this chapter, we summarize the results developed throughout the thesis, discuss about the SNQ scheme in practical applications and explore possible directions for future work.

5.1 Summary of Results and Discussion

The greatest challenges of UWA communication are due to its time-varying environment and rich underwater scatters, which translate into a time-varying ISI channel. To combat ISI, we adopt the traditional MMSE-DFE structure which is optimal under the assumption of perfect feedback. To overcome channel variation, we propose the SNQ scheme which allows rateless communication. Throughout the thesis, we developed an architecture for the SNQ scheme whose major components include the MMSE-DFE, SNQ modulator and demodulator. It achieves rateless communications at capacity-approaching rates.

The underlying concept behind the SNQ scheme is that with increasing SNQ signaling rate and dithered repetition coding, the SNQ scheme can generate an arbitrary number of mutually independent redundancy blocks each containing a little bit information about the codeword. The decoder keeps on collecting and combining these received blocks until the total spectral efficiency exceeds the base code rate R_b (i.e. when the transmitted codeword can be successfully decoded). More specifically, with the assumption that the channel is time-invariant during the transmission of each redundancy block (but can vary over different redundancy block transmissions), we have shown that the gain in spectral efficiency by receiving the i^{th} redundancy block fully uses the available channel capacity (i.e. $R^{(i)} = I(\mathbf{x}; \mathbf{y}^{(i)}) = C^{(i)}$, where $C^{(i)}$ is the channel capacity dur-

ing the transmission of the i^{th} redundancy block). In addition, the total spectral efficiency is the sum of individual effective spectral efficiency of each block (i.e. $R = \sum_{i=1}^{M} R^{(i)}$) as long as the total number of redundancy blocks is less than or equal to the SNQ signaling rate β. Combining these two results, we were able to conclude that the SNQ scheme is capacity-achieving whenever the number of redundancy blocks is less than or equal to the SNQ signaling rate. On the other hand, when the number of redundancy packets is greater than the signaling rate, the SNQ scheme becomes sub-optimal and its achievable rate is given by Eq. (3.24). Nevertheless, a large number of redundancy blocks is required only when the system is operating in the low SNR regime, where the gap between the achievable rate bound and channel capacity is typically small. Figure 3-4 summarizes the SNQ performance curves for different SNQ rates and under different SNRs. From Figure 3-4, it is clear that as β increases, the performance curve becomes increasingly close to the channel capacity.

Does this mean we should try to increase β indefinitely? The answer is "yes" in theory, but "no" in practice. In our analysis, we have made two assumptions: (1) the MMSE-DFE coefficients are fully adapted to their optimal values; and (2) the feedback decisions are all correct. However, in a practical system, the MMSE-DFE coefficients may take a significant amount of time to adapt to the optimal values. Specifically, increasing the signaling rate would increase the ISI introduced by SNQ signal modulation. If the filter coefficients are fully adapted and the feedback decisions are all correct, more ISI from SNQ modulation would not impair the system performance. However, with a time-varying channel and an adaptive MMSE-DFE, the overall system performance is directly related to the convergence rate of the MMSE-DFE. With more ISI to combat, the MMSE-DFE takes longer time to adapt. Hence, we would expect more errors in the MMSE-DFE estimates as a result of not fully-converged filter coefficients. Secondly, with more ISI from signal modulation, the SNR at the slicer is also lower. This increases the probability of error of the hard-decisions, which are fed back to the feedback filter and may lead to error propagation in practical systems. What is more catastrophic than raising the error probability is that, when the amount of error propagation exceeds a certain threshold (as discussed in Chapter 2), the MMSE-DFE will enter the failure mode and, thus cause decoding failure for all future symbols. In summary, faster signaling rate does not necessarily lead to better performance in practical systems. Depending on the channel condition, the signaling rate β should be kept in a regime such that the slicer SNR is not too low that it may run into the failure mode, but also not too high such that the system performance

can be improved by increasing the signaling rate.

As we can see, the performance of the MMSE-DFE is usually the bottleneck of the entire system's performance. Therefore, we have spent considerable effort into improving the performance of the MMSE-DFE specifically for the SNQ-scheme. To minimize the number of filter coefficients without hindering the system performance and avoid numerical errors caused by free coefficients, we incorporated the frequency-domain DFE which only equalizes in the frequency band that the SNQ signal occupies. This way, the optimal number of filter coefficients is constant in spite of the SNQ rate. In addition, to mitigate error propagation in the feedback system, we have adopted the delayed decision scheme. Through simulation, we observed that the threshold (i.e. minimum slicer SNR) of MMSE-DFE failure decreases with increasing delay decoding length and most of the improvements in delayed decoding is obtained in as few as two to three steps.

Lastly, a communication system is optimal only if a capacity-achieving code is applied to the original message. Conventional capacity-achieving codes are designed for time-invariant AWGN channels whose SNR is constant over each symbol. It is shown that the SNQ scheme with DFT dithering preserves this property and yields constant slicer SNR over each symbol. This property implies that any capacity-achieving code designed for the AWGN channel is equally effective when applied to the SNQ scheme. In other words, improvements in conventional coding techniques can be leveraged for the UWA channel.

5.2 Future Work

The SNQ architecture proposed in this thesis is optimal under the assumption of perfect-feedback in the MMSE-DFE. In practical systems, errors in the symbol estimates are fed back into the feedback filter and may cause errors on future symbols. In order to achieve channel capacity in practical systems, we need to utilize an error-correction code to avoid feedback errors. Some notion of iterative scheme between the MMSE-DFE and the channel decoder may be explored in the future in order to fully achieve the channel capacity in practice.

This thesis has proposed a complete architecture for the SNQ signaling scheme dedicated for the purpose of underwater acoustic communication. Although we have shown through analysis that

the SNQ signaling rate can be increased arbitrarily to ultimately achieve the channel capacity, the performance of the adaptive equalizer implies an upper-bound on the SNQ signaling rate. This is due to the fact that the higher the SNQ rate, the more ISI it imposes onto the received signal. It is a known problem that the RLS-adaptive equalizer gets trapped into a failure mode when running at low slicer SNR. Exploring other equalization schemes such as the channel-estimated equalizer may improve the overall SNQ scheme performance in practical systems.

In Chapters 3 and 4, simulation and experiment results of the MIMO-SNQ scheme demonstrated a significant gain in spectral efficiency over the conservative-VBLAST scheme. Moreover, the SNQ-MIMO effective spectral efficiency curve almost overlaps with the channel capacity curve. Appendix G further presents simulation results for the SNQ-MIMO system, which has demonstrated capacity-approaching performances. As a next step, an exact expression for the achievable rate of the MIMO-SNQ scheme may be derived and analyzed to verify the promising simulation results.

As explained in Chapter 2, the current decoder structure for the MIMO-SNQ scheme has long convergence time which increases linearly with the number of transducers. This is highly disadvantageous in a time-varying communication environment. A simpler receiver architecture such as a channel-estimator combined with dither-inverter may be exploited.

Appendix A

Example of Delayed DFE with 1 Delay Step

Figure A-1 shows an example of delayed-decision making procedure when the decision process is postponed by $D = 1$ symbol step. It depicts how symbol decisions are made based on a joint MSE decoding scheme and demonstrates the computation procedure for the joint MSE matrix.

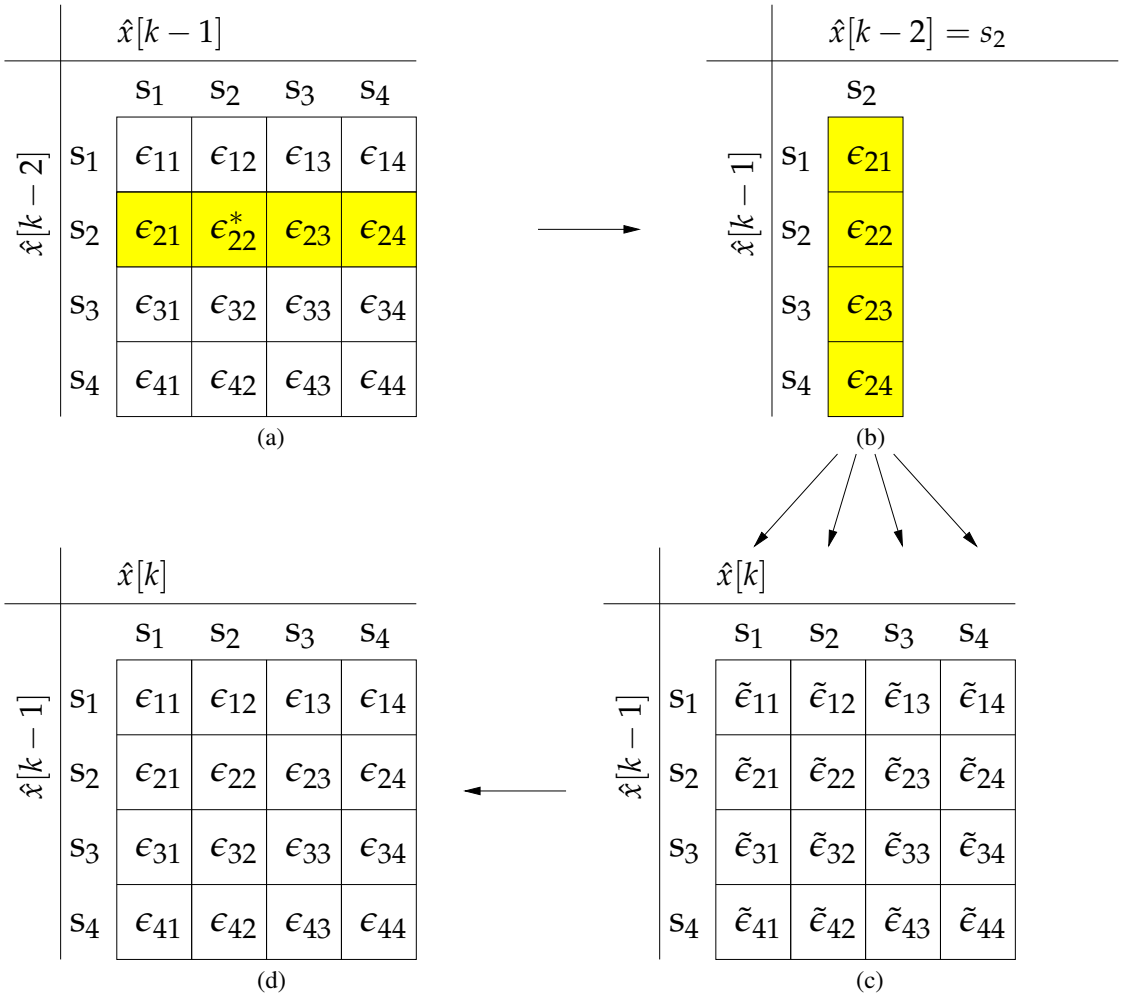

Figure A-1: Example of delayed decision with 1 extra delay tap. (a) Delay decision table for $\hat{x}[k-2]$, whose entries represent the joint MSE of $\hat{x}[k-2]$ and $\hat{x}[n-1]$. The minimum entry in the matrix, ϵ^*_{22}, yields the decision that $\hat{x}[k-2] = s_2$. (b)The column extracted from (a) and indicates the joint error between $\hat{x}[k-2]$ and $\hat{x}[k-1]$ when $\hat{x}[k-2] = s_2$. (3)The intermediate delay decision table, whose entries, $\tilde{\epsilon}_{i,j}$, equal to the slicer soft-decision error when $\hat{x}[k-1] = s_i$ and $\hat{x}[k] = s_j$. The column vector in (b) is added to each column in (c) to yield, (d) The delay decision table for $\hat{x}[k-1]$, whose minimum entry will be used to decide $\hat{x}[k-1]$.

First, part (a) shows the total decision matrix at time instance $[k-1]$, which is used to make decision on $\hat{x}[k-2]$. In this example, each symbol is chosen from a QPSK constellation, which has four symbol points: s_1, s_2, s_3 and s_4. As a result, there are 4^2 possible combinations for the two consecutive symbols $x[k-2]$ and $x[k-1]$ and it is represented by a 4×4 matrix as shown in (a). The element corresponding to the m^{th} row and n^{th} column of the matrix represents the joint MSE of the decisions: $\hat{x}[k-2] = s_m$ and $\hat{x}[k-n] = s_n$; and is obtained by substituting $\hat{x}[k-2] = s_m$ and $\hat{x}[k-1] = s_n$ into Eq. (2.29). Given this matrix, we identify the element that has minimum value, say it is ϵ_{22} and we denote this minimum value with ϵ_{22}^*. Therefore, we make the decision on symbol $\hat{x}[k-2] = s_2$. Conditioned on the decision of $\hat{x}[k-2]$, there is a MSE associated with each potential symbol for $\hat{x}[k-1]$, which is represented by the second row of the matrix. Part (b) shows the MSE vector for $\hat{x}[k-1]$ conditioned on the decision of $\hat{x}[k-2] = s_2$. Part (c) shows the squared slicer error, $(\hat{x}[k] - x_s[k])^2$ for all the possible combinations of symbols. Then, the column vector in part (b) is added to each column of the matrix in part (c) to generate the total MSE matrix for symbol $\hat{x}[k-1]$, as shown in part (d). This procedure repeats for every iteration.

Appendix B

Inverse of a cyclic phase shift matrix

This appendix presents a proof for the inverse of a cyclic phase shift matrix, which is defined as follows. Let $\mathbf{X}^{(M)}$ be a matrix consisting of $M \times M$ sub-matrices of equal size as defined in Eq. (B.1). Each sub-matrix $\mathbf{X}_{m,n}^{(M)}$ is a square matrix of size $K \times K$, for $1 \leq m, n \leq M$. The symbol α denotes a scalar constant and $\mathbf{I}$ is the identity matrix of the same size as the square blocks $\mathbf{X}_{m,n}^{(M)}$.

$$\mathbf{X}^{(M)} \triangleq \begin{bmatrix} \alpha\mathbf{I} + \mathbf{X}_{1,1}^{(M)} & \mathbf{X}_{1,2}^{(M)} & \cdots & \mathbf{X}_{1,M}^{(M)} \\ \mathbf{X}_{2,1}^{(M)} & \alpha\mathbf{I} + \mathbf{X}_{2,2}^{(M)} & \cdots & \mathbf{X}_{2,M}^{(M)} \\ \vdots & \vdots & \ddots & \vdots \\ \mathbf{X}_{M,1}^{(M)} & \mathbf{X}_{M,2}^{(M)} & \cdots & \alpha\mathbf{I} + \mathbf{X}_{M,M}^{(M)} \end{bmatrix} \tag{B.1}$$

Similarly, $\tilde{\mathbf{X}}^{(M)}$ is defined as,

$$\tilde{\mathbf{X}}^{(M)} \triangleq \begin{bmatrix} \alpha\mathbf{I} + \mathbf{X}_{1,1}^{(M)} & \mathbf{X}_{1,2}^{(M)}\omega^{l_1-l_2} & \cdots & \mathbf{X}_{1,M}^{(M)}\omega^{l_1-l_M} \\ \mathbf{X}_{2,1}^{(M)}\omega^{l_2-l_1} & \alpha\mathbf{I} + \mathbf{X}_{2,2}^{(M)} & \cdots & \mathbf{X}_{2,M}^{(M)}\omega^{l_2-l_M} \\ \vdots & \vdots & \ddots & \vdots \\ \mathbf{X}_{M,1}^{(M)}\omega^{l_M-l_1} & \mathbf{X}_{M,2}^{(M)}\omega^{l_M-l_2} & \cdots & \alpha\mathbf{I} + \mathbf{X}_{M,M}^{(M)} \end{bmatrix} \tag{B.2}$$

where $\omega = e^{-\frac{2\pi j}{N}}$, $j = \sqrt{-1}$, $l_i \in \{0, 1, 2, \ldots, R-1\}$, $R \in \mathbb{N}$.

Denote the inverse of $\mathbf{X}^{(M)}$ by $\mathbf{Y}^{(M)}$ and the inverse of $\tilde{\mathbf{X}}^{(M)}$ by $\tilde{\mathbf{Y}}^{(M)}$. $\mathbf{Y}^{(M)}$ and $\tilde{\mathbf{Y}}^{(M)}$ can both be decomposed into $M \times M$ sub-square-matrices of equal size, as shown in Eq. (B.3) and Eq. (B.4).

$$\begin{aligned}\mathbf{Y}^{(M)} &\triangleq [\mathbf{X}^{(M)}]^{-1} \\ &\triangleq \begin{bmatrix} \mathbf{Y}_{1,1}^{(M)} & \mathbf{Y}_{1,2}^{(M)} & \cdots & \mathbf{Y}_{1,M}^{(M)} \\ \mathbf{Y}_{2,1}^{(M)} & \mathbf{Y}_{2,2}^{(M)} & \cdots & \mathbf{Y}_{2,M}^{(M)} \\ \vdots & \vdots & \ddots & \vdots \\ \mathbf{Y}_{M,1}^{(M)} & \mathbf{Y}_{M,2}^{(M)} & \cdots & \mathbf{Y}_{M,M}^{(M)} \end{bmatrix}\end{aligned} \tag{B.3}$$

$$\begin{aligned}\tilde{\mathbf{Y}}^{(M)} &\triangleq [\tilde{\mathbf{X}}^{(M)}]^{-1} \\ &\triangleq \begin{bmatrix} \tilde{\mathbf{Y}}_{1,1}^{(M)} & \tilde{\mathbf{Y}}_{1,2}^{(M)} & \cdots & \tilde{\mathbf{Y}}_{1,M}^{(M)} \\ \tilde{\mathbf{Y}}_{2,1}^{(M)} & \tilde{\mathbf{Y}}_{2,2}^{(M)} & \cdots & \tilde{\mathbf{Y}}_{2,M}^{(M)} \\ \vdots & \vdots & \ddots & \vdots \\ \tilde{\mathbf{Y}}_{M,1}^{(M)} & \tilde{\mathbf{Y}}_{M,2}^{(M)} & \cdots & \tilde{\mathbf{Y}}_{M,M}^{(M)} \end{bmatrix}\end{aligned} \tag{B.4}$$

Lemma 5. $\tilde{\mathbf{Y}}^{(M)}$ and $\mathbf{Y}^{(M)}$ have the following relation:

$$\tilde{\mathbf{Y}}^{(M)} = \begin{bmatrix} \mathbf{Y}_{1,1}^{(M)} & \mathbf{Y}_{1,2}^{(M)}\omega^{l_1-l_2} & \cdots & \mathbf{Y}_{1,M}^{(M)}\omega^{l_1-l_M} \\ \mathbf{Y}_{2,1}^{(M)}\omega^{l_2-l_1} & \mathbf{Y}_{2,2}^{(M)} & \cdots & \mathbf{Y}_{2,M}^{(M)}\omega^{l_2-l_M} \\ \vdots & \vdots & \ddots & \vdots \\ \mathbf{Y}_{M,1}^{(M)}\omega^{l_M-l_1} & \mathbf{Y}_{M,2}^{(M)}\omega^{l_M-l_2} & \cdots & \mathbf{Y}_{M,M}^{(M)} \end{bmatrix} \tag{B.5}$$

Proof. Let Ω^{l_i} denote a diagonal matrix of size $K \times K$ whose diagonal entries are all equal to ω^{l_i}. More specifically, Ω^{l_i} is defined as follows,

$$\Omega^{l_i} \triangleq \begin{bmatrix} \omega^{l_i} & 0 & 0 & \dots & 0 \\ 0 & \omega^{l_i} & 0 & \dots & 0 \\ 0 & 0 & \omega^{l_i} & \dots & 0 \\ \vdots & \vdots & \vdots & \ddots & \vdots \\ 0 & 0 & 0 & \dots & \omega^{l_i} \end{bmatrix}_{K \times K} \tag{B.6}$$

$$\begin{aligned} \tilde{\mathbf{X}}^{(M)} &\triangleq \begin{bmatrix} \alpha\mathbf{I} + \mathbf{X}_{1,1}^{(M)} & \mathbf{X}_{1,2}^{(M)}\omega^{l_1-l_2} & \dots & \mathbf{X}_{1,M}^{(M)}\omega^{l_1-l_M} \\ \mathbf{X}_{2,1}^{(M)}\omega^{l_2-l_1} & \alpha\mathbf{I} + \mathbf{X}_{2,2}^{(M)} & \dots & \mathbf{X}_{2,M}^{(M)}\omega^{l_2-l_M} \\ \vdots & \vdots & \ddots & \vdots \\ \mathbf{X}_{M,1}^{(M)}\omega^{l_M-l_1} & \mathbf{X}_{M,2}^{(M)}\omega^{l_M-l_2} & \dots & \alpha\mathbf{I} + \mathbf{X}_{M,M}^{(M)} \end{bmatrix} \\ &= \underbrace{\begin{bmatrix} \Omega^{l_1} & 0 & \dots & 0 \\ 0 & \Omega^{l_2} & \dots & 0 \\ \vdots & \vdots & \ddots & \vdots \\ 0 & 0 & \dots & \Omega^{l_M} \end{bmatrix}}_{\text{A diagonal matrix}} \begin{bmatrix} \alpha\mathbf{I} + \mathbf{X}_{1,1}^{(M)} & \mathbf{X}_{1,2}^{(M)} & \dots & \mathbf{X}_{1,M}^{(M)} \\ \mathbf{X}_{2,1}^{(M)} & \alpha\mathbf{I} + \mathbf{X}_{2,2}^{(M)} & \dots & \mathbf{X}_{2,M}^{(M)} \\ \vdots & \vdots & \ddots & \vdots \\ \mathbf{X}_{M,1}^{(M)} & \mathbf{X}_{M,2}^{(M)} & \dots & \alpha\mathbf{I} + \mathbf{X}_{M,M}^{(M)} \end{bmatrix} \\ &\qquad \underbrace{\begin{bmatrix} \Omega^{-l_1} & 0 & \dots & 0 \\ 0 & \Omega^{-l_2} & \dots & 0 \\ \vdots & \vdots & \ddots & \vdots \\ 0 & 0 & \dots & \Omega^{-l_M} \end{bmatrix}}_{\text{A diagonal matrix}} \end{aligned} \tag{B.7}$$

Therefore,

$$\tilde{\mathbf{Y}}^{(M)} = \begin{bmatrix} \Omega^{-l_1} & 0 & \dots & 0 \\ 0 & \Omega^{-l_2} & \dots & 0 \\ \vdots & \vdots & \ddots & \vdots \\ 0 & 0 & \dots & \Omega^{-l_M} \end{bmatrix}^{-1} \begin{bmatrix} \alpha\mathbf{I} + \mathbf{X}_{1,1}^{(M)} & \mathbf{X}_{1,2}^{(M)} & \cdots & \mathbf{X}_{1,M}^{(M)} \\ \mathbf{X}_{2,1}^{(M)} & \alpha\mathbf{I} + \mathbf{X}_{2,2}^{(M)} & \cdots & \mathbf{X}_{2,M}^{(M)} \\ \vdots & \vdots & \ddots & \vdots \\ \mathbf{X}_{M,1}^{(M)} & \mathbf{X}_{M,2}^{(M)} & \cdots & \alpha\mathbf{I} + \mathbf{X}_{M,M}^{(M)} \end{bmatrix}^{-1}$$

$$\begin{bmatrix} \Omega^{l_1} & 0 & \dots & 0 \\ 0 & \Omega^{l_2} & \dots & 0 \\ \vdots & \vdots & \ddots & \vdots \\ 0 & 0 & \dots & \Omega^{l_M} \end{bmatrix}^{-1}$$

$$= \begin{bmatrix} \Omega^{l_1} & 0 & \dots & 0 \\ 0 & \Omega^{l_2} & \dots & 0 \\ \vdots & \vdots & \ddots & \vdots \\ 0 & 0 & \dots & \Omega^{l_M} \end{bmatrix} \begin{bmatrix} \mathbf{Y}_{1,1}^{(M)} & \mathbf{Y}_{1,2}^{(M)} & \dots & \mathbf{Y}_{1,M}^{(M)} \\ \mathbf{Y}_{2,1}^{(M)} & \mathbf{Y}_{2,2}^{(M)} & \dots & \mathbf{Y}_{2,M}^{(M)} \\ \vdots & \vdots & \ddots & \vdots \\ \mathbf{Y}_{M,1}^{(M)} & \mathbf{Y}_{M,2}^{(M)} & \dots & \mathbf{Y}_{M,M}^{(M)} \end{bmatrix} \begin{bmatrix} \Omega^{-l_1} & 0 & \dots & 0 \\ 0 & \Omega^{-l_2} & \dots & 0 \\ \vdots & \vdots & \ddots & \vdots \\ 0 & 0 & \dots & \Omega^{-l_M} \end{bmatrix}$$

$$= \begin{bmatrix} \mathbf{Y}_{1,1}^{(M)} & \mathbf{Y}_{1,2}^{(M)}\omega^{l_1-l_2} & \cdots & \mathbf{Y}_{1,M}^{(M)}\omega^{l_1-l_M} \\ \mathbf{Y}_{2,1}^{(M)}\omega^{l_2-l_1} & \mathbf{Y}_{2,2}^{(M)} & \cdots & \mathbf{Y}_{2,M}^{(M)}\omega^{l_2-l_M} \\ \vdots & \vdots & \ddots & \vdots \\ \mathbf{Y}_{M,1}^{(M)}\omega^{l_M-l_1} & \mathbf{Y}_{M,2}^{(M)}\omega^{l_M-l_2} & \cdots & \mathbf{Y}_{M,M}^{(M)} \end{bmatrix} \tag{B.8}$$

□

Appendix C
Proof of Theorem 2.1: Optimal Decoder for DFT Dithered Signaling scheme

This appendix contains the proof for Theorem 2.1. It derives an expression for the optimal DFE coefficients as a function of time k, the corresponding channel impulse matrix and the time-varying dithering vector.

Proof. First, Eqs. (2.32) and (2.34) follow directly from Eqs. (2.25) and (2.26). We will next show that Eqs. (2.35) and (2.36) hold.

Let the dithering sequence for the i^{th} redundancy block, $\mathbf{d}^{(i)}$, be composed of concatenations of the $(l_i+1)^{\text{th}}$ row of the $R \times R$ DFT matrix, $l_i \in \{0,1,2,\ldots,R-1\}$, $R \in \mathbb{N}$. Hence, every entry in $\mathbf{d}^{(i)}$ is equal to the previous entry multiplied by a constant phasor. In other words, $d^{(i)}[k+1] = d^{(i)}[k]e^{-\frac{2\pi j}{N}l_i} = d^{(i)}[k]\omega^{l_i}$, where $\omega = e^{-\frac{2\pi j}{N}}$, $j = \sqrt{-1}$. As given in Eq. (2.20), $\mathbf{d}^{(i)}[k]$ is a segment of the vector $\mathbf{d}^{(i)}$. Therefore, it follows that $\mathbf{d}^{(i)}[k+1] = \mathbf{d}^{(i)}[k]\omega^{l_i}$ and

$$\mathbf{D}^{(i)}[k+1] = \mathbf{D}^{(i)}[k]\omega^{l_i}. \tag{C.1}$$

Substituting Eqs. (2.30) and (C.1) into Eqs. (2.19) and (2.31) yields

$$\mathbf{G}_0^{(i)^\dagger}[k+1] = \mathbf{G}_0^{(i)^\dagger}[k]\omega^{l_i}, \tag{C.2}$$

$$\mathbf{g}_0^{(i)^\dagger}[k+1] = \mathbf{g}_0^{(i)^\dagger}[k]\omega^{l_i}, \tag{C.3}$$

$$\mathbf{G}_{\text{fb}}^{(i)^\dagger}[k+1] = \mathbf{G}_{\text{fb}}^{(i)^\dagger}[k]\omega^{l_i}. \tag{C.4}$$

Now, we can calculate the optimal MMSE-DFE coefficients using Eqs. (2.25) and (2.26). The feedforward filter coefficients, at each time k, are given as a function of the overall transformation

matrix $\mathbf{G}^{\dagger}[k]$ as:

$$\mathbf{h}_{\text{ff}}[k] = \frac{\mathbf{Q}[k]^{-1}\mathbf{g}_0^{\dagger}[k]}{1 + \mathbf{g}_0^{\dagger}[k]^{\text{H}}\mathbf{Q}[k]^{-1}\mathbf{g}_0^{\dagger}[k]}, \tag{C.5}$$

where $\mathbf{Q}[k]$ is given by,

$$\begin{aligned}\mathbf{Q}[k] &= \begin{bmatrix} \sigma_n^2\mathbf{I} & \mathbf{0} & \dots & \mathbf{0} \\ \mathbf{0} & \sigma_n^2\mathbf{I} & \dots & \mathbf{0} \\ \vdots & \vdots & \ddots & \vdots \\ \mathbf{0} & \mathbf{0} & \dots & \sigma_n^2\mathbf{I} \end{bmatrix} + \begin{bmatrix} {\mathbf{G}_0^{(1)}}^{\dagger}[k] \\ {\mathbf{G}_0^{(2)}}^{\dagger}[k] \\ \vdots \\ {\mathbf{G}_0^{(M)}}^{\dagger}[k] \end{bmatrix} \begin{bmatrix} \left[{\mathbf{G}_0^{(1)}}^{\dagger}[k]\right]^{\text{H}} & \dots & \left[{\mathbf{G}_0^{(1)}}^{\dagger}[k]\right]^{\text{H}} \end{bmatrix} \\ &= \begin{bmatrix} \sigma_n^2\mathbf{I} + {\mathbf{G}_0^{(1,1)}}^{\dagger}[k] & {\mathbf{G}_0^{(1,2)}}^{\dagger}[k] & \dots & {\mathbf{G}_0^{(1,M)}}^{\dagger}[k] \\ {\mathbf{G}_0^{(2,1)}}^{\dagger}[k] & \sigma_n^2\mathbf{I} + {\mathbf{G}_0^{(2,2)}}^{\dagger}[k] & \dots & {\mathbf{G}_0^{(2,M)}}^{\dagger}[k] \\ \vdots & \vdots & \ddots & \vdots \\ {\mathbf{G}_0^{(M,1)}}^{\dagger}[k] & {\mathbf{G}_0^{(M,2)}}^{\dagger}[k] & \dots & \sigma_n^2\mathbf{I} + {\mathbf{G}_0^{(M,M)}}^{\dagger}[k] \end{bmatrix} \end{aligned} \tag{C.6}$$

and

$${\mathbf{G}_0^{(i_1,i_2)}}^{\dagger}[k] \triangleq {\mathbf{G}_0^{(i_1)}}^{\dagger}[k] \left[{\mathbf{G}_0^{(i_2)}}^{\dagger}[k]\right]^{\text{H}}, \qquad i_1, i_2 \in \{1, 2, \dots, M\}. \tag{C.7}$$

Here, the time-variance of $\mathbf{h}_{\text{ff}}[k]$ at each symbol time k comes from the time-varying matrix $G^{\dagger}[k]$. Recall that $G^{\dagger}[k]$ is the coupled transformation of $\mathbf{G}[k]$ and $\mathbf{D}[k]$, where $\mathbf{G}[k]$ is assumed to be time-invariant during the each packet transmission, the time-variation property of the filter coefficients is a result of the inconsistency of $\mathbf{D}[k]$ from time to time. With the filter coefficients varying with k, the adaptive DFE structure will not converge. However, we show that with DFT dithering, the time-invariant and time-variant components of the DFE can be separated to result in a feasible decoding structure. Substituting Eq. (C.2) into Eq. (C.7), we can express ${\mathbf{G}_0^{(i_1,i_2)}}^{\dagger}[k+1]$ as a function of ${\mathbf{G}_0^{(i_1,i_2)}}^{\dagger}[k]$ as follows:

$${\mathbf{G}_0^{(i_1,i_2)}}^{\dagger}[k+1] = {\mathbf{G}_0^{(i_1,i_2)}}^{\dagger}[k]\omega^{l_{i_1} - l_{i_2}} \tag{C.8}$$

Then, substituting Eq. (C.8) into Eq. (C.6), $\mathbf{Q}[k+1]$ can be written in terms of $\mathbf{G}_0^{(i_1,i_2)^\dagger}[k]$:

$$\mathbf{Q}[k+1] = \begin{bmatrix} \sigma_n^2\mathbf{I} + \mathbf{G}_0^{(1,1)^\dagger}[k] & \mathbf{G}_0^{(1,2)^\dagger}[k]\omega^{l_1-l_2} & \dots & \mathbf{G}_0^{(1,M)^\dagger}[k]\omega^{l_1-l_M} \\ \mathbf{G}_0^{(2,1)^\dagger}[k]\omega^{l_2-l_1} & \sigma_n^2\mathbf{I} + \mathbf{G}_0^{(2,2)^\dagger}[k] & \dots & \mathbf{G}_0^{(2,M)^\dagger}[k]\omega^{l_2-l_M} \\ \vdots & \vdots & \ddots & \vdots \\ \mathbf{G}_0^{(M,1)^\dagger}[k]\omega^{l_M-l_1} & \mathbf{G}_0^{(M,2)^\dagger}[k+1]\omega^{l_M-l_2} & \dots & \sigma_n^2\mathbf{I} + \mathbf{G}_0^{(M,M)^\dagger}[k] \end{bmatrix} \tag{C.9}$$

Denote the inverses of $\mathbf{Q}[k]$ and $\mathbf{Q}[k+1]$ by $\mathbf{V}[k]$ and $\mathbf{V}[k+1]$, respectively. Partition $\mathbf{V}[k]$ and $\mathbf{V}[k+1]$ into $M \times M$ sub-matrices, ($\mathbf{V}[k]_{i,j}$ and $\mathbf{V}[k+1]_{i,j}$), of equal-size as shown in Eq. (C.10) and Eq. (C.11). The relation between $\mathbf{V}[k]$ and $\mathbf{V}[k+1]$ follows directly from Lemma 5 in Appendix B:

$$\begin{aligned} \mathbf{Q}[k]^{-1} &\triangleq \mathbf{V}[k] \\ &\triangleq \begin{bmatrix} \mathbf{V}[k]_{1,1} & \mathbf{V}[k]_{1,2} & \dots & \mathbf{V}[k]_{1,M} \\ \mathbf{V}[k]_{2,1} & \mathbf{V}[k]_{2,2} & \dots & \mathbf{V}[k]_{2,M} \\ \vdots & \vdots & \ddots & \vdots \\ \mathbf{V}[k]_{M,1} & \mathbf{V}[k]_{M,2} & \dots & \mathbf{V}[k]_{M,M} \end{bmatrix} \end{aligned} \tag{C.10}$$

$$\begin{aligned} \mathbf{Q}[k+1]^{-1} &\triangleq \mathbf{V}[k+1] \\ &\triangleq \begin{bmatrix} \mathbf{V}[k+1]_{1,1} & \mathbf{V}[k+1]_{1,2} & \dots & \mathbf{V}[k+1]_{1,M} \\ \mathbf{V}[k+1]_{2,1} & \mathbf{V}[k+1]_{2,2} & \dots & \mathbf{V}[k+1]_{2,M} \\ \vdots & \vdots & \ddots & \vdots \\ \mathbf{V}[k+1]_{M,1} & \mathbf{V}[k+1]_{M,2} & \dots & \mathbf{V}[k+1]_{M,M} \end{bmatrix} \end{aligned} \tag{C.11}$$

$$= \begin{bmatrix} \mathbf{V}[k]_{1,1} & \mathbf{V}[k]_{1,2}\omega^{l_1-l_2} & \dots & \mathbf{V}[k]_{1,M}\omega^{l_1-l_M} \\ \mathbf{V}[k]_{2,1}\omega^{l_2-l_1} & \mathbf{V}[k]_{2,2} & \dots & \mathbf{V}[k]_{2,M}\omega^{l_2-l_M} \\ \vdots & \vdots & \ddots & \vdots \\ \mathbf{V}[k]_{M,1}\omega^{l_M-l_1} & \mathbf{V}[k]_{M,2}\omega^{l_M-l_2} & \dots & \mathbf{V}[k]_{M,M} \end{bmatrix} \tag{C.12}$$

Using Eqs. (C.3) and (C.12), we then compute the numerator of the feedforward filter, described by Eqs. (C.5), at time k and $k+1$ as follows:

$$\begin{aligned}\tilde{\mathbf{h}}_{\text{ff}}[k] &\triangleq \begin{bmatrix} \tilde{\mathbf{h}}_{\text{ff}}^{(1)}[k] \\ \tilde{\mathbf{h}}_{\text{ff}}^{(2)}[k] \\ \vdots \\ \tilde{\mathbf{h}}_{\text{ff}}^{(M)}[k] \end{bmatrix} \triangleq \mathbf{Q}[k]^{-1}\mathbf{g}_0^{\dagger}[k] \\ &= \begin{bmatrix} \mathbf{V}[k]_{1,1} & \mathbf{V}[k]_{1,2} & \dots & \mathbf{V}[k]_{1,M} \\ \mathbf{V}[k]_{2,1} & \mathbf{V}[k]_{2,2} & \dots & \mathbf{V}[k]_{2,M} \\ \vdots & \vdots & \ddots & \vdots \\ \mathbf{V}[k]_{M,1} & \mathbf{V}[k]_{M,2} & \dots & \mathbf{V}[k]_{M,M} \end{bmatrix} \begin{bmatrix} {\mathbf{g}_0^{(1)}}^{\dagger}[k] \\ {\mathbf{g}_0^{(2)}}^{\dagger}[k] \\ \vdots \\ {\mathbf{g}_0^{(M)}}^{\dagger}[k] \end{bmatrix} \end{aligned} \tag{C.13}$$

$$\tilde{\mathbf{h}}_{\text{ff}}[k+1] \triangleq \mathbf{Q}[k+1]^{-1}\mathbf{g}_0^{\dagger}[k+1] \tag{C.14}$$

$$\begin{aligned} &= \begin{bmatrix} \mathbf{V}[k+1]_{1,1} & \mathbf{V}[k+1]_{1,2} & \dots & \mathbf{V}[k+1]_{1,M} \\ \mathbf{V}[k+1]_{2,1} & \mathbf{V}[k+1]_{2,2} & \dots & \mathbf{V}[k+1]_{2,M} \\ \vdots & \vdots & \ddots & \vdots \\ \mathbf{V}[k+1]_{M,1} & \mathbf{V}[k+1]_{M,2} & \dots & \mathbf{V}[k+1]_{M,M} \end{bmatrix} \begin{bmatrix} {\mathbf{g}_0^{(1)}}^{\dagger}[k+1] \\ {\mathbf{g}_0^{(2)}}^{\dagger}[k+1] \\ \vdots \\ {\mathbf{g}_0^{(M)}}^{\dagger}[k+1] \end{bmatrix} \\ &= \begin{bmatrix} \mathbf{V}[k]_{1,1} & \mathbf{V}[k]_{1,2}\omega^{l_1-l_2} & \dots & \mathbf{V}[k]_{1,M}\omega^{l_1-l_M} \\ \mathbf{V}[k]_{2,1}\omega^{l_2-l_1} & \mathbf{V}[k]_{2,2} & \dots & \mathbf{V}[k]_{2,M}\omega^{l_2-l_M} \\ \vdots & \vdots & \ddots & \vdots \\ \mathbf{V}[k]_{M,1}\omega^{l_M-l_1} & \mathbf{V}[k]_{M,2}\omega^{l_M-l_2} & \dots & \mathbf{V}[k]_{M,M} \end{bmatrix} \begin{bmatrix} {\mathbf{g}_0^{(1)}}^{\dagger}[k]\omega^{l_1} \\ {\mathbf{g}_0^{(2)}}^{\dagger}[k]\omega^{l_2} \\ \vdots \\ {\mathbf{g}_0^{(M)}}^{\dagger}[k]\omega^{l_M} \end{bmatrix} \\ &= \begin{bmatrix} \tilde{\mathbf{h}}_{\text{ff}}^{(1)}[k]\omega^{l_1} \\ \tilde{\mathbf{h}}_{\text{ff}}^{(2)}[k]\omega^{l_2} \\ \vdots \\ \tilde{\mathbf{h}}_{\text{ff}}^{(M)}[k]\omega^{l_M} \end{bmatrix} \end{aligned} \tag{C.15}$$

Next, let $\alpha[k]$ and $\alpha[k+1]$ denote the denominator of Eq. (C.5) at times k and $k+1$. Substituting Eqs. (C.15) and (C.3) into Eq. (C.5), it is shown below that $\alpha[k]$ and $\alpha[k+1]$ are equal:

$$\begin{aligned}
\alpha[k+1] &= 1 + \mathbf{g}_0^{\dagger}[k+1]^{\mathrm{H}}\mathbf{Q}[k+1]^{-1}\mathbf{g}_0^{\dagger}[k+1] \\
&= 1 + \begin{bmatrix} {\mathbf{g}_0^{(1)}}^{\dagger}[k+1]^{\mathrm{H}} & {\mathbf{g}_0^{(2)}}^{\dagger}[k+1]^{\mathrm{H}} & \dots & {\mathbf{g}_0^{(M)}}^{\dagger}[k+1]^{\mathrm{H}} \end{bmatrix} \begin{bmatrix} \tilde{\mathbf{h}}_{\mathrm{ff}}^{(1)}[k+1] \\ \tilde{\mathbf{h}}_{\mathrm{ff}}^{(2)}[k+1] \\ \vdots \\ \tilde{\mathbf{h}}_{\mathrm{ff}}^{(M)}[k+1] \end{bmatrix} \qquad \text{(C.16)} \\
&= 1 + \begin{bmatrix} {\mathbf{g}_0^{(1)}}^{\dagger}[k]^{\mathrm{H}}\omega^{-l_1} & {\mathbf{g}_0^{(2)}}^{\dagger}[k]^{\mathrm{H}}\omega^{-l_2} & \dots & {\mathbf{g}_0^{(M)}}^{\dagger}[k]^{\mathrm{H}}\omega^{-l_M} \end{bmatrix} \begin{bmatrix} \tilde{\mathbf{h}}_{\mathrm{ff}}^{(1)}[k]\omega^{l_1} \\ \tilde{\mathbf{h}}_{\mathrm{ff}}^{(2)}[k]\omega^{l_2} \\ \vdots \\ \tilde{\mathbf{h}}_{\mathrm{ff}}^{(M)}[k]\omega^{l_M} \end{bmatrix} \\
&= 1 + \begin{bmatrix} {\mathbf{g}_0^{(1)}}^{\dagger}[k]^{\mathrm{H}} & {\mathbf{g}_0^{(2)}}^{\dagger}[k]^{\mathrm{H}} & \dots & {\mathbf{g}_0^{(M)}}^{\dagger}[k]^{\mathrm{H}} \end{bmatrix} \begin{bmatrix} \tilde{\mathbf{h}}_{\mathrm{ff}}^{(1)}[k] \\ \tilde{\mathbf{h}}_{\mathrm{ff}}^{(2)}[k] \\ \vdots \\ \tilde{\mathbf{h}}_{\mathrm{ff}}^{(M)}[k] \end{bmatrix} \qquad \text{(C.17)} \\
&= \alpha[k] \qquad \text{(C.18)}
\end{aligned}$$

where Eq. (C.16) follows from Eq. (C.14) and Eq. (C.18) follows from Eq. (C.15).

Eqs. (C.15) and (C.18), respectively, give the relation between the numerators of the feedforward filters at time k and $k+1$, and the relation of the denominators of the feedforward filters at time k and $k+1$. Combining Eqs. (C.18) and (C.15), we have shown that the feedforward filter vector at time $k+1$ equals the feedforward filter coefficients at time k multiplied by a constant phasor

vector as follows,

$$\mathbf{h}_{\text{ff}}[k+1] \triangleq \begin{bmatrix} \mathbf{h}_{\text{ff}}^{(1)}[k+1] \\ \mathbf{h}_{\text{ff}}^{(2)}[k+1] \\ \vdots \\ \mathbf{h}_{\text{ff}}^{(M)}[k+1] \end{bmatrix} = \begin{bmatrix} \mathbf{h}_{\text{ff}}^{(1)}[k]\omega^{l_1} \\ \mathbf{h}_{\text{ff}}^{(2)}[k]\omega^{l_2} \\ \vdots \\ \mathbf{h}_{\text{ff}}^{(M)}[k]\omega^{l_M} \end{bmatrix} \tag{C.19}$$

Next, we will calculate the feedback filter coefficients $\mathbf{h}_{\text{fb}}[k]$ and $\mathbf{h}_{\text{fb}}[k+1]$ from Eqs. (C.4), (C.19) and (2.26).

$$\begin{aligned}
\mathbf{h}_{\text{fb}}[k+1] &= -\mathbf{G}_{\text{fb}}^{\dagger}[k+1]^{\text{H}}\mathbf{h}_{\text{ff}}[k+1] \\
&= -\begin{bmatrix} \mathbf{G}_{\text{fb}}^{(1)^{\dagger}}[k]^{\text{H}}\omega^{-l_1} & \mathbf{G}_{\text{fb}}^{(2)^{\dagger}}[k]^{\text{H}}\omega^{-l_2} & \dots & \mathbf{G}_{\text{fb}}^{(M)^{\dagger}}[k]^{\text{H}}\omega^{-l_M} \end{bmatrix} \begin{bmatrix} \mathbf{h}_{\text{ff}}^{(1)}[k]\omega^{l_1} \\ \mathbf{h}_{\text{ff}}^{(2)}[k]\omega^{l_2} \\ \vdots \\ \mathbf{h}_{\text{ff}}^{(M)}[k]\omega^{l_M} \end{bmatrix} \\
&= -\begin{bmatrix} \mathbf{G}_{\text{fb}}^{(1)^{\dagger}}[k]^{\text{H}} & \mathbf{G}_{\text{fb}}^{(2)^{\dagger}}[k]^{\text{H}} & \dots & \mathbf{G}_{\text{fb}}^{(M)^{\dagger}}[k]^{\text{H}} \end{bmatrix} \begin{bmatrix} \mathbf{h}_{\text{ff}}^{(1)}[k] \\ \mathbf{h}_{\text{ff}}^{(2)}[k] \\ \vdots \\ \mathbf{h}_{\text{ff}}^{(M)}[k] \end{bmatrix} \\
&= \begin{bmatrix} \mathbf{h}_{\text{fb}}^{(1)}[k] \\ \mathbf{h}_{\text{fb}}^{(2)}[k] \\ \vdots \\ \mathbf{h}_{\text{fb}}^{(M)}[k] \end{bmatrix} \\
&\triangleq \mathbf{h}_{\text{fb}}[k]
\end{aligned} \tag{C.20}$$

We have shown that the feedback filter coefficients, $\mathbf{h}_{\text{fb}}[k]$, are time-invariant.

Without loss of generality, assume decoding starts at the first symbol ($k = 0$). Recall that $\mathbf{x}^{(i)}[0]$

is dithered by $d^{(i)}[0]$, the first entry of the $(l_i+1)^{\text{th}}$ row of the $R \times R$ DFT matrix. We then have $d^{(i)}[0] = \omega^{l_i \times 0} = 1$. We interpret the feedforward filter at $k = 0$, $\mathbf{h}_{\text{ff}}^{(i)}[0]$, as the time-invariant portion of the feedforward filter. Modified in time only by the effects of dithering, the feedforward at time k is given by,

$$\mathbf{h}_{\text{ff}}^{(i)}[k] = \mathbf{h}_{\text{ff}}^{(i)}[0]\omega^{kl_i} \tag{C.21}$$

and the feedback filter, $\mathbf{h}_{\text{fb}}[k]$ is time-invariant such that,

$$\mathbf{h}_{\text{fb}}^{(i)}[k] = \mathbf{h}_{\text{fb}}^{(i)}[0]. \tag{C.22}$$

The numerical expression for the soft-estimates of the transmitted signal is described by Eq. (2.27). Combining Eqs. (2.27), (C.21) and (C.22), we can develop the structure of the DFE system.

$$\begin{aligned}
\hat{x}_{\text{s}}[k] &= \mathbf{h}_{\text{ff}}[k]^{\text{H}}\mathbf{y}_{\text{ff}}[k] + \mathbf{h}_{\text{fb}}[k]^{\text{H}}\hat{\mathbf{x}}_{\text{fb}}[k] \\
&= \begin{bmatrix} [\mathbf{h}_{\text{ff}}^{(1)}[0]\omega^{(k)l_1}]^{\text{H}}\mathbf{y}_{\text{ff}}^{(1)}[k] \\ [\mathbf{h}_{\text{ff}}^{(2)}[0]\omega^{(k)l_2}]^{\text{H}}\mathbf{y}_{\text{ff}}^{(2)}[k] \\ \vdots \\ [\mathbf{h}_{\text{ff}}^{(M)}[0]\omega^{(k)l_M}]^{\text{H}}\mathbf{y}^{(M)}[k] \end{bmatrix} + \begin{bmatrix} \mathbf{h}_{\text{fb}}^{(1)}[0]^{\text{H}}\hat{\mathbf{x}}_{\text{fb}}[k] \\ \mathbf{h}_{\text{fb}}^{(2)}[0]^{\text{H}}\hat{\mathbf{x}}_{\text{fb}}[k] \\ \vdots \\ \mathbf{h}_{\text{fb}}^{(M)}[0]^{\text{H}}\hat{\mathbf{x}}_{\text{fb}}[k] \end{bmatrix} \\
&= \begin{bmatrix} \mathbf{h}_{\text{ff}}^{(1)}[0]^{\text{H}}\omega^{-(k)l_1}\mathbf{y}_{\text{ff}}^{(1)}[k] \\ \mathbf{h}_{\text{ff}}^{(2)}[0]^{\text{H}}\omega^{-(k)l_2}\mathbf{y}_{\text{ff}}^{(2)}[k] \\ \vdots \\ \mathbf{h}_{\text{ff}}^{(M)}[0]^{\text{H}}\omega^{-(k)l_M}\mathbf{y}_{\text{ff}}^{(M)}[k] \end{bmatrix} + \mathbf{h}_{\text{fb}}[k]^{\text{H}}\hat{\mathbf{x}}_{\text{fb}}[k] \\
&= \begin{bmatrix} \mathbf{h}_{\text{ff}}^{(1)}[0]^{\text{H}}d^{(1)}[k]^{*}\mathbf{y}_{\text{ff}}^{(1)}[k] \\ \mathbf{h}_{\text{ff}}^{(2)}[0]^{\text{H}}d^{(2)}[k]^{*}\mathbf{y}_{\text{ff}}^{(2)}[k] \\ \vdots \\ \mathbf{h}_{\text{ff}}^{(M)}[0]^{\text{H}}d^{(M)}[k]^{*}\mathbf{y}_{\text{ff}}^{(M)}[k] \end{bmatrix} + \mathbf{h}_{\text{fb}}[0]^{\text{H}}\hat{\mathbf{x}}_{\text{fb}}[k]
\end{aligned} \tag{C.23}$$

where $\mathbf{h}_{\text{fb}}[k] = \mathbf{h}_{\text{fb}}[0] \triangleq \left[\mathbf{h}_{\text{fb}}^{(1)}[0] + \mathbf{h}_{\text{fb}}^{(2)}[0] + \ldots + \mathbf{h}_{\text{fb}}^{(M)}[0]\right]$. □

Appendix D
Procedure for Generating 16-QAM Nyquist Signals

As described in chapter 4, the transmitted signal was modulated with QPSK constellation, such that each symbol represents two binary bits. The mapping is shown in Figure D-1.

With QPSK modulation, two bits are transmitted during each Nyquist symbol period. In other

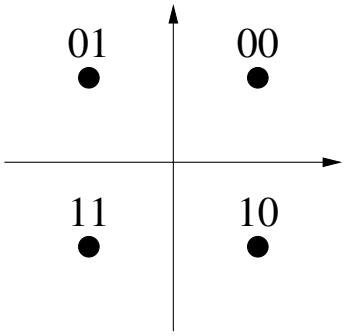

Figure D-1: QPSK constellation with gray coding scheme.

words, the Nyquist signaling scheme transmits two coded bits per second per Hz; whereas the SNQ-2 signaling scheme transmits two QPSK symbols (4 coded bits) per second per Hz. In order to make a fair comparison between the Nyquist and SNQ-2 scheme, we need to map the Nyquist symbols to a 16-QAM constellation such that the number of bits transmitted per Nyquist period will be comparable to the SNQ-2 scheme. We perform the following steps to obtain an upper-bound of the experiment transmission rate for 16-QAM modulation.

In the experiment, what we transmitted are QPSK symbols as shown in Figure D-1, where every two bits map to one QPSK symbol. On the other hand, a 16-QAM constellation is shown in Figure D-2. Let us first consider an alternate scheme: constraint 16-QAM scheme where all symbols are mapped to one of the outer four symbols. In the mapping scheme shown in Figure D-2, only symbols representing 0010, 1010, 0000 and 1000 are used. Because the outer four symbols have the least number of neighbors resulting in minimum probability of symbol error among all 16 constellation points, the expected symbol error rate with this constraint 16-QAM modulation scheme would be lower than the probability of symbol error rate of the actual 16-QAM modu-

lation scheme. Hence, the constraint 16-QAM scheme provides an upper bound of the 16-QAM scheme.

Now, let us consider the experiment setup. In the experiment, the transmitted signal is limited by maximum signal amplitude. Therefore, modulation with QPSK constellation can be interpreted as modulating with 16-QAM constellation where only the outer four symbols are used, which are indicated with arrows in Figure D-2. Therefore, by decoding the received signal with a 16-QAM constellation in the equalizer, the decoded signal would yield symbol error rate of the constraint 16-QAM scheme. Next, in order to evaluate the performance of the entire system, we need to map symbol estimates to binary bits and eventually decode it with LDPC code. Originally, each QPSK symbol is mapped to two bits whereas if 16-QAM is transmitted, each symbol would be decoded into four binary bits. What is a meaningful mapping scheme? First, let us look at the 16-QAM constellation as shown in Figure D-2(a). Due to symmetry property of the gray coding scheme, the bit error rate is constant with respect to constant relative symbol distance for the outer four symbols. For example, assume the transmitted symbol is "1010", which is colored in yellow. Figure D-2(b) indicates the bit error rate if the transmitted symbol is decoded incorrectly. Say the symbol "1010" is incorrectly decoded into "1110", which has a relative distance of one unit. This corresponds to bit error rate of $3/4$.

Knowing the transmitted symbol and its corresponding two binary bits with respect to the QPSK constellation; the relative distance between the decoded symbol and the transmitted symbol based on a 16-QAM constellation, we will map the decoded 16-QAM symbol in the following manner. Let ϵ denote the probability of bit error based on the distance between the known transmitted symbol and the decoded symbol. Suppose the transmitted symbol is s^*, which maps to two binary bits $b_1 b_2$ and the decoded symbol is $\hat{s}$, which maps to $\hat{b}_1 \hat{b}_2$. The mapping procedure is shown in Figure **??**, where $\hat{b} \in \mathbf{U}[0,1]$ means $\hat{b}_1$ is drawn from the uniform distribution

$$\begin{cases} P(x=0) = \frac{1}{2} \\ P(x=1) = \frac{1}{2} \end{cases} \tag{D.1}$$

and $\hat{b} = \bar{b}$ indicates the decision variable $\hat{b}$ is the complement of b.

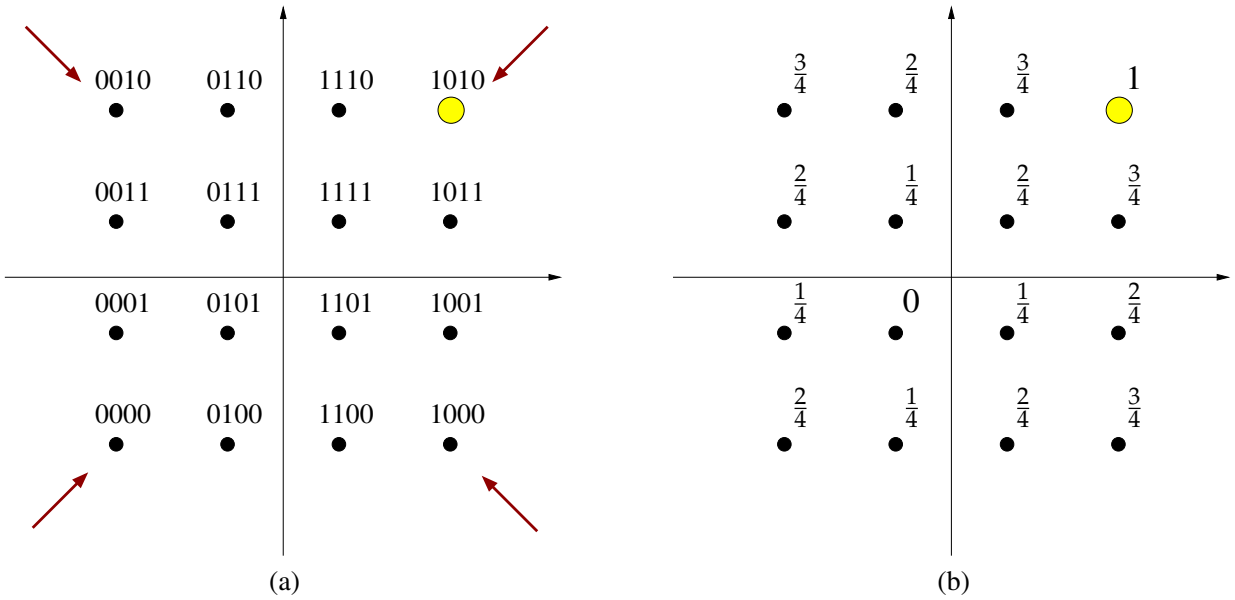

Figure D-2: (a) shows the 16-QAM constellation with gray coding scheme. The outer four symbols (indicated by arrows) correspond to symbols mapped from the QPSK constellation. (b) shows the bit error rate of each symbol if the transmitted symbol was '1010' as indicated by the yellow dot.

If $\epsilon = 1$
$\hat{b}_1 = b_1$ and $\hat{b}_2 = b_2$

If $\epsilon = \frac{3}{4}$
$\hat{b}_1 = b_1$ and $\hat{b}_2 \in \mathbf{U}[0,1]$

If $\epsilon = \frac{2}{4}$
$\hat{b}_1 = b_1$ and $\hat{b}_2 = \bar{b}_2$

If $\epsilon = \frac{1}{4}$
$\hat{b}_1 \in \mathbf{U}[0,1]$ and $\hat{b}_2 = \bar{b}_2$

If $\epsilon = 0$
$\hat{b}_1 = \bar{b}_1$ and $\hat{b}_2 = \bar{b}_2$

Figure D-3: Symbol to bits mapping procedure for a 16-QAM constellation

Appendix E
Efficiency Analysis for LDPC Code with QPSK Modulation

Throughout the analysis of the SNQ scheme, we have always made the assumption that there exists a capacity-achieving code. Although the channel coding theorem has proven the achievability of channel capacity, there is a gap between achievable rate and the channel capacity under the constraint of a fixed codeword length, symbol constellation and a practical code, such as the LDPC code. Figure E-1 shows the efficiency of LDPC code of codeword length of 64,800 bits when modulated with QPSK constellation. The values are obtained from [18]. The x-axis indicates the LDPC coderate and the y-axis corresponds to its efficiency, which is attained in the following manner. For example, for the left-most point which corresponds to coderate $1/4$. Information bits of block length 16,200 are coded with the rate $1/4$ LDPC code to produce a codeword of length 64,800. The codeword is mapped to a QPSK constellation to generate a vector of 32,400 symbols. The coded symbols are then transmitted through an AWGN channel with different SNR. The code is considered to be decodable (error-free) when its packet error rate is less than 10^{-7}. Let $C(R_{\mathrm{b}})$ denote the channel capacity [bits/s/Hz] at the minimum decodable SNR when the base LDPC coderate is equal to R_{b}. Then, efficiency is given by,

$$\text{efficiency}(R_{\mathrm{b}}) = \frac{R_{\mathrm{b}}}{C(R_{\mathrm{b}})}.$$

Figure E-1 indicates that the LDPC code yields better performance at higher coderate. Unfortunately, we do not always have the freedom of choosing the coderate. When the channel SNR is low, we are forced to operate in the low coderate regime. In the experiment, we have tested the SNQ scheme at two coderate: $1/2$ and $9/10$.

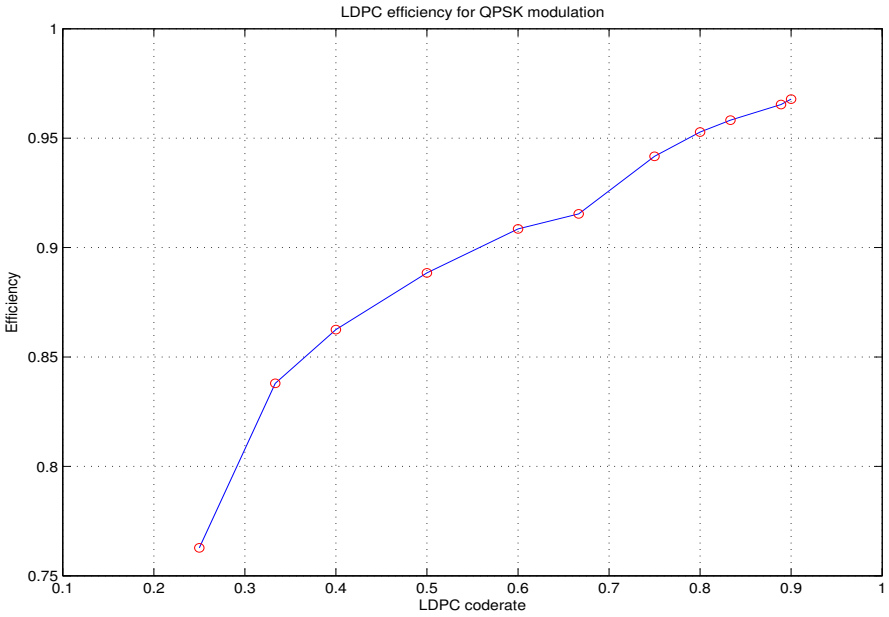

Figure E-1: Efficiency plot of LDPC code with QPSK modulation. [Efficiency = LDPC coderate / QPSK spectral efficiency], where the codeword is decodable if its bit error rate is below 10^{-7}.

Appendix F

KAM11 Signal Specifications

F.1 KAM11 Signal Specification

TX2 Useable transmit bandwidth	8.5kHz $\sim$ 17.5kHz
Sampling Rate	39062.5 samples/second
Signal bandwidth	6.51kHz (6 samples per Nyquist symbol)
Carrier Frequency (f_c)	13kHz
Signal occupied bandwidth	9.74kHz $\sim$ 16.25kHz
HPF	No

Table F.1: TX2: WHOI Autonomous Source Array

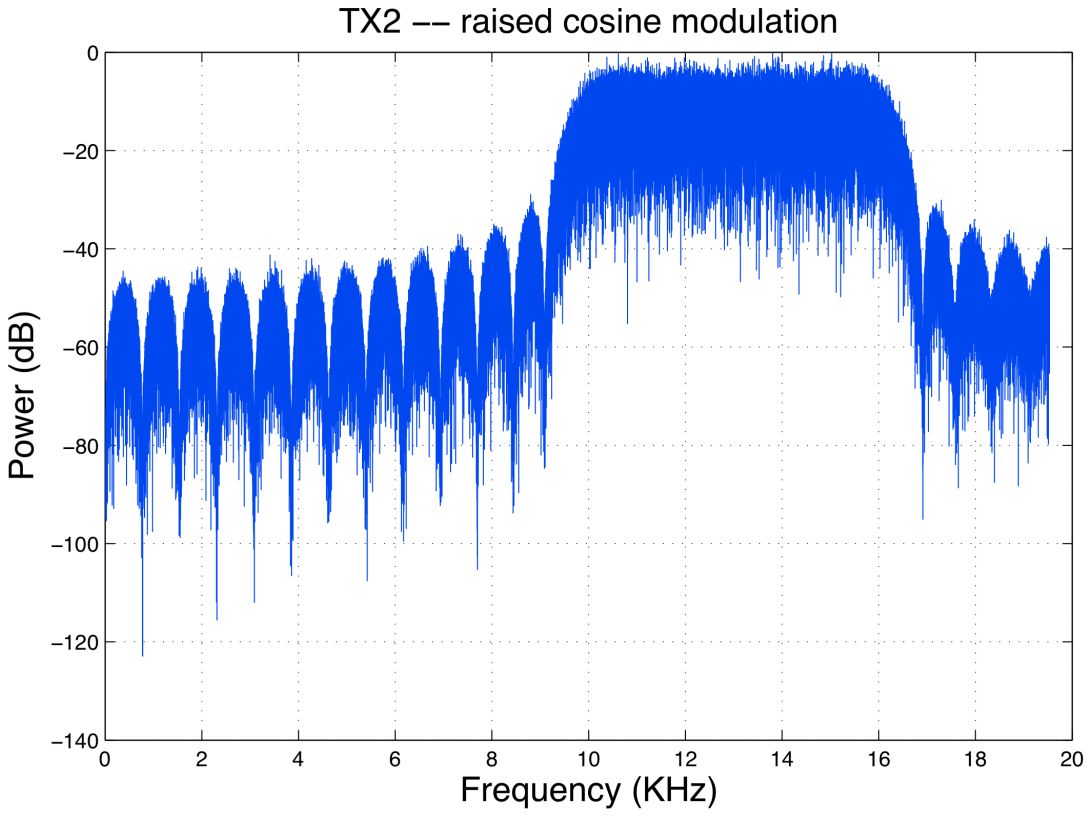

Figure F-1: TX2 – Transmitted Signal Frequency Response: Raised Cosine Modulation

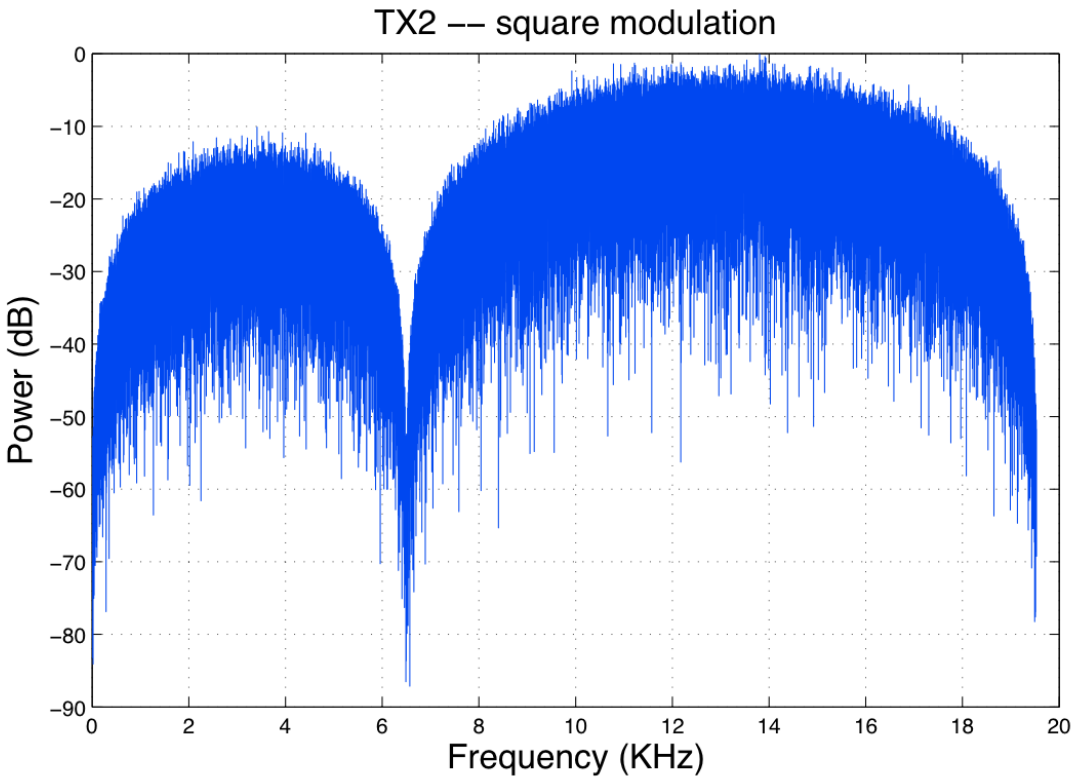

Figure F-2: TX2 – Transmitted Signal Frequency Response: Square Modulation

	Time							
Signaling Rate	NYQ	NYQ	SNQ2	SNQ2	SNQ3	SNQ3	SNQ4	SNQ4
Base Coderate	1/2	9/10	1/2	9/10	1/2	9/10	1/2	9/10
Modulation	square	square	square	square	square	square	square	square
	Time							
Signaling Rate	NYQ	NYQ	SNQ2	SNQ2	SNQ3	SNQ3	SNQ4	SNQ4
Base Coderate	1/2	9/10	1/2	9/10	1/2	9/10	1/2	9/10
Modulation	raised cosine	raised cosine	raised cosine	raised cosine	raised cosine	raised cosine	raised cosine	raised cosine

Table F.2: TX2 signal description

TX1 Useable transmit bandwidth	20kHz $\sim$ 32kHz
Sampling Rate	100,000 samples/second
Signal bandwidth	8.33kHz (12 samples per Nyquist symbol)
Carrier Frequency (f_c)	27kHz
Signal occupied bandwidth	22.8kHz $\sim$ 31.16kHz
HPF	Yes (cutoff frequency at 20kHz)

Table F.3: TX1: Scripps Institute of Oceanography Source Receiver Arrays

TX1W Useable transmit bandwidth	10kHz $\sim$ 32kHz
Sampling Rate	100,000 samples/second
Signal bandwidth	16.67kHz (6 samples per Nyquist symbol)
Carrier Frequency (f_c)	21kHz
Signal occupied bandwidth	12.67kHz $\sim$ 29.33kHz
HPF	No

Table F.4: TX1W: Scripps Institute of Oceanography Source Receiver Arrays

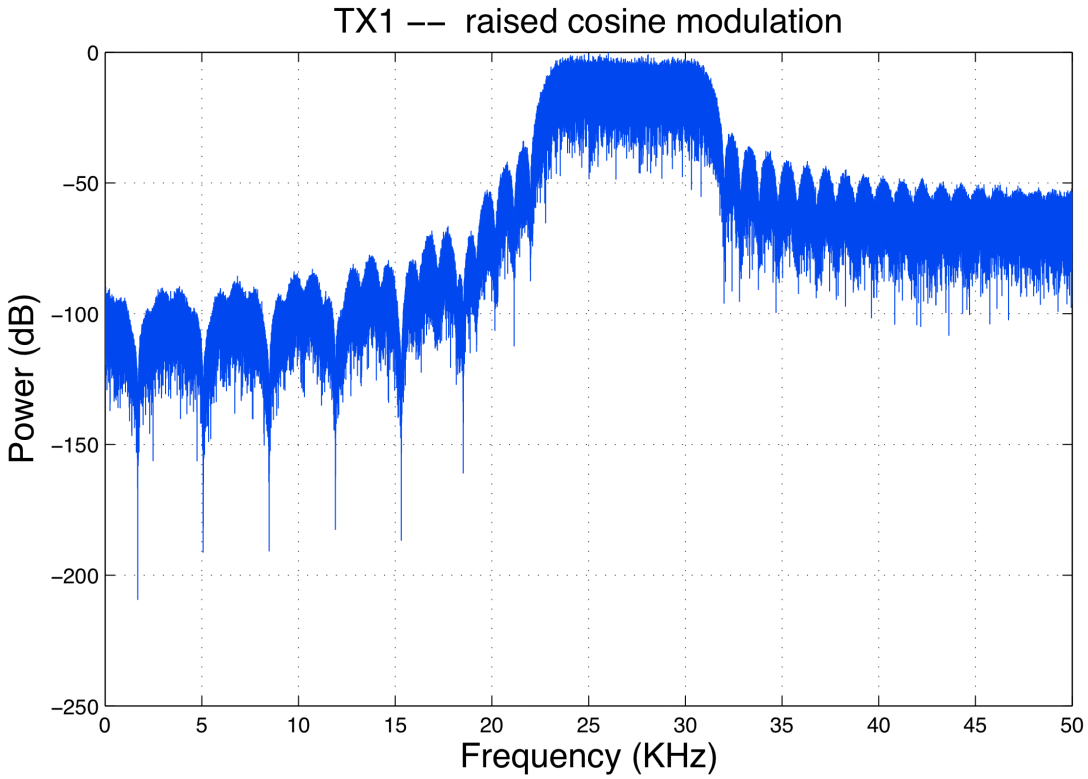

Figure F-3: TX1 – Transmitted Signal Frequency Response: Raised Cosine Modulation

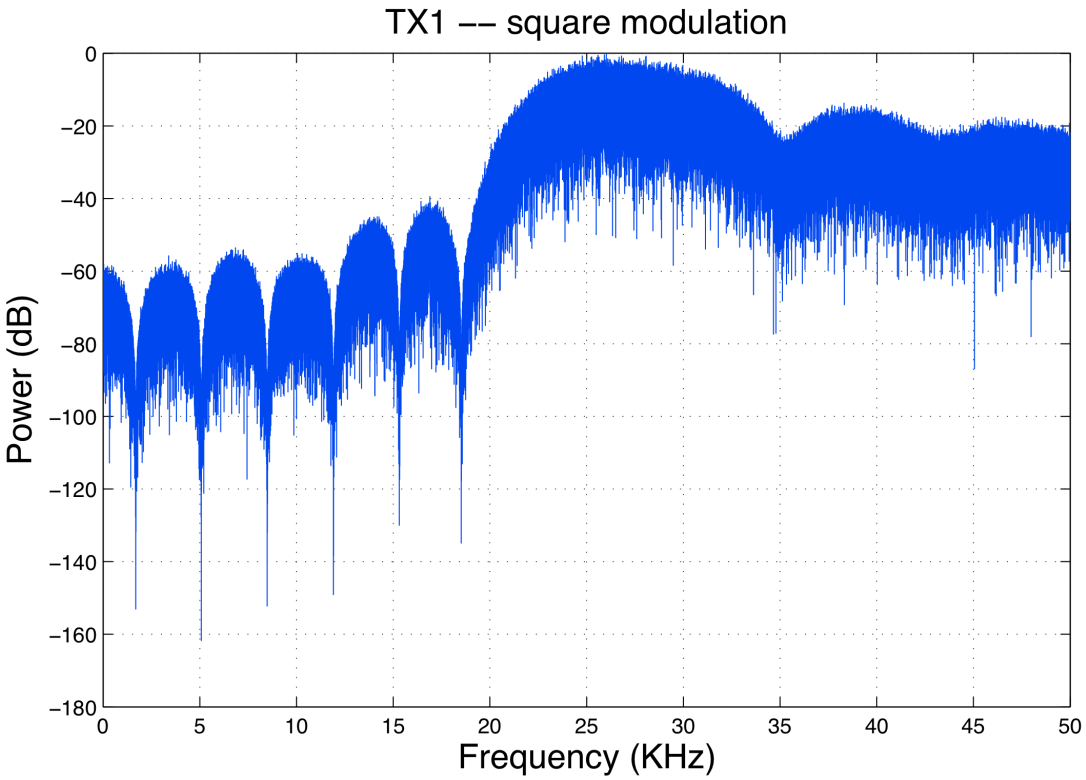

Figure F-4: TX1 – Transmitted Signal Frequency Response: Square Modulation

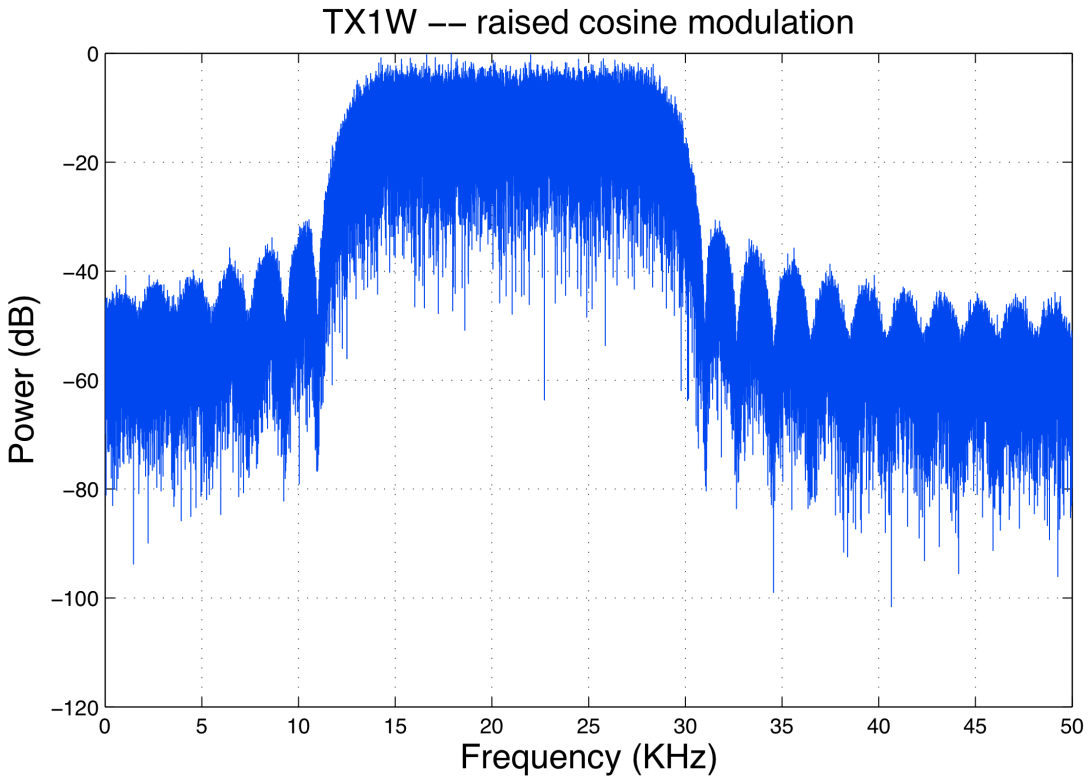

Figure F-5: TX1W – Transmitted Signal Frequency Response: Raised Cosine Modulation

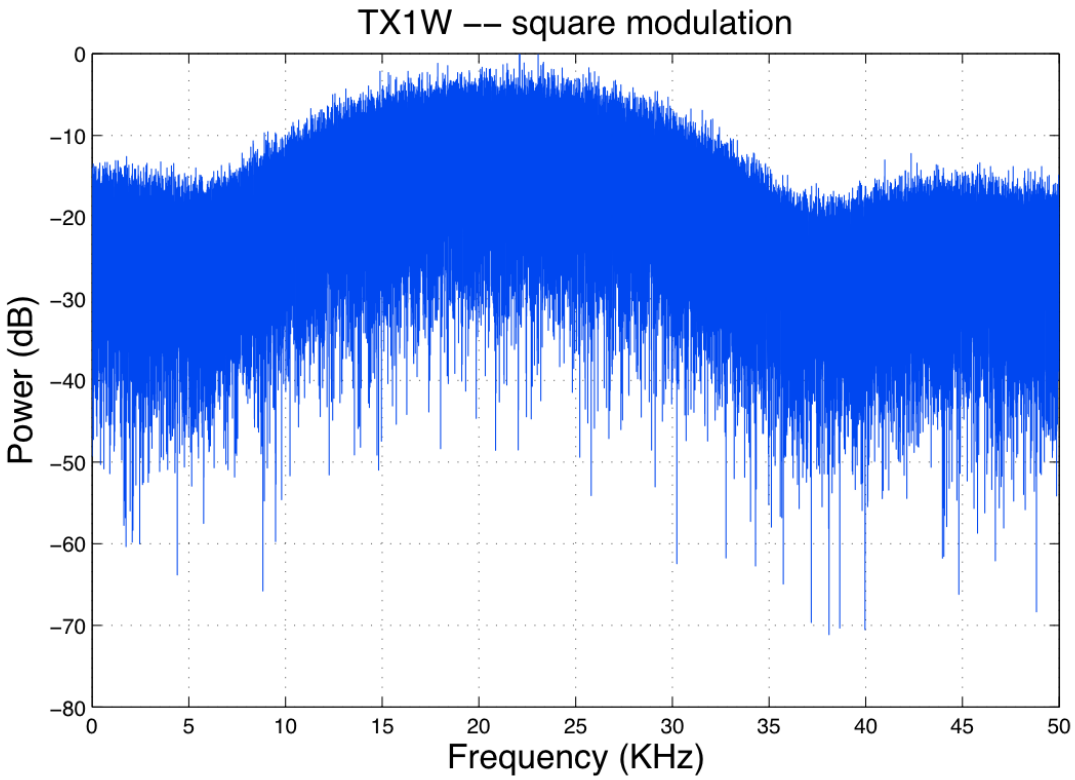

Figure F-6: TX1W – Transmitted Signal Frequency Response: Square Modulation

	Time										
Signaling Rate	NYQ	NYQ	NYQ	SNQ2	SNQ2	SNQ3	SNQ3	SNQ4	SNQ4	SNQ6	SNQ6
Base Coderate	1/2	9/10	1/4	1/2	9/10	1/2	9/10	1/2	9/10	1/2	9/10
Modulation	square	square	square	square	square	square	square	square	square	square	square
	Time										
Signaling Rate	NYQ	NYQ	NYQ	SNQ2	SNQ2	SNQ3	SNQ3	SNQ4	SNQ4	SNQ6	SNQ6
Base Coderate	1/2	9/10	1/4	1/2	9/10	1/2	9/10	1/2	9/10	1/2	9/10
Modulation	raised cosine	raised cosine	raised cosine	raised cosine	raised cosine	raised cosine	raised cosine	raised cosine	raised cosine	raised cosine	raised cosine

Table F.5: TX1 and TX1W signal description[1]

[1]For TX1W, the signal sequence is transmitted twice during a 1-minute transmission

F.2 Detailed Description of Transmitted Signal

Scheme	# of samples	Cumulative # of samples	Scheme	# of samples	Cumulative # of samples	Scheme	#of samples	Cumulative # of samples
Silent bits	20000	20000	**SNQ3 SM (rate 1/2)**	78804	784538	**SNQ2 RC (rate 9/10)**	115248	1663938
Synchronization	528	20528	**SNQ3 SM (rate 9/10)**	78804	863342	**SNQ3 RC (rate 1/2)**	78849	1742787
Zero-Padding	6000	26528	**SNQ4 SM (rate 1/2)**	60605	923947	**SNQ3 RC (rate 9/10)**	78849	1821636
NYQ SM[3] (rate 1/2)	224400	250928	**SNQ4 SM (rate 9/10)**	60605	984552	**SNQ4 RC (rate 1/2)**	60649	1882285
NYQ SM (rate 9/10)	224400	475328	**NYQ RC[4] (rate 1/2)**	224445	1208997	**SNQ4 RC (rate 9/10)**	60649	1942934
SNQ2 SM (rate 1/2)	115203	590531	**NYQ RC (rate 9/10)**	224445	1433442	**Silent bits**	400816	2343750
SNQ2 SM (rate 9/10)	115203	705734	**SNQ2 RC (rate 1/2)**	115248	1548690			

Table F.6: TX2 data transmitted over 1 minute period [2]

[2]For each signaling scheme, the transmitted signal is a concatenation of 1000 training symbols, 32400 coded data symbols and 6000 zero samples.
[3]Square Modulation. (SM)
[4]Raised-Cosine Modulation (RC)

Transducer # 5								
Scheme	**# of samples**	**Cumulative # of samples**	**Scheme**	**# of samples**	**Cumulative # of samples**	**Scheme**	**#of samples**	**Cumulative # of samples**
Silent bits	100000	100000	**SNQ3 SM (rate 9/10)**	157634	2235692	**SNQ2 RC (rate 9/10)**	230521	4455621
Synchronization	1082	101082	**SNQ4 SM (rate 1/2)**	121235	2356927	**SNQ3 RC (rate 1/2)**	157723	4613344
Zero-Padding	12000	113082	**SNQ4 SM (rate 9/10)**	121235	2478162	**SNQ3 RC (rate 9/10)**	157723	4771067
NYQ SM (rate 1/2)	448826	561908	**SNQ6 SM (rate 1/2)**	84836	2562998	**SNQ4 RC (rate 1/2)**	121324	4892391
NYQ SM (rate 9/10)	448826	1010734	**SNQ6 SM (rate 9/10)**	84836	2647834	**SNQ4 RC (rate 9/10)**	121324	5013715
NYQ SM (rate 1/4)	448826	1459560	**NYQ RC (rate 1/2)**	448915	3096749	**SNQ6 RC (rate 1/2)**	84925	5098640
SNQ2 SM (rate 1/2)	230432	1689992	**NYQ RC (rate 9/10)**	448915	3545664	**SNQ6 RC (rate 9/10)**	84925	5183565
SNQ2 SM (rate 9/10)	230432	1920424	**NYQ RC (rate 1/4)**	448915	3994579	**Silent bits**	816435	6000000
SNQ3 SM (rate 1/2)	157634	2078058	**SNQ2 RC (rate 1/2)**	230521	4225100			

Table F.7: TX1 data transmitted over 1 minute period (minute 1 to minute 4) with 1 transducer[5]

[5]For each signaling scheme, the transmitted signal is a concatenation of 1000 training symbols, 32400 coded data symbols and 12000 zero samples.

Transducer # 3 4 5 6								
Scheme	**# of samples**	**Cumulative # of samples**	**Scheme**	**# of samples**	**Cumulative # of samples**	**Scheme**	**#of samples**	**Cumulative # of samples**
Silent bits	100000	100000	**SNQ3 SM (rate 9/10)**	157634	2242184	**SNQ2 RC (rate 9/10)**	230521	4462113
Synchronization	7574	107574	**SNQ4 SM (rate 1/2)**	121235	2363419	**SNQ3 RC (rate 1/2)**	157723	4619836
Zero-Padding	12000	119574	**SNQ4 SM (rate 9/10)**	121235	2484654	**SNQ3 RC (rate 9/10)**	157723	4777559
NYQ SM (rate 1/2)	448826	568400	**SNQ6 SM (rate 1/2)**	84836	2569490	**SNQ4 RC (rate 1/2)**	121324	4898883
NYQ SM (rate 9/10)	448826	1017226	**SNQ6 SM (rate 9/10)**	84836	2654326	**SNQ4 RC (rate 9/10)**	121324	5020207
NYQ SM (rate 1/4)	448826	1466052	**NYQ RC (rate 1/2)**	448915	3103241	**SNQ6 RC (rate 1/2)**	84925	5105132
SNQ2 SM (rate 1/2)	230432	1696484	**NYQ RC (rate 9/10)**	448915	3552156	**SNQ6 RC (rate 9/10)**	84925	5190057
SNQ2 SM (rate 9/10)	230432	1926916	**NYQ RC (rate 1/4)**	448915	4001071	**Silent bits**	809943	6000000
SNQ3 SM (rate 1/2)	157634	2084550	**SNQ2 RC (rate 1/2)**	230521	4231592			

Table F.8: TX1 data transmitted over 1 minute period (minute 5 to minute 8) with 4 transducers [6]

[6]For each signaling scheme, the transmitted signal is a concatenation of 1000 training symbols, 32400 coded data symbols and 12000 zero samples.

	7574 Zero-Padded Synchronization samples			
Transducer 3	1082 Synchronization samples	2164 zero samples	2164 zero samples	2164 zero samples
Transducer 4	2164 zero 2164 zero samples	1082 Synchronization samples	2164 zero samples	2164 zero samples
Transducer 5	2164 zero samples	2164 zero samples	1082 Synchronization samples	2164 zero samples
Transducer 6	2164 zero samples	2164 zero samples	2164 zero samples	1082 Synchronization samples

Table F.9: The synchronization bits for transducer 3, 4, 5, 6

Transducer # 3 4 5 6								
Scheme	**# of samples**	**Cumulative # of samples**	**Scheme**	**# of samples**	**Cumulative # of samples**	**Scheme**	**#of sam-ples**	**Cumulative # of samples**
Silent bits	100000	100000	**SNQ3 SM (rate 9/10)**	157634	2250840	**SNQ2 RC (rate 9/10)**	230521	4470769
Synchronization**	16230	116230	**SNQ4 SM (rate 1/2)**	121235	2372075	**SNQ3 RC (rate 1/2)**	157723	4628492
Zero-Padding	12000	128230	**SNQ4 SM (rate 9/10)**	121235	2493310	**SNQ3 RC (rate 9/10)**	157723	4786215
NYQ SM (rate 1/2)	448826	577056	**SNQ6 SM (rate 1/2)**	84836	2578146	**SNQ4 RC (rate 1/2)**	121324	4907539
NYQ SM (rate 9/10)	448826	1025882	**SNQ6 SM (rate 9/10)**	84836	2662982	**SNQ4 RC (rate 9/10)**	121324	5028863
NYQ SM (rate 1/4)	448826	1474708	**NYQ RC (rate 1/2)**	448915	3111897	**SNQ6 RC (rate 1/2)**	84925	5113788
SNQ2 SM (rate 1/2)	230432	1705140	**NYQ RC (rate 9/10)**	448915	3560812	**SNQ6 RC (rate 9/10)**	84925	5198713
SNQ2 SM (rate 9/10)	230432	1935572	**NYQ RC (rate 1/4)**	448915	4009727	**Silent bits**	801287	6000000
SNQ3 SM (rate 1/2)	157634	2093206	**SNQ2 RC (rate 1/2)**	230521	4240248			

Table F.10: TX1 data transmitted over 1 minute period (minute 9 to minute 12) with 8 transducers [7]

[7]For each signaling scheme, the transmitted signal is a concatenation of 1000 training symbols, 32400 coded data symbols and 12000 zero samples.

	16230 Zero-Padded Synchronization samples							
Transducer 1	1082 Synchro-nization samples	2164 zero samples	2164 zero samples	2164 zero samples	2164 zero samples	2164 zero samples	2164 zero samples	2164 zero samples
Transducer 2	2164 zero samples	1082 Synchro-nization samples	2164 zero samples	2164 zero samples	2164 zero samples	2164 zero samples	2164 zero samples	2164 zero samples
Transducer 3	2164 zero samples	2164 zero samples	1082 Synchro-nization samples	2164 zero samples	2164 zero samples	2164 zero samples	2164 zero samples	2164 zero samples
Transducer 4	2164 zero samples	2164 zero samples	2164 zero samples	1082 Synchro-nization samples	2164 zero samples	2164 zero samples	2164 zero samples	2164 zero samples
Transducer 5	2164 zero samples	2164 zero samples	2164 zero samples	2164 zero samples	1082 Synchro-nization samples	2164 zero samples	2164 zero samples	2164 zero samples
Transducer 6	2164 zero samples	2164 zero samples	2164 zero samples	2164 zero samples	2164 zero samples	1082 Synchro-nization samples	2164 zero samples	2164 zero samples
Transducer 7	2164 zero samples	2164 zero samples	2164 zero samples	2164 zero samples	2164 zero samples	2164 zero samples	1082 Synchro-nization samples	2164 zero samples
Transducer 8	2164 zero samples	2164 zero samples	2164 zero samples	2164 zero samples	2164 zero samples	2164 zero samples	2164 zero samples	1082 Synchro-nization samples

Table F.11: The synchronization bits for transducer 1, 2, 3, 4, 5, 6, 7, 8

Transducer # 5								
Scheme	**# of samples**	**Cumulative # of samples**	**Scheme**	**# of samples**	**Cumulative # of samples**	**Scheme**	**#of samples**	**Cumulative # of samples**
Silent bits	50000	50000	**SNQ3 SM (rate 9/10)**	83604	1156142	**SNQ2 RC (rate 9/10)**	120048	2309193
Synchronization	528	50528	**SNQ4 SM (rate 1/2)**	65405	1221547	**SNQ3 RC (rate 1/2)**	83649	2392842
Zero-Padding	10800	61328	**SNQ4 SM (rate 9/10)**	65405	1286952	**SNQ3 RC (rate 9/10)**	83649	2476491
NYQ SM (rate 1/2)	229200	290528	**SNQ6 SM (rate 1/2)**	47205	1334157	**SNQ4 RC (rate 1/2)**	65449	2541940
NYQ SM (rate 9/10)	229200	519728	**SNQ6 SM (rate 9/10)**	47205	1381362	**SNQ4 RC (rate 9/10)**	65449	2607389
NYQ SM (rate 1/4)	229200	748928	**NYQ RC (rate 1/2)**	229245	1610607	**SNQ6 RC (rate 1/2)**	47250	2654639
SNQ2 SM (rate 1/2)	120003	868931	**NYQ RC (rate 9/10)**	229245	1839852	**SNQ6 RC (rate 9/10)**	47250	2701889
SNQ2 SM (rate 9/10)	120003	988934	**NYQ RC (rate 1/4)**	229245	2069097	**Repeat Signal Transmission**	2640561	5342450
SNQ3 SM (rate 1/2)	83604	1072538	**SNQ2 RC (rate 1/2)**	120048	2189145	**Silent bits**	657550	6000000

Table F.12: TX1W data transmitted over 1 minute period (minute 1 to minute 4) with 1 transducer[8]

[8]For each signaling scheme, the transmitted signal is a concatenation of 1000 training symbols, 32400 coded data symbols and 9000 zero samples.

Transducer # 3 4 5 6								
Scheme	**# of samples**	**Cumulative # of samples**	**Scheme**	**# of samples**	**Cumulative # of samples**	**Scheme**	**#of samples**	**Cumulative # of samples**
Silent bits	50000	50000	**SNQ3 SM (rate 9/10)**	83604	1159310	**SNQ2 RC (rate 9/10)**	120048	2312361
Synchronization**	3696	53696	**SNQ4 SM (rate 1/2)**	65405	1224715	**SNQ3 RC (rate 1/2)**	83649	2396010
Zero-Padding	10800	64496	**SNQ4 SM (rate 9/10)**	65405	1290120	**SNQ3 RC (rate 9/10)**	83649	2479659
NYQ SM (rate 1/2)	229200	293696	**SNQ6 SM (rate 1/2)**	47205	1337325	**SNQ4 RC (rate 1/2)**	65449	2545108
NYQ SM (rate 9/10)	229200	522896	**SNQ6 SM (rate 9/10)**	47205	1384530	**SNQ4 RC (rate 9/10)**	65449	2610557
NYQ SM (rate 1/4)	229200	752096	**NYQ RC (rate 1/2)**	229245	1613775	**SNQ6 RC (rate 1/2)**	47250	2657807
SNQ2 SM (rate 1/2)	120003	872099	**NYQ RC (rate 9/10)**	229245	1843020	**SNQ6 RC (rate 9/10)**	47250	2705057
SNQ2 SM (rate 9/10)	120003	992102	**NYQ RC (rate 1/4)**	229245	2072265	**Repeat Signal Transmission**	2640561	5345618
SNQ3 SM (rate 1/2)	83604	1075706	**SNQ2 RC (rate 1/2)**	120048	2192313	**Silent bits**	654382	6000000

Table F.13: TX1W data transmitted over 1 minute period (minute 5 to minute 8) with 4 transducers[9]

[9]For each signaling scheme, the transmitted signal is a concatenation of 1000 training symbols, 32400 coded data symbols and 9000 zero samples.

	3696 Zero-Padded Synchronization samples			
Transducer 3	528 Synchronization samples	1056 zero samples	1056 zero samples	1056 zero samples
Transducer 4	2164 zero 1056 zero samples	528 Synchronization samples	1056 zero samples	1056 zero samples
Transducer 5	1056 zero samples	1056 zero samples	528 Synchronization samples	1056 zero samples
Transducer 6	1056 zero samples	1056 zero samples	1056 zero samples	528 Synchronization samples

Table F.14: The synchronization bits for transducer 3, 4, 5, 6

Transducer # 1 2 3 4 5 6 7 8								
Scheme	**# of samples**	**Cumulative # of samples**	**Scheme**	**# of samples**	**Cumulative # of samples**	**Scheme**	**#of samples**	**Cumulative # of samples**
Silent bits	50000	50000	**SNQ3 SM (rate 9/10)**	83604	1163534	**SNQ2 RC (rate 9/10)**	120048	2316585
Synchronization**	7920	57920	**SNQ4 SM (rate 1/2)**	65405	1228939	**SNQ3 RC (rate 1/2)**	83649	2400234
Zero-Padding	10800	68720	**SNQ4 SM (rate 9/10)**	65405	1294344	**SNQ3 RC (rate 9/10)**	83649	2483883
NYQ SM (rate 1/2)	229200	297920	**SNQ6 SM (rate 1/2)**	47205	1341549	**SNQ4 RC (rate 1/2)**	65449	2549332
NYQ SM (rate 9/10)	229200	527120	**SNQ6 SM (rate 9/10)**	47205	1388754	**SNQ4 RC (rate 9/10)**	65449	2614781
NYQ SM (rate 1/4)	229200	756320	**NYQ RC (rate 1/2)**	229245	1617999	**SNQ6 RC (rate 1/2)**	47250	2662031
SNQ2 SM (rate 1/2)	120003	876323	**NYQ RC (rate 9/10)**	229245	1847244	**SNQ6 RC (rate 9/10)**	47250	2709281
SNQ2 SM (rate 9/10)	120003	996326	**NYQ RC (rate 1/4)**	229245	2076489	**Repeat Signal Transmission**	2640561	5349842
SNQ3 SM (rate 1/2)	83604	1079930	**SNQ2 RC (rate 1/2)**	120048	2196537	**Silent bits**	650158	6000000

Table F.15: TX1W data transmitted over 1 minute period (minute 9 to minute 12) with 8 transducers[10]

[10]For each signal transmission, it a concatenation of 1000 training symbols, 32400 coded data symbols and 9000 zero samples.

	7920 Zero-Padded Synchronization samples							
Transducer 1	528 Synchro-nization samples	1056 zero samples	1056 zero samples	1056 zero samples	1056 zero samples	1056 zero samples	1056 zero samples	1056 zero samples
Transducer 2	1056 zero samples	528 Synchro-nization samples	1056 zero samples	1056 zero samples	1056 zero samples	1056 zero samples	1056 zero samples	1056 zero samples
Transducer 3	1056 zero samples	1056 zero samples	528 Synchro-nization samples	1056 zero samples	1056 zero samples	1056 zero samples	1056 zero samples	1056 zero samples
Transducer 4	1056 zero samples	1056 zero samples	1056 zero samples	528 Synchro-nization samples	1056 zero samples	1056 zero samples	1056 zero samples	1056 zero samples
Transducer 5	1056 zero samples	1056 zero samples	1056 zero samples	1056 zero samples	528 Synchro-nization samples	1056 zero samples	1056 zero samples	1056 zero samples
Transducer 6	1056 zero samples	1056 zero samples	1056 zero samples	1056 zero samples	1056 zero samples	528 Synchro-nization samples	1056 zero samples	1056 zero samples
Transducer 7	1056 zero samples	1056 zero samples	1056 zero samples	1056 zero samples	1056 zero samples	1056 zero samples	528 Synchro-nization samples	1056 zero samples
Transducer 8	1056 zero samples	1056 zero samples	1056 zero samples	1056 zero samples	1056 zero samples	1056 zero samples	1056 zero samples	528 Synchro-nization samples

Table F.16: The synchronization bits for transducer 1, 2, 3, 4, 5, 6, 7, 8

Appendix G
SNQ-MIMO Additional Simulation Results

In this chapter, we show our preliminary simulation results for the SNQ-MIMO system and discuss our observations.

G.1 Simulation Setup

Without loss of generality, we consider the SNQ-MIMO4 case (i.e. 4 transducers, 4 receivers with SNQ4 signaling). Let i and j denote the transducer number and the receiver number respectively such that $i, j \in \{1, 2, 3, 4\}$. For each path before transducer i to receiver j, there is a corresponding channel impulse response $\mathbf{h}_{ij}$ whose length is l_h. We assume that the length of all channels are equal. In this simulation, entries of each $\mathbf{h}_{i,j}$ are samples from a standard complex Gaussian random variable (i.e. if $\mathbf{X} \sim \mathbb{C}\mathcal{N}(0, 1)$ means $\mathbf{X} = \mathbf{Y} + j\mathbf{Z}$, where $\mathbf{Y}, \mathbf{Z} \sim \mathcal{N}(0, \frac{1}{2})$ and independent). In addition, we define the channel correlation matrix for the MIMO4 channel as follows,

$$\Delta \triangleq \begin{bmatrix} 1 & \delta & \delta & \delta \\ \delta & 1 & \delta & \delta \\ \delta & \delta & 1 & \delta \\ \delta & \delta & \delta & 1 \end{bmatrix}. \tag{G.1}$$

Hence, the overall impulse response can be represented by a three dimensional matrix $\mathbf{H}$, where the first dimension corresponds to transducer number; the second dimension corresponds to receiver number and the third dimension corresponds to time index. Therefore, $\mathbf{H}$ is a matrix of size

$4 \times 4 \times l$ and it is given by,

$$\mathbf{H} \triangleq \eta \begin{bmatrix} \mathbf{h}_{11} & \delta\mathbf{h}_{12} & \delta\mathbf{h}_{13} & \delta\mathbf{h}_{14} \\ \delta\mathbf{h}_{21} & \mathbf{h}_{22} & \delta\mathbf{h}_{23} & \delta\mathbf{h}_{24} \\ \delta\mathbf{h}_{31} & \delta\mathbf{h}_{32} & \mathbf{h}_{33} & \delta\mathbf{h}_{34} \\ \delta\mathbf{h}_{41} & \delta\mathbf{h}_{42} & \delta\mathbf{h}_{43} & \mathbf{h}_{44} \end{bmatrix} \tag{G.2}$$

$$\triangleq \begin{bmatrix} \tilde{\mathbf{h}}_{11} & \tilde{\mathbf{h}}_{12} & \tilde{\mathbf{h}}_{13} & \tilde{\mathbf{h}}_{14} \\ \tilde{\mathbf{h}}_{21} & \tilde{\mathbf{h}}_{22} & \tilde{\mathbf{h}}_{23} & \tilde{\mathbf{h}}_{24} \\ \tilde{\mathbf{h}}_{31} & \tilde{\mathbf{h}}_{32} & \tilde{\mathbf{h}}_{33} & \tilde{\mathbf{h}}_{34} \\ \tilde{\mathbf{h}}_{41} & \tilde{\mathbf{h}}_{42} & \tilde{\mathbf{h}}_{43} & \tilde{\mathbf{h}}_{44} \end{bmatrix} \tag{G.3}$$

where $\eta \triangleq \sqrt{\frac{E}{4\times(1+\delta^2+\delta^2+\delta^2)}}$ is the normalization factor that makes sure the total transmission power from all four transmitters sum up to E. Therefore, the received signal at receiver j is given by,

$$\mathbf{y}_j = \sum_{i=1}^{4} \tilde{\mathbf{x}}_\mathbf{i} \otimes \tilde{\mathbf{h}}_{ij} + \mathbf{n}_{ij}$$

where $\tilde{\mathbf{x}}_\mathbf{i}$ denotes the transmitted signal from transmitter i and $\mathbf{n}ij$ represents the AWGN with power N. Hence, the channel SNR is given by E/N.

G.2 MIMO Simulation Plots

In this section, we show the simulation plots. The following three plots correspond to the cases that $\delta = 0$, $\delta = 0.4$ and $\delta = 0.8$, respectively. As δ increases, the interference among the channels also increases. In each figure, there are four plots that each corresponds to a different channel length l. As l increases, the ISI in each channel increases. For each setup, the simulation is conducted under four SNQ settings: 0dB, 10 dB, 20dB and 30dB. In addition, for each SNR, we run the simulation for ten different randomly generated channels and each point on the plot corresponds to a different channel.

Figure G-1 corresponds to the case that $\delta = 0$. In this case, we have four independent channels. Since the SNQ-SISO structure is shown to be capacity-achieving, we would expect the SNQ-MIMO

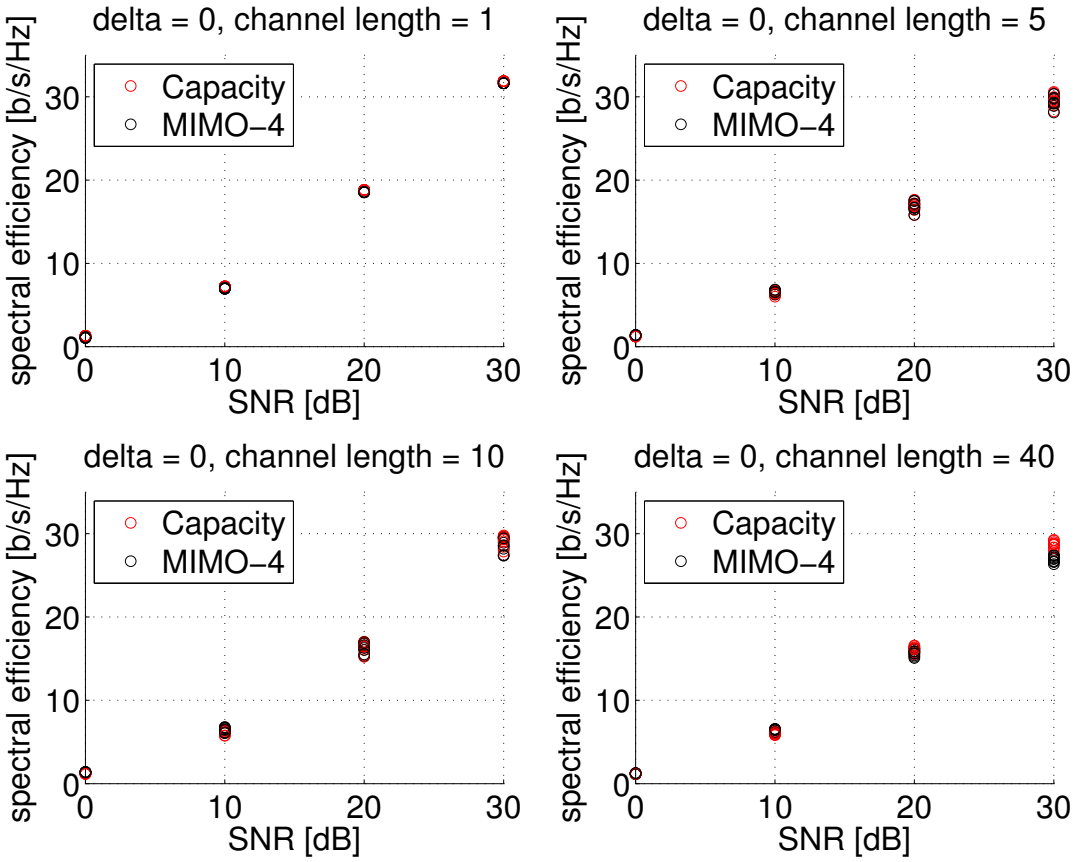

Figure G-1: MIMO Simulation with $\delta = 0$

structure also be capacity-achieving for the $\delta = 0$ case, which is verified by Figure G-1.

Figure G-2 corresponds to the case the there is some interference across the channels. With channel length equal to 1 (first plot in the figure), there are cases that the SNQ-MIMO4 performance is below capacity. However, as the channel length increases, the SNR-MIMO4 performance almost always achieves channel capacity. As shown in the second plot, with channel length equal to 5, the SNQ-MIMO4 points (i.e. black circles) almost overlap exactly with the capacity points (i.e. red circles).

Figure G-3 demonstrates the same behavior as the previous plot. However, with a larger δ value, there are more interference among the MIMO channels. As a result, as shown in the first plot (channel length = 1), there is a larger gap between capacity and the SNQ-MIMO scheme. Nev-

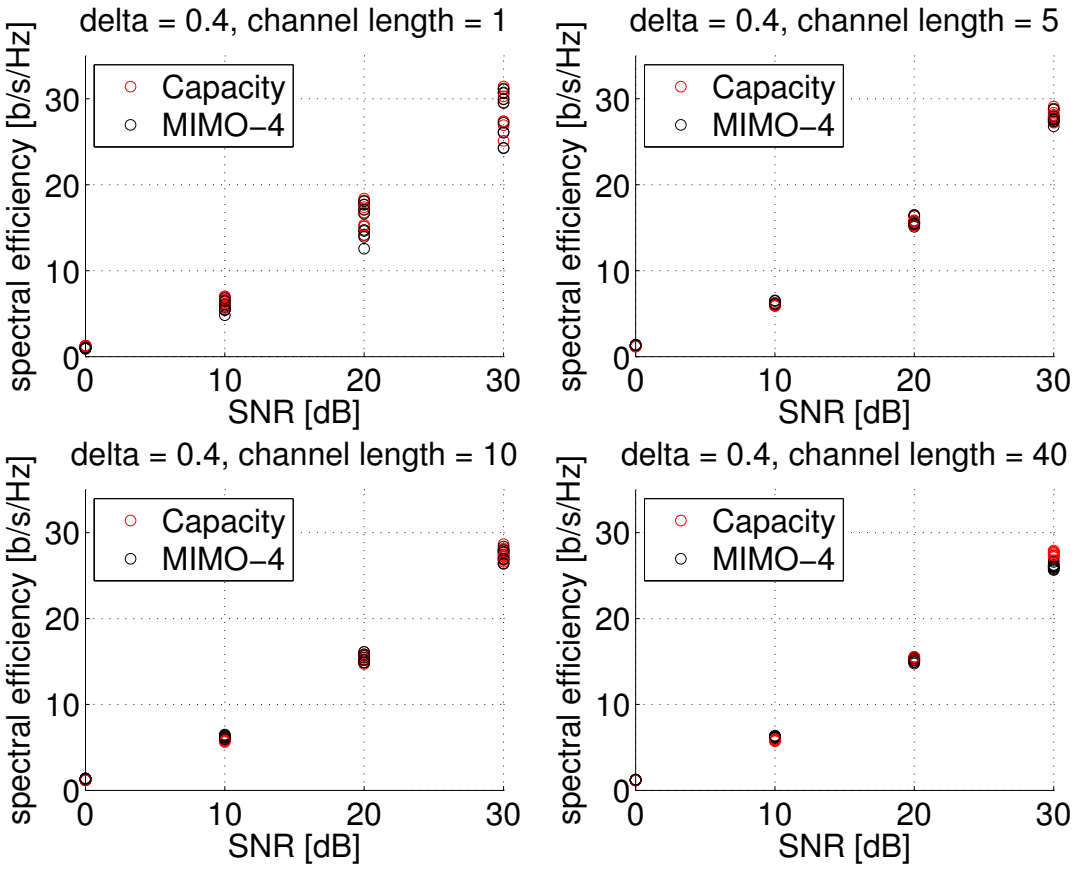

Figure G-2: MIMO Simulation with $\delta = 0.4$

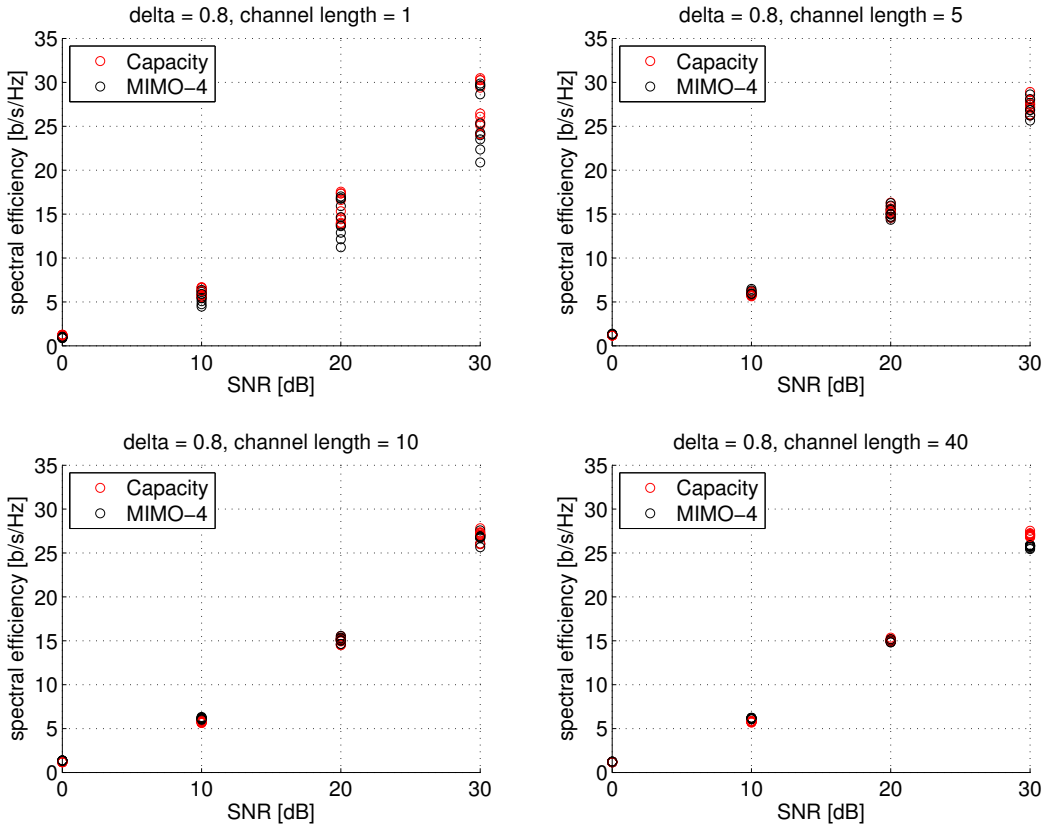

Figure G-3: MIMO Simulation with $\delta = 0.8$

ertheless, the SNQ-MIMO performance points quickly converge to channel capacity as channel length increases. A heuristical explanation for this observation is that, there are specific channels under which the SNQ-MIMO scheme is strictly sub-optimal. However, as channel length increases, the SNQ-MIMO performance is an averaged value over many different channels, which converges quickly to a value that is close to channel capacity.

Bibliography

[1] M. Stojanovic, "Recent advances in high-speed underwater acoustic communications," *Oceanic Engineering, IEEE Journal of*, vol. 21, no. 2, pp. 125–136, 1996.

[2] D.B. Kilfoyle and A.B. Baggeroer, "The state of the art in underwater acoustic telemetry," *Oceanic Engineering, IEEE Journal of*, vol. 25, no. 1, pp. 4–27, 2000.

[3] A.C. Singer, J.K. Nelson, and S.S. Kozat, "Signal processing for underwater acoustic communications," *Communications Magazine, IEEE*, vol. 47, no. 1, pp. 90–96, 2009.

[4] R. Palanki and J. S. Yedidia, "Rateless codes on noisy channels," http://www.merl.com/papers/TR2003-124/, 2004.

[5] U. Erez, M.D. Trott, and G.W. Wornell, "Rateless coding for gaussian channels," *Information Theory, IEEE Transactions on*, vol. 58, no. 2, pp. 530–547, 2012.

[6] U. Erez, G.W. Wornell, and M.D. Trott, "Faster-than-Nyquist coding: The merits of a regime change," *Allerton Conf. Communication, Control and Computing*, , no. Proc. 42nd, pp. 933–942, Sept. 2004.

[7] U. Erez and G. Wornell, "A super-nyquist architecture for reliable underwater acoustic communication," in *Communication, Control, and Computing (Allerton), 2011 49th Annual Allerton Conference on*. IEEE, 2011, pp. 469–476.

[8] T. Guess and M.K. Varanasi, "An information-theoretic derivation of the mmse decision-feedback equalizer," in *Proceedings of the Annual Allerton Conference on Communication Control and Computing*. UNIVERSITY OF ILLINOIS, 1998, vol. 36, pp. 318–327.

[9] J. Preisig, "Acoustic propagation considerations for underwater acoustic communications network development," *ACM SIGMOBILE Mobile Computing and Communications Review*, vol. 11, no. 4, pp. 2–10, 2007.

[10] J.M. Cioffi, G.P. Dudevoir, M. Vedat Eyuboglu, and G.D. Forney Jr, "Mmse decision-feedback equalizers and coding. i. equalization results," *Communications, IEEE Transactions on*, vol. 43, no. 10, pp. 2582–2594, 1995.

[11] Simon Haykin, *Adaptive Filter Theory*, Prentice Hall, 4 edition, Sept. 2001.

[12] M. Stojanovic, J. Catipovic, and J.G. Proakis, "Adaptive multichannel combining and equalization for underwater acoustic communications," *The Journal of the Acoustical Society of America*, vol. 94, pp. 1621, 1993.

[13] J.C. Preisig, A.C. Singer, and G.W. Wornell, "Reduced bandwidth frequency domain equalization for underwater acoustic communications," in *Sensor Array and Multichannel Signal Processing Workshop (SAM), 2010 IEEE*. IEEE, 2010, pp. 93–96.

[14] A. Duel-Hallen and C. Heegard, "Delayed decision-feedback sequence estimation," *Communications, IEEE Transactions on*, vol. 37, no. 5, pp. 428–436, 1989.

[15] David Tse and Pramod Viswanath, *Fundamentals of Wireless Communication*, Prentice Hall, 1 edition, Sept. 2005.

[16] U. Erez and G.W. Wornell, "Super-nyquist rateless coding for intersymbol interference channels," in *International Zurich Seminar on Communications*, 2012, p. 99.

[17] W. Hodgkiss and J. Preisig, "Kauai acomms muri (kam11) experiment," in *Proceedings of the European Conference on Underwater Acoustics*, 2012 (to appear).

[18] Tandberg Television, "A companion guide to dvb-s2," http://www.arctekhd.com/news/stories/DVBS-2guide.pdf, 2004.